ADJOINT BASED AERODYNAMIC SHAPE OPTIMIZATION OF SUBSONIC SUBMERGED INTAKE

A THESIS SUBMITTED TO
THE GRADUATE SCHOOL OF NATURAL AND APPLIED SCIENCES
OF
MIDDLE EAST TECHNICAL UNIVERSITY

BY

ALI AHMED

IN PARTIAL FULFILLMENT OF THE REQUIREMENTS
FOR
THE DEGREE OF DOCTOR OF PHILOSOPHY
IN
AEROSPACE ENGINEERING

MAY 2021

Approval of the thesis:

ADJOINT BASED AERODYNAMIC SHAPE OPTIMIZATION OF SUBSONIC SUBMERGED INTAKE

submitted by **ALI AHMED** in partial fulfillment of the requirements for the degree of **Doctor of Philosophy in Aerospace Engineering Department, Middle East Technical University** by,

Prof. Dr. Halil Kalıpçılar
Dean, Graduate School of **Natural and Applied Sciences** _____

Prof. Dr. İsmail H. Tuncer
Head of Department, **Aerospace Engineering** _____

Prof. Dr. İsmail H. Tuncer
Supervisor, **Aerospace Engineering, METU** _____

Examining Committee Members:

Prof. Dr. Yusuf Özyörük
Aerospace Engineering, METU _____

Prof. Dr. İsmail H. Tuncer
Aerospace Engineering, METU _____

Assoc. Prof. Dr. Harika S. Kahveci
Aerospace Engineering, METU _____

Prof. Dr. Hasan U. Akay
Mechanical Engineering, Atılım University _____

Assist. Prof. Dr. Sıtkı Uslu
Mechanical Engineering, TOBB ETU _____

Date: 04.05.2021

I hereby declare that all information in this document has been obtained and presented in accordance with academic rules and ethical conduct. I also declare that, as required by these rules and conduct, I have fully cited and referenced all material and results that are not original to this work.

Name, Surname: ALI AHMED

Signature :

ABSTRACT

ADJOINT BASED AERODYNAMIC SHAPE OPTIMIZATION OF SUBSONIC SUBMERGED INTAKE

AHMED, ALI
Ph.D., Department of Aerospace Engineering
Supervisor: Prof. Dr. İsmail H. Tuncer

May 2021, 123 pages

In this study the aerodynamic shape optimization of subsonic submerged intake is performed. The total pressure at the aerodynamic interface plane and lift are employed as objective functions. Drag is constrained and employed as penalty objective. Open-ware platforms are used including SALOME for solid modeling, GMSH for the hybrid mesh generation and SU2 for flow solutions and adjoint based shape optimization. Free form deformation box is employed for shape parameterization and surface deformation. Initially NACA intake placed on a flat plate is solved and result is compared with reference study at subsonic flow conditions. Thereafter single objective shape optimization is employed which enhances the C_L/C_D from 0.08 to 0.53 at the end of design cycles. The second case is of trapezoidal-entrance intake placed in slender aerodynamic body. The results are compared with reference study and baseline case for optimization is established. The shape is optimized using multi objective function and for multiple free form deformation boxes. The intake remains flush with the body during the shape deformation process. The intake internal surface is then allowed to deform

along the optimization steps. The pressure recovery increases by 3%. The third case is similar but with circular entrance in slender body. A single free form deformation box encloses the intake region and the deformation is allowed such that optimization creates a semi-submerged shape. The total pressure recovery increases by 2% and C_L/C_D also increases by 10%. In the last case again the trapezoidal entrance intake is employed. The optimization process is similar to the third case. The optimum shape produces a substantial deformation at the intake surface and a semi-submerged intake is finally formed. The total pressure recovery improves by 6% and an additional C_L/C_D ratio of 0.04 is achieved.

Keywords: Flush Intake, Submerged Intake, SU2, Shape Optimization, Adjoint Solver

ÖZ

SESALTI GÖMÜLÜ HAVA ALIKLARI İÇİN ADJOİNT TABANLI AERODİNAMİK ŞEKİL OPTİMİZASYONU

AHMED, ALI
Doktora, Havacılık ve Uzay Mühendisliği Bölümü
Tez Yöneticisi: Prof. Dr. İsmail H. Tuncer

Mayıs 2021 , 123 sayfa

Bu çalışmada, yüzeye gömülü bir ses-altı hava alığının şekil optimizasyonu yapılmıştır. Amaç fonksiyonlar olarak aerodinamik arayüzdeki toplam basınç ve kaldırma kuvveti tanımlanmıştır. Kısıtlayıcı ve ceza fonksiyonu olarak sürüklenme kuvveti belirlenmiştir. Katı modelleme için SALOME, çözüm ağı GMSH, akış çözümü ve adjoint optimizasyon için ise SU2 açık kaynak kodlar kullanılmıştır. Şekil parametrizasyonu ve yüzey deformasyonları, Serbest Şekil Deformasyon (FFD) kutusu ile yapılmıştır. Önce, düz plaka üzerine yerleştirilmiş NACA alığında ses-altı şartlarda alınan sonuçlar doğrulanmıştır. Ardından, şekil optimizasyonu ile CL/CD oranı 0.08den 0.53e iyileştirilmiştir. İkinci bir çalışma, bir narin gövde içerisine yerleştirilmiş trapezoidal girişli alık ile yapılmıştır. Sonuçlar doğrulanmış ve optimizasyona baz model olarak kullanılmıştır. Şekil, çok-amaçlı bir fonksiyon için ve çoklu FFD kutusu ile optimize edilmiştir. Şekil deformasyonunda alık ve gövde aynı düzlemde tutulmuştur. Daha sonra, alığın iç yüzeyinin deforme olmasına izin verilmiştir. Basınç geri kazanımı $\%3$ artırılmıştır. Üçüncü çalışma, benzer bir narin gövdedeki dairesel bir girişi içermektedir. Burada, alık tek bir FFD

kutusu içine alınmaktadır ve optimizasyonda yarı-gömülü bir şekil oluşacak şekilde deformasyona müsaade edilmiştir. Basınç geri kazanımında $\%2$ artış ve CL/CD oranında $\%10$ iyileşme sağlanmıştır. Son çalışmada ise yine trapezoidal girişli alık ele alınmıştır. Optimizasyon süreci, üçüncü çalışmaya benzer şekilde işletilmiştir. Alık yüzeyinde kayda değer bir deformasyon sonucunda optimum şekil elde edilmiş ve yarı-gömülü bir alık oluşturulmuştur. Basınç geri kazanımında $\%6$ artışın yanı sıra 0.04 CL/CD oranı elde edilmiştir.

Anahtar Kelimeler: Yüzeye Gömülü Alık, SU2, Şekil Optimizisyon, Adjoint

ACKNOWLEDGMENTS

I would like to express my deepest and most sincere gratitude to my thesis supervisor Prof. Dr. İsmail H. Tuncer for his confidence and trust in me which provided me the strength and ability to accomplish my goal. Without his support and guidance it would have been almost impossible to finish this daunting task. I would also like to acknowledge all the members of the examining committee for agreeing to read my thesis and for taking interest in my work.

I am thankful to my parent organization CESAT for supporting my doctoral program. I hope that my research will be beneficial to my organization and my country Pakistan. I am indebted to my friend and colleague Muhammad Omair for his sincere support and goodwill. I am proud and at the same time greatly humbled to be a member of METU which dignifies who I am. My time spent here has given me the opportunity to make great friends and acquaintances. I would like to express my gratitude to my friend Hüseyin Can Önel with whom I discussed and solved many technical problems. I am thankful to my friend Alp Tikenoğulları who helped me understand the different skills useful to manage my tasks. I am grateful to the administrative staff at the Aerospace department METU specially Madam Derya for her help in administrative issues and her kind attitude.

I am very lucky to have the most loving family and I am specially grateful to my beloved wife Sara and our children, Armughan, Aarib and Arfaa who stood by me in the most testing times with patience and empathy. I am truly grateful to Aunt Farhat for her kindness and support for me and my family. I am thankful to my siblings Aysha and Abdullah for all their help, affection and for boosting my spirits. I wish to express my deepest and most humble gratitude to my father whose faith in me and encouragement is the source of my hope and perseverance.

Finally as a tribute to my dear mother, who lost her battle to cancer in 2019, I dedicate my thesis.

TABLE OF CONTENTS

LIST OF TABLES

TABLES

LIST OF FIGURES

FIGURES

LIST OF ABBREVIATIONS

AD	Automatic /Algorithmic Differentiation
AIP	Aerodynamic Interface Plane
BC	Boundary Condition
BL	Boundary Layer
CAD	Computer Aided Design
CFD	Computational Fluid Dynamics
DC	Distortion Coefficient
DES	Detached Eddy Simulation
DOE	Design of Experiment
FFD	Free Form Deformation
GA	Genetic Algorithm
KKT	Karush–Kuhn–Tucker
LES	Large Eddy Simulation
RANS	Reynolds-Averaged Navier-Stokes Model
NACA	National Advisory Committee for Aeronautics
NURBS	Non-Uniform Rational B-spline or NURBS
SQP	Sequential Quadratic Programming
SST	Shear Stress Transport
SU2	Stanford University Unstructured
RCS	Radar Cross Section
UAV	Unmanned Aerial Vehicle
VG	Vortex Generator

LIST OF SYMBOLS

α	Angle of attack or alpha
C_D	3D drag coefficient
C_L	3D lift coefficient
C_p	Pressure coefficient
D	3D drag
ε	Rate of dissipation of turbulent kinetic energy
k	Turbulent kinetic energy
L	3D lift
ρ	Free stream density
σ	Total pressure recovery factor
$\overline{\overline{\sigma}}$	Stress tensor
V_0	Free stream velocity
V_1	Intake entrance velocity
p_0	Free stream static pressure
P_0	Free stream total pressure
p_2	Outlet static pressure/ Static pressure at AIP
P_2	Total Pressure at AIP
$P_{2\theta min}$	Total Pressure at worst sector of AIP
U	Flow variable vector
$Y+$	Non-dimensional distance from the wall to the first mesh node based on local cell fluid velocity
θ	Angle of worst sector subtended at the centre of the AIP

CHAPTER 1

INTRODUCTION

The intake along with the nozzle is one of the two air breathing engine components that directly interface with the air frame. Therefore it becomes the problem of engine to air frame integration to properly design an intake. Air intake are installed in vehicles primarily to feed air to the engine which generate thrust. Secondary usages can be cooling of engine/avionics parts or maintaining cabin pressure. Air intake are employed such as to supply the readily available air from the freestream, in which the vehicle is moving, to the engine. Intuitively this requirement can be fulfilled by a duct which has opening in the ambient flow and physically links freestream to the AIP (aerodynamic interface plane). This need for air is continuous for the duration of flight and must be fulfilled as per engine requirement with minimum losses. Traditionally the intake performance is measured by flow rate, total pressure recovery factor and flow uniformity but as the complexities of aircraft applications increase so does the demand of including other parameters which were disregarded in earlier designs such as stealth capability and lift.

Submerged or flush intake is inherently capable of having low radar cross section RCS by virtue of its shape, and the desire to use it in such applications where stealth capabilities are desirable, is but natural. However flush intake lack other performance parameters such as pressure recovery and flow distortion which aggravate at off-design angles of attitude. Another drawback of a submerged intake is large internal volume requirement due to small ramp angle for optimum performance. The present study suggests that in order to evaluate submerged intake and improve trade studies with other type of intake, the possibility of lift generation must also be accounted for, specially in instances when the submerged intake is top/bottom

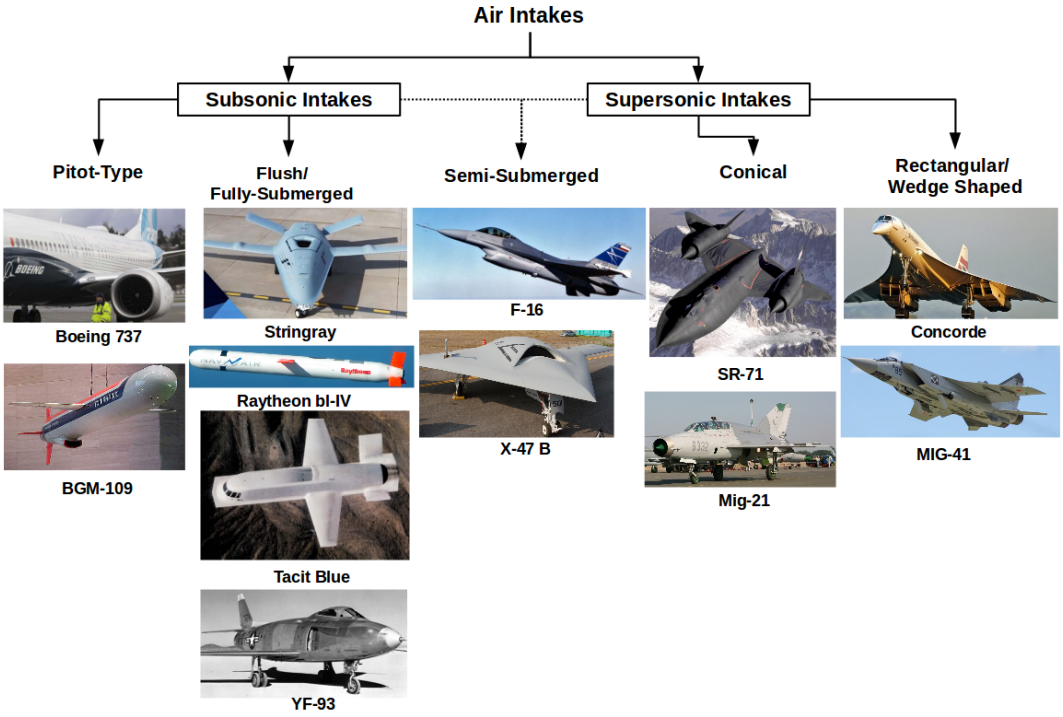

Figure 1.1: *Types of intake in aerospace industry*

mounted on the air frame. Therefore as an additional performance parameter, evaluation of complete vehicle C_L/C_D for a air frame top-mounted with submerged intake is carried in the current study.

1.1 Applications of Flush or Submerged Intake

The type of intake to be installed depends upon the aircraft. The range of applications covers all the aircraft which employ air breathing engines for propulsion. The two major categories are subsonic and supersonic aircraft and hence are their respective intake types. Subsonic aircraft such as commercial jets are mounted with engines below each wing inside a nacelle with a pitot-type capture area. Cruise missiles also employ pitot intake which protrude from the belly as cowl which encloses the s-duct connecting the intake to the engine. In order to improve the stealth capabilities of cruise missiles and UAVs, pitot intake are replaced by submerged/flush intake such as the improved version of BGM-109 now known as Raytheon block-IV which has a NACA intake located at the belly of fuselage. Other aircraft with fully flush intake

are Stringray, TacitBlue UAVs and YF-93 jet.

Submerging the intake also reduces parasite drag hence the pitot type intake in the latest version of the F-16 jet fighter has been replaced by a diverter-less subsonic intake (DSi). However is not a fully submerged intake and it operates in both subsonic and supersonic regimes therefore it is categorized as semi-submerged intake. UAVs such as Dassault Neuron and X-47 both have semi-submerged intake mounted on top for reducing observability and RCS. The design of supersonic intake requires external compression by cone or wedge to reduce pressure recovery losses during compression. The SR-71 Blackbird is mounted with two conical intake on the wings, placed inside nacelles while several fighter jets such as Mig-21 have a nose-cone intake. The Concorde supersonic commercial jet has two pairs of rectangular ramp-shaped intake placed below each wing. Similar design is also utilized in many fighter jets.

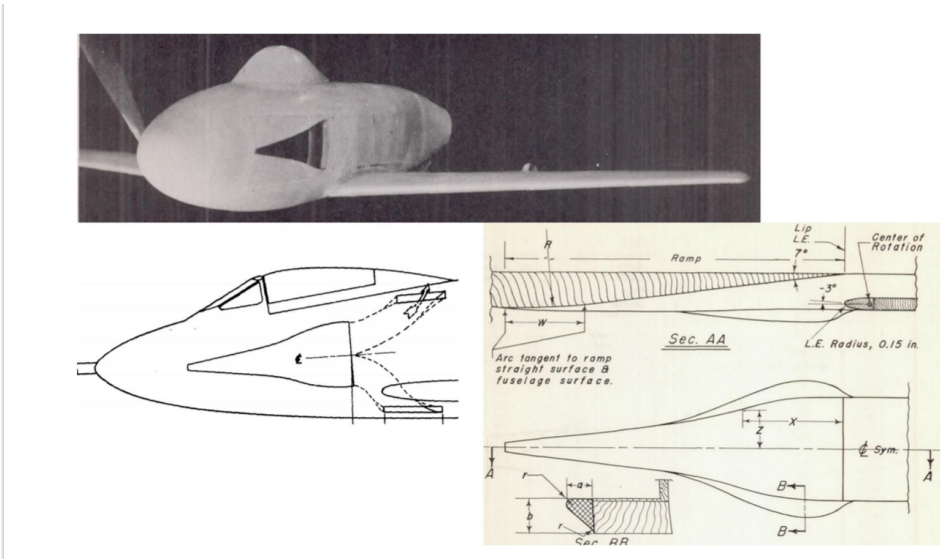

Figure 1.2: *Submerged intake concept by NACA [1]*

1.1.1 NACA Intake

The end of WWII saw the advent of jet fighters and new concepts were realized for improving the performance of such aircraft. One such concept is that of a fully submerged or flush intake mounted on the YF-93 jet fighter, which is developed and implemented at NACA by Randall and Mossman [1] and [3].

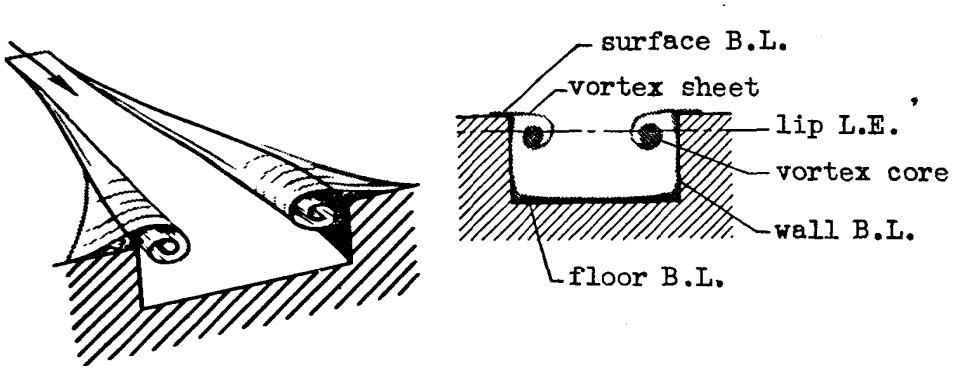

Figure 1.3: *NACA Intake with counter rotating vortex pair [2]*

NACA-type air intake are special type of flush intake with a trapezoidal entrance. The trapezoidal shape gives a smaller shorter leading edge compared to the trailing edge. This serves to deviate the boundary layer away from intake and reduces its effect on the free-stream which is ingested in the engine.
Secondly the side edges of the trapezoidal intake section are kept sharp in order to produce a counter rotating vortex pair which energizes the flow entering the intake and produce inward entrainment allowing more mass flow rate to be ingested from the free-stream, as found in a study done by Sacks and Spreiter [2]. Several configurations were tested by Holzhauser et al. [11] and a high performing shape thereafter named the NACA intake was finalized for flight.

The NACA flush intake was rigorously tested and a comparison study was also done with scoop type intake. Both intake were mounted on an experimental fighter jet and their respective performances were evaluated with respect to pressure recovery, drag and flow rate. NACA intake performed well for Mach numbers from 0.7 to 0.88 as studied by Taylor [12]. However it was observed that the scoop intake outperformed the NACA intake at Mach number 0.9 as studied by Rolls [13]. Thereafter the NACA intake was disregarded for YF-93 and replaced by the scoop intake and the NACA intake was not considered for transonic applications but it continued to be considered for subsonic applications and auxiliary purposes which are discussed in next section. Thus the full potential of the NACA intake was yet to be fully exploited.

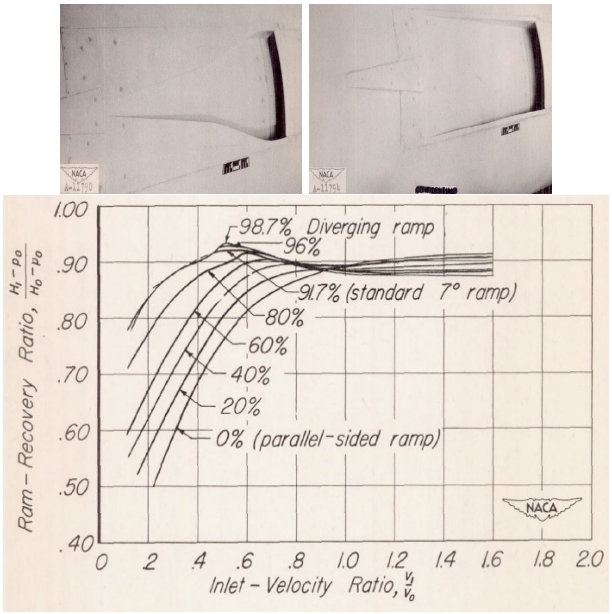

Figure 1.4: *Experimental study to optimize intake shape by Mossman [3]*

1.1.2 Applications of NACA Intake- Auxiliary Air Supply and Racing Cars

The arrival of modern commercial aircraft increased the requirement of air for electronic cooling, cabin or cockpit ventilation and suction slots for boundary-layer control systems which created a demand for auxiliary intake in transonic vehicles as studied by Dennard [14] . The intake thus employed should be able to provide air to the aforementioned auxiliary applications without generating any additional drag of their own. Several intake configurations were tested and NACA intake with a 7° ramp angle delivered desirable performance. The performance evaluation of submerged intake were also conducted in academia and the first study was published by Smith et al. [15] from Cambridge in 1967 on the influence of boundary layers in submerged intake. Later years witnessed a decrease in interest however in 1982, IHS released a document ESDU 86002 [16] for auxiliary units. The document provides standard NACA intake designs and respective performances at various flight conditions. This increased a demand for various commercial jet applications specially for HVAC systems for maintaining cabin pressure and avionics components cooling, as well as racing cars as reported by Roe and Co [17].

1.1.3 Renewed Interest-Stealth Capability of aircraft

There was a renewed interest in the submerged intake for aircraft engines in the late 1970s when large number of fighter jets were hit during the ensuing wars due to being susceptible to radar observance. The susceptibility of an aircraft was considered by Throndson as an important trade-off parameter compared to its performance in the face of survival [18] . This demanded that the engine should be kept out-of-sight at all attitude of the flight and the intake must have a very low radar cross section (RCS) presented by Odendaal and Grygier [19]. The next generation of aircraft such as the F-16 was installed with a semi-submerged Diverterless Subsonic Inlet DSI which is a modification from the previous pitot-intake as given in AGARD report [20]. This greatly reduces the RCS as well as the parasite drag. Other aircraft such as reconnaissance UAVs and cruise missiles also incorporated the submerged intake in later designs for stealth capabilities. The inherent shape of the flush intake gives it low observability which is highly sought after in military applications specially UAVs and cruise missiles which must avoid radar signals while travelling inside enemy domain as studied by da Silveira et al. [21] and Kornev [22]. However the absence of ramming effect of incoming air, the general design of the vehicle does not allow for high speed applications and therefore the range is limited to subsonic Mach number= 0.6-0.8.

1.2 Historical Account of Numerical Studies on Submerged Intake

Interest in submerged intake started with the onset of high thrust jet engines and the need arose to solve the problem of integrating the engine with the aerodynamic vehicle at transonic speeds. NACA intake were fully submerged intake and provided the desired solution but were only used thereafter as auxiliary devices. Renewed interest followed when it was realized that the submerged intake has inherent capability of reducing RCS. This characteristics gives it a major advantage in terms of stealth. With the turn of the 21st century further research followed in numerical based studies and optimization. The general increase in interest in CFD also saw a number of computational studies being conducted on NACA intake as well as other non-generic submerged intake and study by Sun and Rongwei [23] is of particular

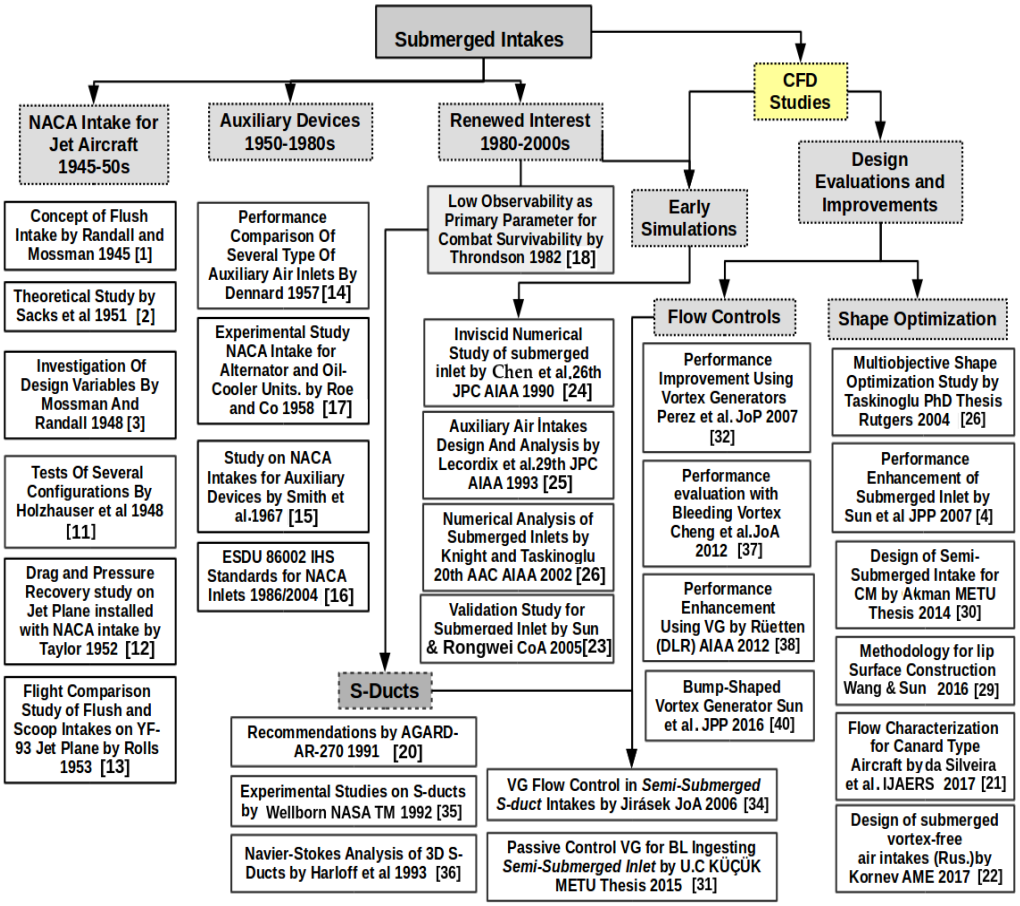

Figure 1.5: *A hierarchical representation of salient studies on submerged intake*

importance . Earlier all of the studies conducted were experiments by NACA on its generic flush intake so most of the initial numerical simulations were basically comparisons with those experimental results. Elementary studies such as Chen et al. [24] and Lecordix [25] were published in early 1990s which comprises of flow simulation results. A collection of various studies on high speed intake with special focus on s-ducts is found in the recommendations by AGARD [20]. Apart from simulations on already tested geometries, CFD based design studies comprised of two main areas: shape optimization of intake and flow control studies. The latter as mainly based on improving the intake performance by introducing different shapes of flow control devices such as vortex generators (VG) or flow bleeding. Some studies were done for shape optimization of VG inside submerged intake. Shape optimization studies on submerged intake using CFD can be traced back to early 21st century when Taskinoglu and Knight [26] published their study in 2002. This later culminated into a full PhD thesis in 2004 based on multi-objective optimization of

a submerged subsonic intake shape [27] in which a fin is placed inside the duct of a submerged intake and by varying the fin angle of attack along axis normal to the core flow it changes direction of swirl of the fin tip vortices which consequently improves the wall pressure distribution and reduce flow distortion coefficient at the AIP. This thesis is frequently cited in later studies since it incorporates multi-objective optimization techniques such as Pareto data sets into numerical studies.

Sun et al. published a comparison study on performance enhancement of a submerged intake [4]. Interestingly the geometry used in study was a non-generic shape and the numerical simulations were run on FLUENT commercial software and results thereof were compared with experimental results conducted in Nanjing University wind tunnel. Different geometric parameters for shape optimization such as ramp angle, side edge angle and lip profile were used as variables to improve total pressure recovery factor and distortion coefficient DC(θ). As an implication, it was realized that shapes other than the NACA intake can be considered for aerospace applications.

This was followed by several numerical and experimental studies on shape optimization and VG based flow control. However the building blocks for submerged intake were yet to be properly defined. Therefore the geometric parameters for the construction of the submerged intake lip were outlined for first time by Wang et al. in 2016 [28]. In this study various parts of the lip which are combined to construct the geometry and defined as per standard theory of differential geometry previously given by Carmo [29]. The u- and v- curves form the two sides of the lip outer most edge and are called the planar curves which are smoothly connected to form a single curve by blending curves at either ends. Similarly the lip inner edge is constructed and then surface of lip is generated by extrusion of outer edge on to inner edge by a third curve named the ridge. The definition of the different geometric parameters is followed by a complex methodology of construction steps. A numerical study is finally described in which the performance of the geometrically specified submerged intake is evaluated. It is worth mentioning at this point that an optimization study on semi submerged intake was done by Akman as fulfillment of MS thesis from METU [30]. The thesis encompasses gradient based optimization for a subsonic-transonic intake with total pressure recovery factor and distortion coefficient as the objective functions and throat area of s-duct as the geometric constraint using a commercial

CFD software. The step-wise optimization method was first validated for total pressure recovery factor as the single objective function in unconstrained fashion then this validated method was applied to generate the optimized intake shape. The improvement achieved for total pressure recovery factor was 6.45 % and DC(60) improved by 45%, as claimed in the thesis. Recently another thesis by Küçük [31] in METU studied the possibility of using passive control in semi-submerged intake. The working principle of flow control using VG as flow control device as studied by Perez et al. [32] is simply to mix the boundary layer with the inviscid freestream which energizes and homogenize the overall flow and improve uniformity and flow quality at the AIP. Vortex generators VG for flow control were first presented by Kaldschmidt [33] in 1973 at NASA. However CFD tools for investigating the effect of VG in a semi-submerged intake was applied for first time by Jirasek [34] in simulations done at the Swedish Defence Research Agency FOI . The study at FOI was a comprehensive examination of the flow inside a s-duct with vortex generators of different configurations and compare CFD and experimental results.

Some other studies such as Wellborn et al. [35] focus on s-duct flows specially on the areas where separation distorts the flow downstream at the AIP. VG are also experimented by Harloff et al. [36] with s-duct to mix the boundary layer and delay or subside separation at second bend. By applying such techniques, improved results in the form of total pressure recovery factor and lower DC were obtained. Cheng and Sun et al. [37] claimed in their CFD study about the improvement of flow quality at the AIP by introducing bleeding vortex as flow control device placed at different locations surrounding the submerged intake. The study was carried out on FLUENT commercial software using RANS method with a step wise grid independence study. The results obtained from the CFD study were claimed to be in agreement with experimental results from Sun et al. [4]. This study concludes that bleeding vortex has the advantage of reduced drag due to absence of any solid VG placed in the free stream.

Study on comparison of different types of VG pairs was done at DLR by Rutten et al. [38]. The VG pair were not placed inside the duct as in earlier studies but on the fuselage upstream of the intake and interestingly results showed improvement in total pressure recovery factor. Earlier Ruetten in another study discussed performance

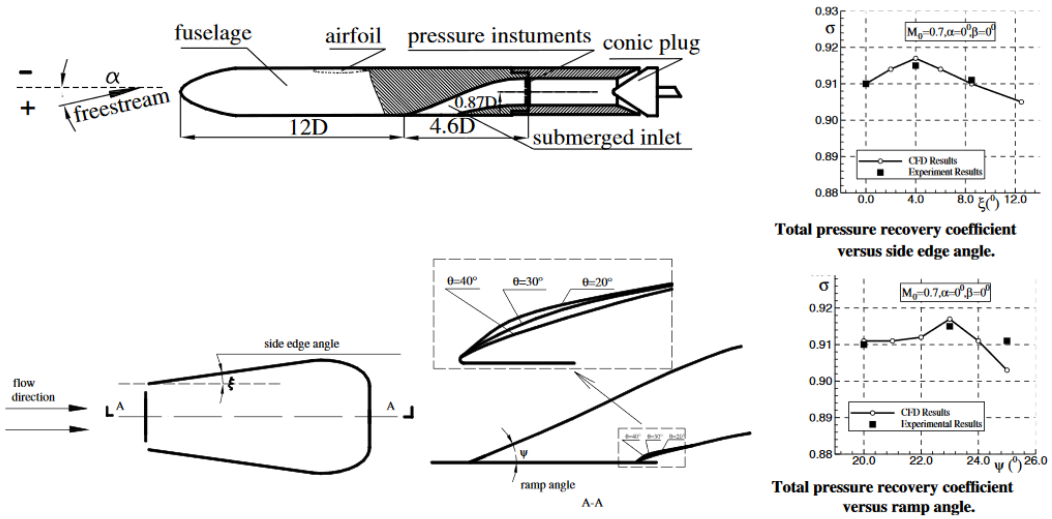

Figure 1.6: *Intake characterized for AIP pressure vs. side edge angle and ramp angle [4]*

of scoop and NACA type intake for DLR F12 aircraft (similar in shape and size to A340) in a bleedless configuration [39]. Although the studies done at DLR were performed for auxiliary intake, application of VG pairs for intake of propulsion systems can be further explored. In an experimental study corroborated with CFD by Sun et al. [40], a unique bump-shaped VG, also placed upstream in similar fashion to DLR, was optimized for improving flush intake performance. The Nanjing University wind tunnel was used as the experimental facility and CFD software FLUENT was used in to estimate the drag. The flight conditions were varied for different free stream Mach and angles of attitude. The findings claimed that the placement of the bump VG upstream of the submerged intake will mitigate the effect of boundary layer carried over along the fuselage and from entering the intake. Thus despite the 0.76% drag penalty, it was claimed that the total total pressure recovery factor increased by as much as 3.7 to 5% for free stream Mach number ranging from 0.73 to 0.9 for a intake with bump VG compared to that of a clean configuration. Aero-acoustic effects of submerged intake were investigated in parallel to flow simulations using detached eddy simulation method by Pignier et al. at KTH in 2016 [5]. DES solves RANS for attached boundary layer and LES for the region of separation and secondary flow. Hence it improves the quality of the CFD results without significantly increasing computational load. Mesh independence study was done upto 47.8 million cells. Results were also calculated for Cp distribution and compared with DES and experimental results from previous studies on NACA.

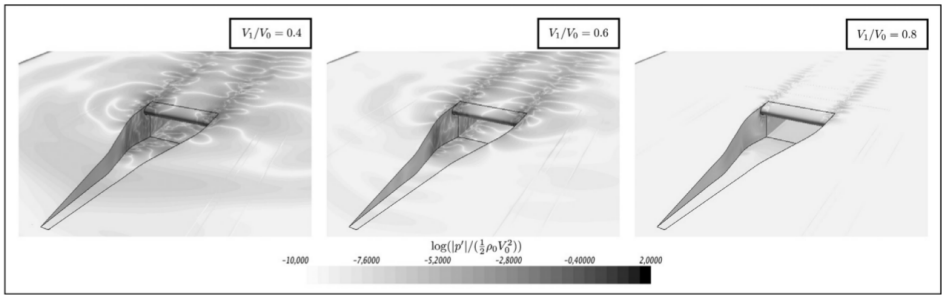

Figure 1.7: *Acoustic predictions for NACA intake by Pignier [5]*

The primary variable was the velocity ratio V_1/V_0 where V_1 is the velocity of air entering the intake at ramp section and V_0 is the free stream velocity. The maximum acoustic effects were generated at lower velocity ratios and diminished as the velocity ratio approached unity.

1.3 Aerodynamic Shape Optimization Studies

Aerodynamic shape optimization is a branch of a broader field of the continually expanding field of aerodynamics which also includes experimental and analytical tools. Numerical optimization is based on CFD and is now considered in mainstream aerospace applications. Several studies have shown great success in this new field and this study is a part of the on-going advancements. CFD has the advantage of generating complete field of flow parameters and therefore makes it feasible for optimization. The underlying principles and the equations involved are explained in details in many references specially by Janiga [41] who compiled the basic theory of CFD and optimization and explained the manner in which the two branches are combined to give the powerful tool called CFD-O. To further develop interest in the topic , an early survey of different shape optimization was done by Jamshid and Samareh [42] in order to select the most suitable mathematical formulation to optimize a airfoil shape. The earliest accounts of FFD techniques in aerodynamic shape optimization were investigated also by Jamshid [43]. The major criteria for the selection of surface parameterization methods are surface smoothness, local control, analytical sensitivity , grid deformation, re-usability of grid and connection of CAD model which are still used in current studies however the early studies preferred CAD based shape deformation methods over FFD box method which was taken up as a

comparative study by Nitish et al. for turbomachinery applications and concluded in favor of FFD as the better of the two [44]. Parameterization and optimization methods were considered by Tokuda et al.[10] for major applications of turbomachinery such as compressors, turbines, etc as effective means of improving design.

The term aerodynamic shape optimization in the beginning, was synonymous to 2D airfoil optimization only, whether with respect to selecting the optimum performing airfoil for the wing section or tailoring the airfoil shape for specific flight conditions. The earliest studies available in this field were done by Lighthill [45] around the end of WWII however the classical 4-digit NACA profiles as shape parameters were already in vogue much earlier. Later in 1978, a mathematical formula called a Bump function for shape parameterization as tool was employed by Hicks and Henne [46].

However the pace of progress in shape optimization as compared to other dominant fields in aerodynamic, was slow due to various reasons such as flow complexity, non-linearity of mathematical models, prohibitively large number of design variables and lack of accurate models to describe objective functions in terms of design variables. Resolving an airfoil shape into geometric parameters was done by Sobieczky in 1998 [47] and later by Shahrokhi et al. [48]. Sobieczky introduced the PARSEC code which parameterizes airfoil with respect to several geometric features such as camber and angles at the edges. When implemented on the airfoil for optimum lift or drag as the objective the optimum shape is obtained from varying the geometric parameters as the design variables. As late as the end of 20th century, near-accurate formulation of drag as functional was done by Epstein and Peigin [49] [50] for lifting bodies which were then used for shape optimization. Nevertheless, Jameson [51] gets the credit for deriving the Navier-Stokes equations for optimization as subset of control theory. Hence shape optimization based upon flow solution commenced which included all fluid mechanics application including aerodynamic shapes. This work is important also because of the fact that during 1980s, CFD was developing into a primary tool for solving flow problems. There are several optimization methodologies however broadly speaking they can be classified under two families: gradient based optimization and stochastic optimization methods.

Dulikravich [52] pointed that gradient based method algorithm is suitable for lower

number of design variables since less number of gradient vectors are computed. Therefore traditionally, in order to manage a larger number of variables GA are more economical. Steepest descent, conjugate gradient, and sequential quadratic programming are examples of gradient-based optimization techniques. They can be efficiently used for finding the local optima however the systematic formulation of finding a gradient is laborious in seeking the global optimum. Thévenin and Janiga [41] have discussed in details a number of topics such as stochastic optimization, which are employed for engineering applications. Stochastic optimization methods, employs a certain random distribution in the optimization process to evade getting entrapped in the neighbourhood of a local minimum. Accordingly GAs are global optimization methods directly inspired from the Darwinian theory of evolution of species. They require the evolution of a certain number of possible solutions, also called population (Np). Similarly, a surrogate model as given in general definition by Wikipedia [53], is an engineering method used when an outcome of interest cannot be easily or directly measured, therefore a model of the outcome is used instead.

Gradient based algorithm on the other hand were previously considered inefficient with higher number of design variables that succumb to high computation time during calculation of gradient vectors using finite difference format, which is not necessary at all in genetic algorithm and which were therefore favoured for high number of variables in which the gradient vector computation is non-essential. In the beginning of this century an upcoming method called adjoint method gained popularity which would soon replace finite difference for gradient calculation specially due to its unique treating large number of variables with relatively low cost. Dwight [54] categorized the gradient methods applied in the sensitivity analysis into several techniques, which are: finite difference method, discrete adjoint method, and continuous adjoint method.

In discrete adjoint, the governing fluid flow equations along with objective function gradient are discretized and then these discretized equation are operated upon by adjoint sensitivity analysis. On the hand in the continuous adjoint, the adjoint operation is done before the equations are discretized. Both methods have proved to be equally effective however discrete method found a wider preference among users.

In 1999, Anderson and Venkatakrishnan [55] published their study, using the

continuous type, in which they analytically formulated the whole sequence of steps from conservative equations , adjoint calculation and discretization finally applying on mesh deformation for a airfoil shape. Fabiano et al. discussed unstructured mesh and application in discrete adjoint formulation [56]. In this study, a continuous adjoint formulation has been used to derive the adjoint system of equations. Accordingly, the adjoint equations are derived directly from the governing equations and then discretized. This approach has the advantage over the discrete adjoint formulation in that the resulting adjoint equations are independent of the form of discretized flow equations. The adjoint system of equations has a similar form to the governing equations of the flow and hence the numerical methods developed for the flow equations can be reused for the adjoint equations.

In terms of enunciation of the theory the book on CFD based optimization by Janiga is noteworthy [41]. The underlying principles and the equations involved are explained in details under collection of diverse topics covering all major aspects. The initial chapters describe the general scheme of processes employed for CFD optimization. Nonetheless its early days optimization for large design space using gradient was not much in usage. A comparison of these gradient techniques was carried out by Wang and He [57] in which computational cost was taken as the criteria of comparison. The cost was found directly related to the number of design variables, therefore classical gradient-based methods such as finite difference were regarded as unfeasible for aerodynamic optimization due to design space consisting of large number of surface points. Another conclusion was that the adjoint method has an advantage over finite difference because its computing time does not depend on the number of design variables; however till 2008, when the report was published, this method was judged to be complex due to counter-intuitive nature of results [57]. Nevertheless, with the advent of improved techniques in adjoint methods such as algorithmic differentiation implemented into available codes and advancements in computational resources has increased popularity of the adjoint gradient methods. Artificial intelligence and machine learning was already employing Automatic Differentiation AD for neural networks as informed by Thévenin and Janiga [41]. Automatic Differentiation is a collection of techniques to obtain analytical derivatives of differentiable functions, in the case where these functions are provided in the form

of a computer program. Instead of using a mathematical representation, explicit or implicit, of these functions, AD uses the computer program itself as the basis to compute the derivatives such as TAPENADE. TAPENADE was presented in a paper by Hascoët and Pascual [58] which is an Automatic Differentiation tool that takes input as a code written in Fortran or C code and outputs a new code that computes its tangent or adjoint derivatives and also Hessians [59]. Formally, Automated Optimization (AO) is defined as the method to integrate the computer-aided design (CAD) model, numerical analysis (fluid dynamics and/or structural mechanics), and optimization techniques in a single framework. Palacio and team developed AO in SU2 and based it on adjoint gradient method and shape parameterization [60]. To start the automated optimization procedure, first the design variables are selected. Selection of design variables is an important task in the whole procedure and must be carried out only with a proper understanding of the problem. Only those design variables should be chosen that have the most effect on the performance of the system. The efficiency of the AO mainly depends on the number of design variables used for the model. Therefore, choosing unnecessary design variables might decrease the efficiency of the system. With the help of numerical simulation, the constraints and objective functions are calculated and sent to the optimizer. The optimizer can use different optimization algorithms to find out the optima. Different case studies are mentioned later on the optimization algorithms used in literature. Once the result from the optimizer generates the optimum result, the process is terminated, or else different values of design variables are chosen and the whole cycle is run again until an optimal result is obtained. The Sequential Quadratic Programming SQP method is used for mathematical problems where the constraints and the objective functions are differentiable.

Aerodynamic shapes are by no measure simple but are infact complex and possess subtle geometric architecture. Wings, turbomachinery, intake and geometries of nozzles are modelled using mathematical tools called Parameterization. A detailed description of the underlying theory of aerodynamic shape parameterization was given by Kulfan [61]. To quote as an example, an airfoil shape can be modelled in a number of ways. The most straightforward way is called the discrete approach whereby the shape is described using a large set of points of known space coordinates.

This however requires a huge amount of design variables in order to guarantee a smooth and accurate airfoil shape. Additionally, modifying the airfoil shape by changing the positions of the individual points is counter-intuitive and has no real physical meaning. In order to limit the amount of design variables, an airfoil section can also be modeled as a curve. Such a curve can be described as a parametric equations composed of polynomials. To further develop interest in the topic , an early survey of different shape optimization was done by Jamshid in order to select the most suitable mathematical formulation specifically to parameterize airfoil [43]. One way to increase the complexity of a curve is to increase the order of the polynomials. A type of curve that makes use of this principle is the Bezier curve [42]. Another way is to combine multiple low order polynomial curve segments by B-splines that together form the shape shape. The B-spline curve is a piece-wise collection of Bézier curves which is used when a single Bézier curve cannot be used for the shape due to complexity. The amount of information required to define a 3D aerodynamic

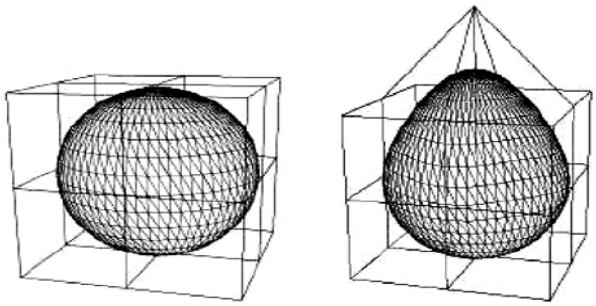

Figure 1.8: *Illustration of FFD based shape deformation [6]*

shape using classical B-spline curves is still quite large to handle. A more compact method is Non-Uniform Rational B-spline or NURBS curves introduced for CAD by Farin [62]. Later, Schramm et al. successfully employed different configurations of B-spline including NURBS for shape optimization purposes [63]. Another method is the "Feature Based CAD" in which a complex geometry is modeled by a hierarchy of commands with the purpose to capture the intent of the designer. Different shape modeling tools are employed including Booleans and B-Splines. The final shape is composed of all the features used in a certain hierarchical order therefore the features are available for parameterization. The turbomachinery community has particularly showed its interest in feature based CAD for shape optimization specially of turbine blades and the community of CAD users claimed to state that

by using this technique "design has returned back to CAD" Jamshid stated [42]. A more advanced technique is "Free Form Deformation FFD" box technique which was already vogue in computer graphics since 1980s and can deform surface primitives such as planes, quadrics, parametric surface patches, or implicitly defined surfaces [64]. The deformation can be applied both globally or locally. The latter deformation type can be imposed with 1st or 2nd degree of surface derivative continuity. It is also possible to deform a solid model in such a way that its volume is preserved. The scheme is based on trivariate Bernstein polynomials which were introduced by Barr [65], and provides the designer with an intuitive appreciation for its effects. Lattice defined by the Bernstein polynomials ensure that by just moving one control point in one direction will allow the smooth deformation of all the surface.

The FFD techniques defines a deformation field over the space embedded in a lattice which is built around the object. By transforming the space coordinates inside the lattice, the FFD technique is able to deform the enclosed object. An added advantage is that the computational grid used for CFD can also be deformed simultaneously to conform to the new shape of the object ; whereby any type of grid can be possibly employed. Spring analogy is compatible for volumetric deformation of the grid and will be discussed later. The earliest accounts of FFD techniques in aerodynamic shape optimization are found in investigations by Jamshid [42] [43]. Chauhan and Duvigneau performed wing shape optimization using FFD box including twist as an additional parameterization [66].

Earlier, Duvigneau had studied FFD box for aerodynamic shape optimization and presented for the HAL forum in 2006 [67]. Since parameterization techniques are selected for the following criteria: surface smoothness, local control, analytical sensitivity , grid deformation, re-usability of grid , based upon which Nitish et al. [44] did a comparative study between feature-based CAD and FFD for shape parameterization of turbomachinery according to the aforementioned criteria. The conclusion was in favor of FFD as the better of the two techniques . FFD is also implemented in SU2 for both 2D and 3D shapes. Kline et al. performed shape optimization of hypersonic inlet using 2D FFD box [68]. The mesh obtained from mesh generator is imported as .su2 file and then it is embedded with the information of the predefined FFD Box control points [69]. Subsequently after the surface of the

body is deformed, the volume mesh is adjusted as well by the spring analogy.

Spring analogy based volume mesh deformation is the enabling technique to close the problem of shape optimization by adjusting the volume mesh governed by changes to the surface deformation. Mesh deformation is also applied in FSI problems and transient problems in CFD. The range of variation can be from negligibly small to total design transformation. In adjoint based aerodynamic shape optimization this design change is governed by the sensitivity analysis of the objective function on the geometry. Region of high sensitivity will undergo larger shape change and control the outcome accordingly. This opens a whole new avenue in this field and increases the levels of complexity since the boundaries of the shape surface when altered, will consequently vary the volume mesh nodal location however nodal connectivity are required to be kept intact. According to Lin et al. [70] there are two basic ways that it can be done: Firstly by creating a new mesh every time the geometric surfaces deforms, secondly by using a meshing tool or mesh automatically deforms. A hybrid method is also possible which is combination of the two.

As former is usually manual the latter is almost always automatic and requires codes built upon robust techniques based on theory of structural mechanics of spring or molecular lattices and this analogy is widely accepted as the basis of such codes [71]. Dwight preformed volume mesh deformation for a number of aerodynamic problems including 2D airfoils and 3D DLR wings, demonstrating large shape changes and as a consequence significant volume mesh deformations were obtained. This study claims to perform probably the first scaled deformation and can be used for any application such as unsteady aerodynamic or shape optimization [54]. The theoretical implementation of the spring analogy for mesh deformation is done mathematically using various types of solvers which may use PDEs, physical analogy methods, algebraic methods, or hybrid of these all techniques [72]. There are several different methods under spring analogy [73]. Spring analogy is the most popular used method for mesh deformation codes due to simple and robust theory and ease of implementation. Vertex Spring Method considers each edge as a spring that obeys the linear Hooke's Law. The equilibrium length of the spring is zero. The equilibrium can be achieved by putting sum of all forces passing a node surrounded by neighbouring nodes to zero. The new location of each node is obtained from

iteration while applying Dirichlet boundary fixes the node location for each iteration [74].

1.4 Shape Optimization on Subsonic Intake

Intake as part of both propulsion and aerodynamic system is a subject of shape optimization since its beginning. Supersonic intake have remained in the limelight of most CFD studies due to most advancements occurring in the field of high speed aerodynamics. A summary of the studies performed on the design optimization for high-speed intake can be found by Knight [75] [76] [77] . The design objectives for intake shape were predominantly related to the intake exit condition at the AIP such as total pressure recovery factor and flow distortion. Together they both account for the quality of the air output by intake. Zha et al. optimized an axisymmetric mixed compression ramjet intake at Mach 4 and 18.3-km altitude where the objective of the design was to maximize total pressure recovery factor [78]. One of the earliest intake shape optimization using CFD was done by Reddy and Reddy for a nacelle lip taking AIP Mach number as the objective function [79].

Lefantzi and Knight emphasized the complex three-dimensional flow separation in the bump by means of flowfield visualizations [80]. Blaize and Knight [81] and Blaize et al. [82] employed a single-objective algorithm to maximize the total pressure recovery factor of a two-dimensional supersonic intake for a single flight point and an entire mission . They used GADO24 and obtained 20–30 % improvement in total pressure recovery factor of the supersonic intake. A similar design methodology for a three-dimensional supersonic intake was performed to achieve maximum total pressure recovery factor at a single flight condition [83] [84]. Using different shape optimization techniques, supersonic intake can be optimized and pressure recovery losses can be greatly reduced. However subsonic intake do not experience large total pressure losses due to shock formation as in supersonic intake, and subsonic intake usually have pressure recovery of around 90% or more. A mere few units increase of recovery factor are possible to achieve through shape optimization. Subsonic intake for most part are Pitot type and the shape optimization of the subsonic intake, in essence is related to improving the s-duct geometry but

the earliest subsonic intake shapes were optimized for the lip geometry as well [79]. The s-duct is the mandatory part of any intake and many studies are solely devoted to the improvement in s-duct design. In 1993 Wellborun and Okiishi generated aerodynamic data for compressible s-duct intake configuration [85]. They conducted experimental tests and numerical solutions to understand flow phenomena in s-duct intake and validated the computational codes. Numerical solutions are obtained by using parabolized Navier-Stokes equations. The aim of this study is to provide benefits to aircraft intake designers by presenting validated computational works with experimental test data. Secondary flows in the s-duct intake are also investigated in this work. Several others continued to use the results from their work to validate their own research on s-duct [86]. Reddy [79] found optimum intake by using ADS Automated Design Synthesis code that is interfaced with CFD solver and grid generation code. For s-duct subsonic diffusers, a Gaussian bump located upstream of the separation region showed an improvement with respect to flow distortion at the AIP . An automated design loop was employed using a flow solver in step with an optimizer [87] [88]. Zhang et al. [87] explained the performance improvement seen in the diffuser by the suppression of detrimental secondary flows as a result of surface modification which redirected the flow. Later Zhang et al. [88] performed a multidisciplinary and multi-objective optimization by parameterizing the S-shaped intake and aerodynamically improved this baseline intake by integrating CFD computations with numerical optimization methods . This is a particularly interesting study since it was concluded from the multi-objective and multidisciplinary results that in order to optimize both RCS and pressure recovery the conflicting nature of both objectives compromised on the outcome. The improvement in total pressure at AIP is found less than 1% for most shape optimization studies therefore DC is a noteworthy parameter and is shown to improve by almost 80% in studies by Knight and Zhang on s-ducts. Similarly, Berrier et al. [89] conducted an experimental research of a flush-mounted, s-duct intake which ingested large amounts of BL flow. In addition to experimental study, they incorporated computational studies of this intake by using Navier-Stokes solver OVERFLOW to direct their aim to present a database for CFD tool validation on this type of intake and provide a baseline intake for future intake flow control studies. Loeper and King [90] also studied the effects of five different parameters of s-duct intake on its performance numerically such as duct

length, vertical offset distance, expansion ratio of the cross-sectional area, aspect ratio of elliptical entry and Mach number at entry. Gan and Zhang [91] improved aerodynamic performance of the s-duct by using the centre-line's curvature and the cross-sectional area ratio as design variables and in comparison with baseline design, the flow distortion coefficient is reduced by 16.3 % and the total pressure recovery factor increased by 1.1 % on the flight conditions at design point .

Finally some discussion on submerged intake which is the intent of present study. Initially several works were directed in the possibility of employing such intake for primary air supply. The preliminary research on the 3D shaped NACA intake was experimental using wind tunnel models as well as real flight tests and performance based on geometric parameters was completed during the early days of jet age as aforementioned in section 1.1. The complete range of design parameters as estimated in [1] [3] such as size , ratios and angles, provide a geometry that is optimized and is still used verbatim for auxiliary and other applications. However, the optimum performance was based upon the pressure outlet and ram recovery at the AIP as the primary objective and no other objective was ever considered such as lift or RCS. In the years following the final shape of the NACA intake, there is a dearth of any significant study on shape optimization and this negligence continued well after the CFD revolution took off in the 1990s. The low pressure recovery, due to ingested boundary layer, was one of the reasons of abdicating it in favour of pitot-type. He and Li [92] found 93.6% pressure recovery at subsonic cruise speeds from CFD studies which were in match with the previously attained values from flight tests. The ingested boundary layer can be deflected by various techniques such as by raising the intake above the line of boundary layer or by giving a component of swirl to the flow containing boundary layer using some device such as "vortex generator VG" and aerodynamic grid. Perez [32] used a delta wing shaped VG upstream to entrain flow into the intake cavity. Out of seven configurations, the best performing VG achieved 57.5 % increase in total pressure however drag increased by 93.6 % hence inadvertently taking away the only advantage a flush intake has over pitot type .

Ruetten [39] however mounted a vertical VG pair attached just upstream of the NACA intake fore lip. Shape deformation techniques were employed before becoming in vogue in adjoint based shape optimization therefore a manifestation is

found in this very study. FFD box method for shape deformation was used to rotate VG about its vertex upstream of the intake. Different configurations were numerically tested. Almost all VG uniformly improved total pressure by 5 % however drag increased from almost 0 to at least 6 drag points. A very important study available which comprise of an optimization method for performance enhancement of flush intake was done in 2015 by Lombardi [93]. The study used Genetic Algorithm for optimization which employed CFD solver to optimize the divergence angle and not surprisingly this study corroborated previous studies done in the 1940s. The optimum performance of the intake was at pressure recovery of 0.855 for ramp angle of 7° and 97% divergence (corresponding to 2° divergence angle). Sun and Guo [4] studied flush intake numerically. They determined three significant parameters side edge angle, ramp angle and parameter of aft lip and later studied the effects of these parameters on the intake performance both experimentally and numerically in 2007 [23] in an effort to enhance submerged intake performance with flush mounted planar side entrance. The trapezoidal shaped intake operated at Mach 0.7 was found to perform optimally at pressure recovery of 0.915 for a ramp angle of 23 ° and side edge single of 4°. The characterization process was carried out experimentally also showed that the initial geometry gave pressure recovery less than 0.9. Taskinoglu and Knight studied submerged intake on slender body and employed multi-objective optimization using trade-off or ϵ-constraint method for finding the Pareto optimal set [26] [27]. A fin was placed inside the s-duct of the intake and the variables of the study were its geometrical parameters i.e. fin height, length and incidence angle. The objective functions of the optimization problem were taken as distortion and swirl indices over the AIP. The principal benefit of the fin is the generation of a large tip vortex within the intake, which substantially modifies the flowfield. The distortion index was minimized using two intake configurations and was observed to be reduced by 25% and 70% at the expense of a substantial increase in swirl index in the two intake respectively. In a study by Joon et al. [94] on flush intake, adjoint based shape optimization of VG was placed inside duct which improved the distortion coefficient by VG however the pressure recovery remained principally unchanged. SU2 as open source CFD tool is being employed for shape optimization as early as 2008. Kline who is now one of the lead developers of SU2, applied continuous adjoint method to shape optimize a hypersonic intake design for a PhD thesis and subsequent

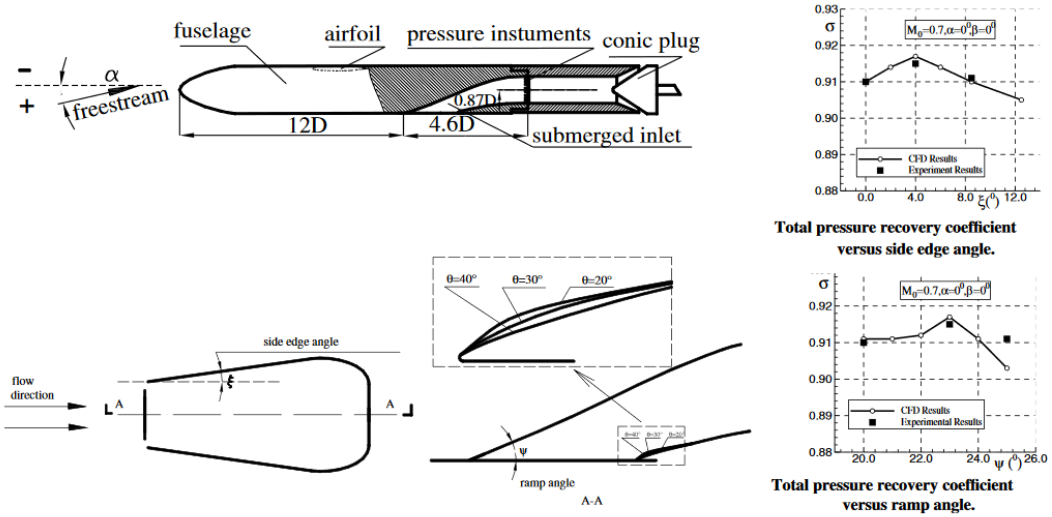

Figure 1.9: *Shape characterization of trapezoidal submerged intake by Shu Sun et al [4]*

research from Stanford University [68].

The dissertation by Kline contains the complete details of the continuous adjoint equations for a generalized outflow-based functional, a framework that utilizes this generalized functional to find the surface sensitivity for objectives and enables multi-fidelity flow path design. Multi-objective adjoint optimization utilizes the principle of superposition to combine already-implemented functional. The discussion of adjoint based optimization techniques using SU2 must not end without mention of Albring , Sagebaum and Gauge [95] who presented the automatic or algorithmic differentiation technique and its implementation for discrete shape optimization by illustrating examples of both inviscid and viscous cases. The developers used Expression Template a C++ meta-programming technique to improve the efficiency of the operator overload in the calculation steps of AD.

1.5 Intake Performance Parameters

A properly designed intake benefits both the vehicle aerodynamic performance as well as engine performance. Intake design is based upon the operational requirements of the aircraft. A subsonic commercial aircraft is intended to fly a major portion of its operational hours at cruise flight conditions, with a mission of simply transporting commuters and cargo. However a military jet is capable of executing

multi-role capabilities and therefore its intake must be able to handle different engine requirements. Primarily the mass flow rate for thrust generation by engine must be fulfilled for which the size shape and location of intake on the air frame is crucial. Then while the required mass flow is being delivered, the intake customizes the flow to the needs of engine which generally performs at optimum for Mach number at AIP of about 0.3- 0.5, and total pressure equal to the free stream total pressure for ease of compression and minimum flow distortion. However, while the flow rate of air cannot be compromised the air quality i.e. the total pressure and uniformity may deteriorate to an extent due to factors such as shocks and friction which generate boundary layer, shock-boundary layer interactions and separated flow inside the intake.

The design of the intake should minimize these losses therefore performance evaluation is necessary. The correct choice of parameters and their measurement are deterministic for selection of type, shape optimization and sizing of the intake. Its worthwhile to mention here that the improvement in one performance parameter may compromise other parameters. The classical intake performance parameters as in standard literature are:

- Total pressure recovery factor
- Distortion coefficient
- Drag

1.5.1 Total Pressure Recovery Factor

Pressure recovery is the most common objective function in intake optimization studies. It is the ratio of the total pressure at AIP to that at freetream. Compressible effects are experienced by intake in vehicles moving at Mach number greater than 0.3. Total pressure in free stream can be available as the static pressure at AIP and air can be delivered to the engine by the intake at this pressure if it is theoretically brought to rest isentropically. However due to losses such as lip separation, duct friction, shocks, due to the diffusion process of the intake, the recovered pressure is less than the total free stream pressure. Hence the measure of the intake efficiency is

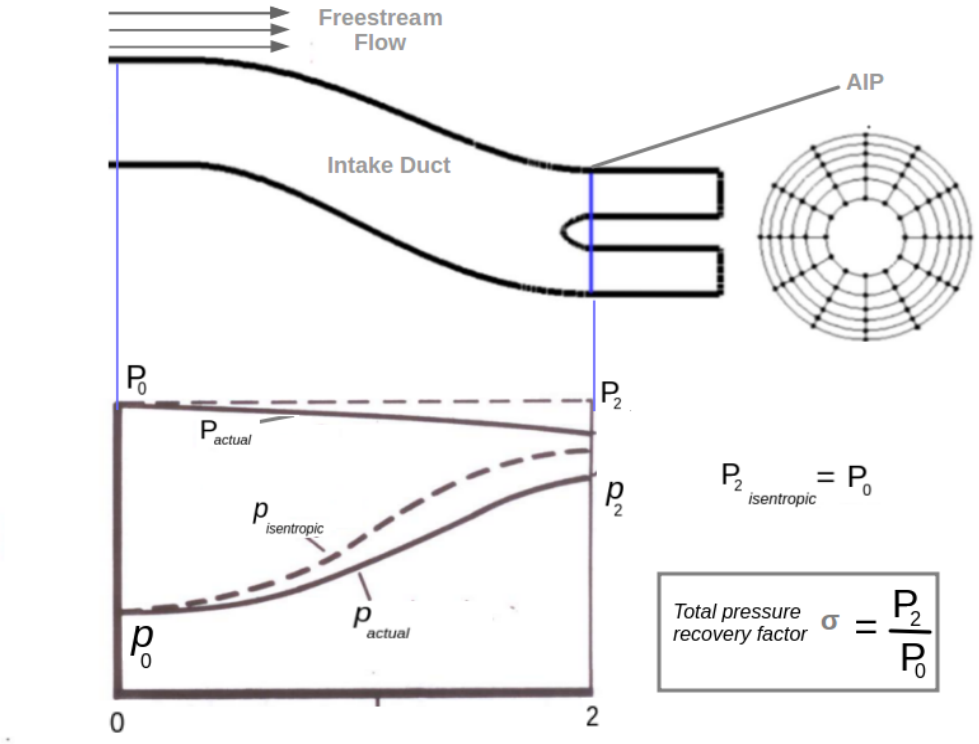

Figure 1.10: *Total pressure loss and static pressure rise along intake length [7].*

the ratio of the total pressure recovered at the fan face or AIP to the free stream total pressure also called the "total pressure recovery factor σ" [7]. Another parameter is also used in literature called the "Ram Recovery Coefficient" which is the ratio of dynamic pressure at AIP to the freestream dynamic pressure.

1.5.2 Intake Distortion Coefficient DC (θ)

The quality of air delivered by intake to engine is defined by the level of distortion or non-uniformity of total pressure at the AIP face. Total pressure distortion has many causes which can be both internal and external. DC (θ) is given by the equation:

$$DC(\theta) = \frac{P_2 - P_{2\theta min}}{0.5\rho {V_0}^2} \tag{1.1}$$

The main cause of distortion are high local duct curvatures, compression along duct and BL bleeds and other flow control devices. Oates [96] gave the external causes of distortion as the following: flowfield angularities due to angle of attack and angle of yaw, carry over BL from fuselage and appendages such as wings, canards, antennas, flow measurement devices etc. The problem of distortion as aforementioned is that

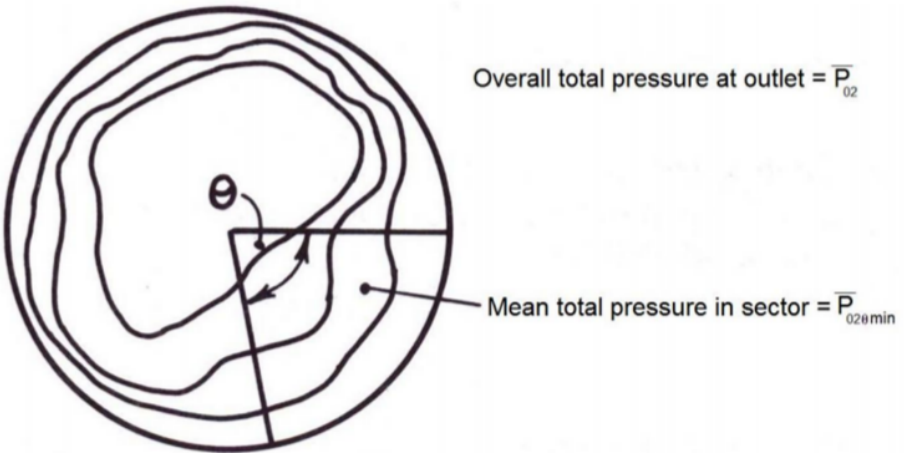

Figure 1.11: *Distortion coefficient DC (θ) at the AIP [8]*

of integration. Hence the compressor surge line shifts towards a lower pressure ratio for a distorted flow at AIP compared to an undistorted flow.

1.5.3 Intake Drag

The intake drag can be considered as both part of the overall vehicle drag and the component drag. The installation of the intake on the air frame must ensure minimum drag [97]. The shape component of drag is minimized by sizing the intake to the desired air flow rate of the engine and optimizing the shape to reduce the drag coefficient. But this is the case if the intake is protruding out of the fuselage. The cowl generates the negative pressure force or additive drag in non-submerged intake. However in the case of fully submerged intake the shape component of drag will be reduced. This key point elaborates the importance of a fully submerged or flush intake. Flush intake by virtue of being embedded into the surface of the vehicle do not generate shape drag. The only drag a fully submerged or flush intake generates is the the friction along the duct.

1.6 C_L/C_D as an Objective Function for Submerged Intake

The problem of intake-air frame integration and performance optimization is under exhaustive study for supersonic and hypersonic vehicles since Busemann developed the oblique shock wave air intake in 1944 [98]. Historically, the lion's share of

studies have been on supersonic intake which utilise shock waves for both air intake diffusion to increase thrust and creating high static pressure on intake upper surface to generate lift [99] [100]. Hypersonic vehicles such as scramjets and waverider were specially studied and advancements were made in all related practical fields [101]. Consequently, subsonic intake were largely neglected in this regards.
The inherent geometry of the flush intake allows the flow to be tangential to the surface. It is observed that a considerable negative pressure coefficient develops along the ramp of the intake which can possibly generate lift. The observation is already made in the initial studies by Taylor [12]. The intensity of negative pressure coefficient on the ramp surface is greater than the basic fuselage surface indicating generation of additional outward normal force along the ramp. Recently in a study done by Pignier [5] on the DES simulation of acoustic effects of NACA intake similar trends of negative pressure coefficient were observed. In the present study these non-uniform pressure distribution along the ramp surface are considered and it is suggested that it can give overall lift force on being integrated along ramp surface. It is also noticed that the increase in velocity ratio V_1/V_0 increases the negative pressure coefficient region.

1.6.1 Vortex Lift

As part of the overall literature survey and in order to augment the numerical study, a review of some recently established aerodynamic concepts around vortex lift is worth mentioning before proceeding to the methodology and result sections. During the 1960s it was observed that the extra lift generated from the delta wings specially at high angle of attack was inexplicable by the potential flow theory for attached flows. The reason for that is that the delta wing apex and the sharp leading edges generate vortex pair which increase the Cp distribution near the edges due to a reattachment line along the edge and the suction is directed normal to the edge instead of tangential directed hence producing additional lift .

This additional lift is called "vortex lift" and it is predicted with the "leading edge suction analogy" by Polhamus [102]. For a profile with a sharp leading edge a free vortex forms . This vortex creates a suction force which will now be normal

to the surface as opposed to the leading edge tangential force if the flow remains attached. Polhamus predicted the lift force as the sum of two distinct forces: the lift from potential flow theory and the additional lift from the free vortex. The sharp corner which causes the flow to separate and vortex is spun around the edge is of vital importance in the creation of the additional lift. If there is a mechanism that reproduces the same vortex sheet spinning around the sharp edge lift force can be created by virtue of the same reattachment and Cp distribution as seen in delta wing case. According to Hoeijmakers [103] under influence of the vorticity contained in it, the free shear layer rolls up in a spiral fashion to form a relatively compact single-branched core with distributed vorticity, the so-called leading-edge vortex. The study for the possibility of generating these type of vortex sheets in a range of subsonic flow regimes is done in detail by Lamar [104]. Thus theory supports the generation of additional lift for both supersonic and subsonic flows due to vortex emanating from sharp leading edges of the delta wing and extrapolation of this phenomena to a flush intake, which also behaves similarly, is an overlooked possibility. In the case of delta wing, vortex pair is due to leading edge separation at higher angle of attack whereas in the flush intake, its due to the ramp geometry which is inherently at an angle relative to the flow. The latter depends on the engine aspiration, hence the vortex pair is already existing at zero angle of attack with respect to the body and therefore it is possible to achieve lift.

1.7 Motivation and Problem Definition

Submerged intake is currently being used as a secondary air supply component in many aircraft and not many applications seek its use as primary air supply for engine. The current study seeks to broaden the horizon of research and of converting it into a primary component i.e. in order to supply air to the engine requires improvement in existing design as well as finding new parameters which will strengthen the position of submerged as a better candidate viz-a-viz other types of intake currently in application. Another motivation of the present study is to address the issue of solving the problem of submerged intake with respect to shape optimization. The geometry is optimized with regards to the total pressure recovery at the AIP, as the

main objective so as to be competitive in the quality of air supplied to the engine. In addition to pressure recovery, the lift generating property of the submerged intake is also investigated. Some effort to improve AIP distortion is also undertaken but it is supplementary to the pressure recovery optimization. Therefore as the objective functions in the present optimization, total pressure recovery factor and C_L/C_D are the primary considerations. The advent of new open source CFD platforms like SU2 have provided opportunities of exploring a large number of problems such as adjoint based shape optimization. The present study focuses on subsonic and transonic flow modeling of submerged intake integrated into symmetrical bodies. The performance evaluation using SU2 and comparison with established results in literature is also an aim of this study and therefore it is sought in the study for end-to-end open ware resource utilization.

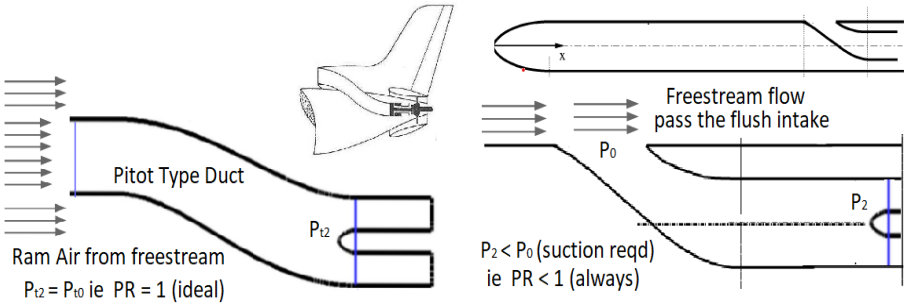

Figure 1.12: *Pitot intake vs. submerged intake.*

1.8 General Flow Considerations - Pitot and Submerged Intake

Some general differences in flow characteristics are considered and mentioned here with respect to pitot and flush/fully submerged intake as shown in figure 1.12.

1. Pitot intake at ideal condition total pressure recovery factor =1.0 as the air rams and stagnates at the AIP.

2. For Mach number at and less than 0.3 static and total pressure are almost equal.

3. In flush or fully submerged intake the air flow passes tangentially to the opening and therefore will not attain freestream total pressure value at AIP hence total pressure recovery factor < 1 due to absence of ramming effect.

1.9 Outline of the Thesis

In the present part of the study, the shape optimization of three submerged intake is undertaken: NACA-type generic flush intake mounted on a flat plate trapezoidal entrance flush intake on a slender body and a circular intake on a similar slender body. The flow regime for all cases is subsonic to transonic in the range of 0.6-0.7 Mach number. The optimization study is undertaken with respect to the objective functions of lift, total pressure at AIP and drag. The study realizes the complete design optimization cycle for the mentioned cases. The cycle begins with the generation of the baseline geometry and mesh and obtaining a primary solution. Hence CAD modeling , mesh generation and direct numerical solver are prerequisites. To meet this end, the open source modeling tool SALOME with, Python dump script option, is used for initial surface generation and generating a Boolean cut model of the flow field that includes the outer farfield surfaces as well. The mesh generation is done by GMSH which has both GUI and Python based script for mesh generation. GMSH utilizes prism layer meshing by surface extrusion feature upon which the outer mesh till farfield is resolved by tetrahedral cells hence producing a hybrid mesh. GMSH is also recommended as it writes the .su2 file which can be processed in the following steps i.e. the mesh file containing the geometric surfaces and boundaries is read by SU2 which can be initially processed using SU2_MSH to give the SU2 for flow and adjoint solution and PARAVIEW for post-processing the numerical solution.

FFD box in the SU2_DEF is utilized as the key method of defining design space. The adjoint solver SU2_DOT built-in SU2 runs in consequent manner after direct SU2_CFD solution to give the sensitivity field of the objective function over the surface of intake. This ends the first design iteration. The next iteration begins with the SU2_DEF grid deformation iteration which deforms the surface with respect to the adjoint sensitivities calculated previously as well as the volumetric deformation of the grid. The deformation process includes the surface mesh smoothness and grid cell volume solver as well. This is followed by the next iteration starting with direct solutions on the new geometry. During the course of this part of the study , the implementation of the optimization tools in SU2 such as adjoint or sensitivity calculations, FFD Box modeling and driving the optimization cycle is the major

accomplishment. Single and multi-objective approach are realised by optimizing shape for two objective function that is pressure recovery at intake AIP and/or C_L of aerodynamic body. The drag is included as penalty function which acts as constraint.

1.10 Proposed Methods and Models

It is important to realize that the development of a proper set of tools for the direct numerical problem are the essential building blocks in any numerical study in other words prior to any numerical study, such as adjoint-optimization, the basic tools for the study must be learned thoroughly and a certain level of expertise has to be developed. In the present study the skill set for the job of accomplishing a flow solution are SALOME for CAD modeling, GMSH for mesh generation, SU2 for numerical solution and PARAVIEW for post-processing the numerical solution. This skill set along with the in-built adjoint optimization toolkit of SU2 will form the back bone of the methodology to be followed in the present study. A discussion of the mathematics underlying the shape optimization is also elaborated. Hence details related to basic optimization and adjoint method is added as well as geometric formulation of free-form deformation technique to adjoint optimization is explained for a future reference to the ongoing study. The results are mentioned for four cases. NACA intake on flat plate, trapezoidal flush intake on slender body, circular intake on slender body and trapezoidal semi-submerged intake on slender body.

1.11 Contributions of the Study

- Multi-objective shape optimization using adjoint technique in open-source CFD platform SU2 for subsonic submerged intake design improvement.

- Considering lift as a design parameter for submerged intake.

- End-to-end application of open source platforms.

1.12 Problems Related to Open-Source Software

- SALOME and GMSH are not as user friendly for solid CAD modeling and mesh generation, as are available widely used commercial softwares. However the strict requirements of generating a SU2 readable file can be met by using GMSH.
- The geometry and flow regime poses a few challenges. The intake is seamlessly integrated within the body with outlet BC at AIP. The flow requires RANS 3D solution at Mach number 0.6-0.75 which makes it a multi-regime flow problem.
- In shape parameterization the FFD box method is employed and control point specification using "Point-inversion" requires several iterations of "FFD setting" before a stable configuration is achieved for any particular optimization problem.

CHAPTER 2

METHODOLOGY

2.1 Introduction

The present study undertakes the design optimization of a subsonic submerged intake in which numerical tools are utilised. These tools include the geometry modeling by CAD , mesh generation and refinement, basic formulations of fluid flow using CFD, shape deformation and sensitivity estimation using adjoint methods for optimization. Hence this section puts forwards a background of the methods and the theory involved. The discussion also takes into account the previous studies which have paved the way for the improved techniques which are recently in use within SU2 framework. Hence to touch upon the upcoming tasks, a discussion on the adjoint method with the underlying mathematics of the sensitivity analysis and application of the FFD box for shape optimization is also done.

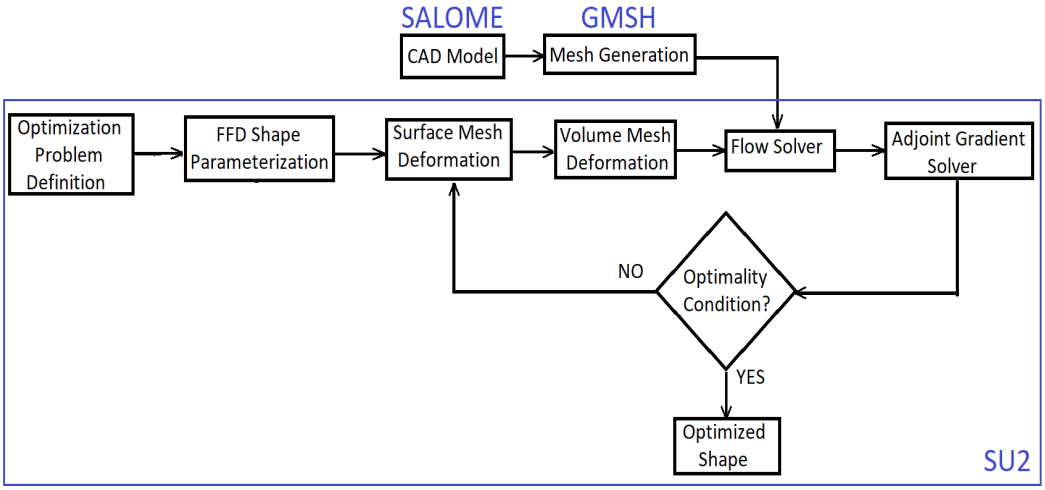

Figure 2.1: *Flow chart of CFD optimization processes in present study.*

SALOME is an open-source software that provides a generic Pre- and Post-Processing platform for numerical simulation. SALOME has open and flexible structure made of multipurpose tools.

- Functions such as Create, modify, import and export to different file formats (IGES, STEP, BREP, ...), improve quality of CAD models such removing repetition in points, edges and improving quality of CAD models.
- Build mesh upon the geometry from CAD; manipulate and work with meshes; inspect mesh quality; import and export mesh files (UNV, DAT, STL, etc).
- Control physical properties and embed them into CAD and geometric items.
- SALOME comes in tandem with SATURNE flow solver and also provides CFD results for number of problems.
- Post processing in the form of fields and vectors

SALOME is a multi-disciplinary platform however in the present study it is employed only for CAD modeling of surfaces and generate Boolean cut solids which are consequently saved in .stl format for mesh generation in GMSH.

2.2 Modeling Geometry in SALOME

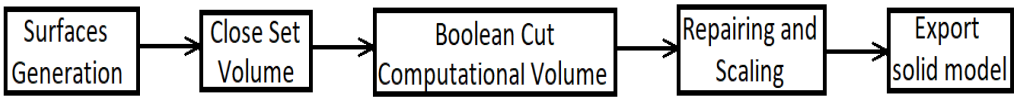

Figure 2.2: *CAD modeling flow chart in SALOME*

The initial step of any numerical problem is a proper, accurate and well-defined set of geometry. SALOME is an open-source CAD software with a python dump script along with GUI and an inbuilt meshing tools as well. The illustration of rectangular flat plate with duct leading from the aft of the intake to the outlet which controls the flow is done. The details of the geometry are given in the benchmark study by Pignier et al. [5]. The coordinates of the divergent intake opening provided in reference

generates the initial 2D sketch which is extruded to a duct depth D=50.79 mm. The intake in reference is shown in figure 2.4.

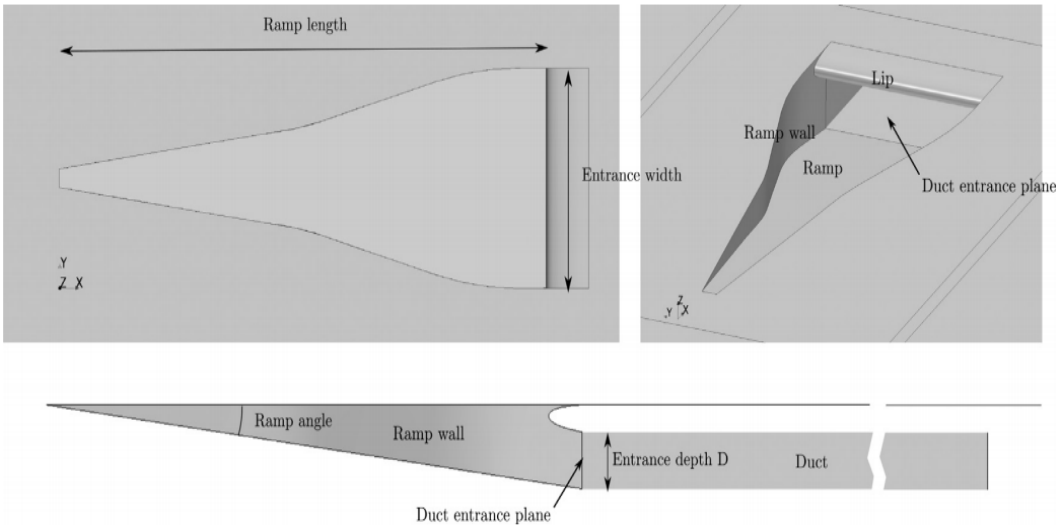

Figure 2.3: *Benchmark geometry based on the reference study by Pignier [5].*

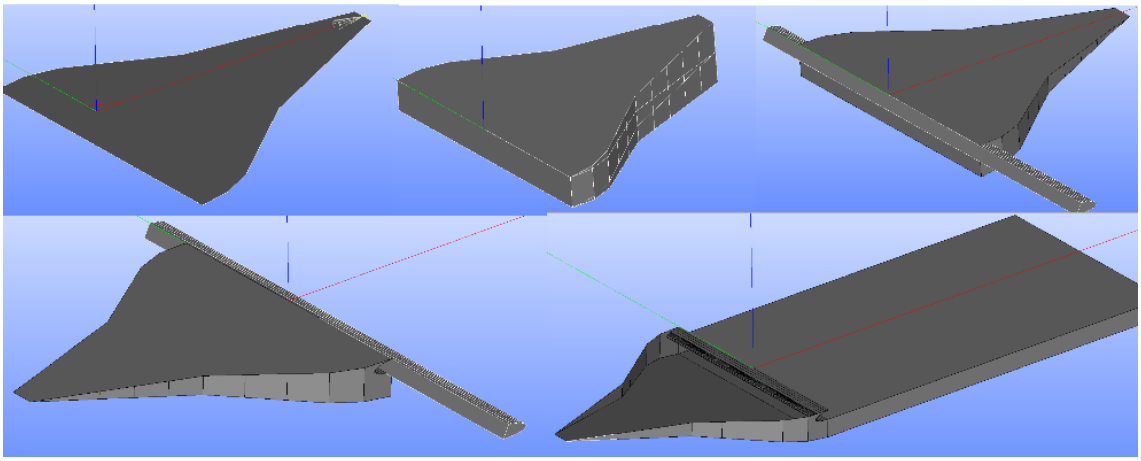

Figure 2.4: *NACA intake modeled using Boolean cutting feature in SALOME*

The extrusion is copied and rotated at 7 ° ramp angle and the corresponding Boolean common of the two give the NACA intake as a solid model. The rear lip profile is then sketched according to the given coordinates in reference and its lateral extrusion is Boolean cut from the top of the base of the NACA intake solid while the uncut base is extruded 1 m in axial direction and finally fused with a box with dimensions of far field. This solid body is exported as .stl file upon which meshing is carried out in GMSH. The individually named parts of the NACA inlet are given in figure 2.3 while the outer boundaries are farfield. The duct outlet is given outlet boundary condition.

2.3 Mesh Generation in GMSH

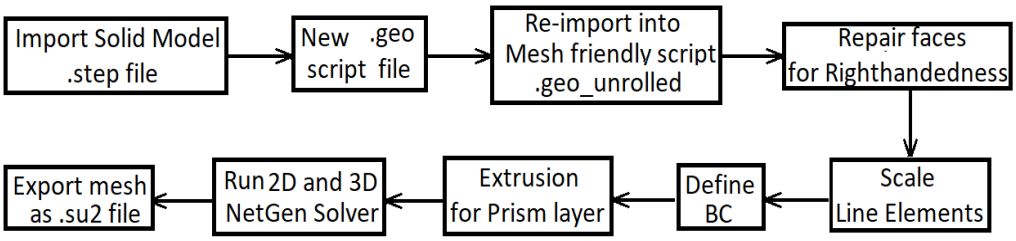

Figure 2.5: *Mesh generation flow chart in GMSH*

Geometry modeling is followed by discretization of the physical model into suitable mesh format. This is accomplished by hybrid mesh generation on GMSH, which is open-source code with dual features of both a GUI and python based script. GMSH generates .su2 mesh file which is readable by SU2 platform. POINTWISE is also capable of producing reliable .su2 mesh files but is a commercial code therefore GMSH is utilized. Basic mesh properties are possible to improve by adaptation. The mesh adaptation feature of SU2 is also utilized which can improve mesh quality for density gradient based cell refinement technique. GMSH is based around four modules: Geometry, Mesh, Solver and Post-processing. GMSH can be used at 3 levels:

- Through the GUI
- Through the dedicated .geo language
- Through the C++, C, Python and Julia API

In the present study, GMSH is used with combination of GUI and .geo dedicated language code. Generation of initial mesh in GMSH requires several steps mentioned as follows:

2.3.1 Creating Mesh-friendly Geometry Script

At the onset of generating a close 3D solid geometry as .stl file, GMSH is launched and the file is opened in it following which it is re-exported into .geo format in the first step and again imported and re-exported into ".geo unrolled" format. This type

of format does not contain the supporting .stl file in fact it unrolls the geometry into basic geometric features of points, lines and surfaces. The points connect to form lines and lines loop to give surfaces. At this juncture the surface normal should be checked and modified according to the inner facing direction as shown in figure 2.6. These surface normal are oriented on the either face of each surface, which, unless not properly allocated will be the reason of error in the volume mesh solver step. While working on the GMSH friendly geometric file further processing is under taken. As a prerequisite the Boundary Condition IDs should be mentioned at this step.

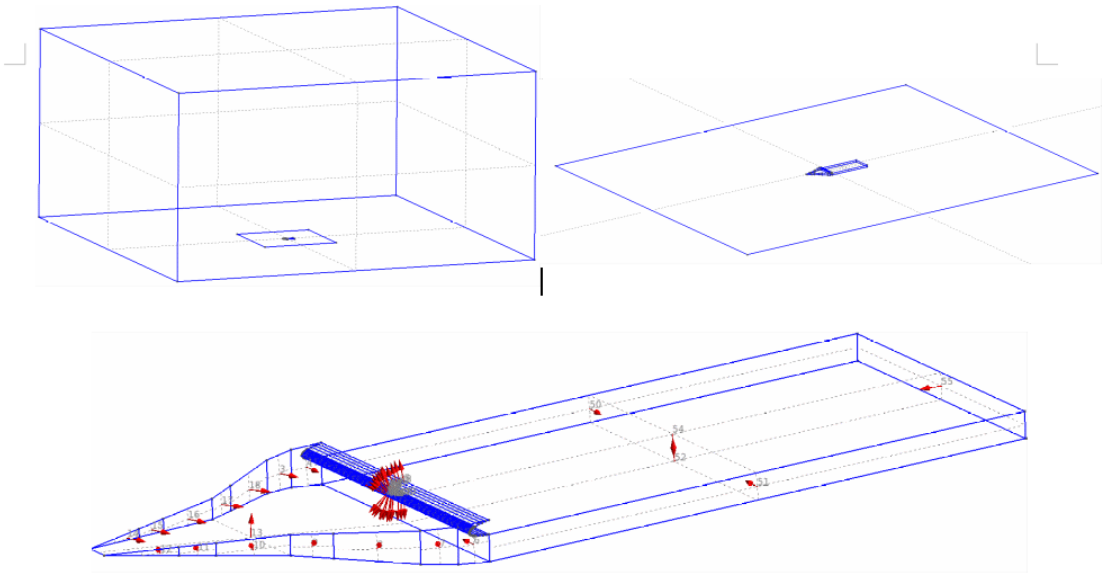

Figure 2.6: *Representation of the solid model as imported in GMSH in .stl format. Note the surface normal vectors in red.*

2.3.2 Mesh Clustering and Boundary Layer Prisms

The GMSH friendly geometric file in ".geo unrolled" format is obtained which contains the complete hierarchy of the model from points up to the volume. Now in the following step the lines are individually clustered using the transfinite curve option whereby the number of mesh points on each elementary curve is defined. The progressive or bump type of mesh point distribution can also be controlled correspondingly in this same command. Following the clustering of 1D components the surface mesh is generated. The present study uses the "Packing of Parallelogram" algorithm for 2D mesh solving with a single smoothing step.

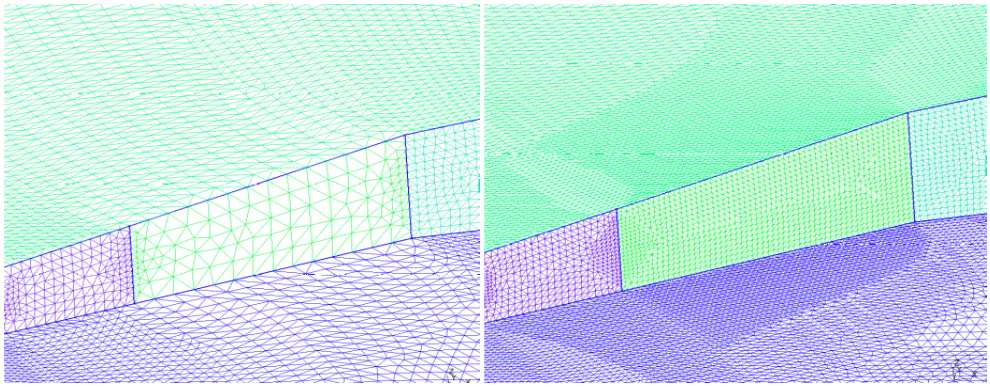

Figure 2.7: *Transfinite clustering to increase built-in mesh size.*

After the boundary layer prisms, the unstructured volume mesh can be generated. This mesh is bounded by the outer most layers of the prism layer volume meshes therefore the surface ID of the 2D elements will be accordingly mentioned in the surface loop command. The "Surface Loop Surface ID command has arguments containing the ID‘s of all the surfaces bounding the volume mesh. Frontal and Delaunay 3D unstructured solver options are both capable of creating tetrahedral elements inside the volume bounded by the surface loop. In this study frontal option is taken.

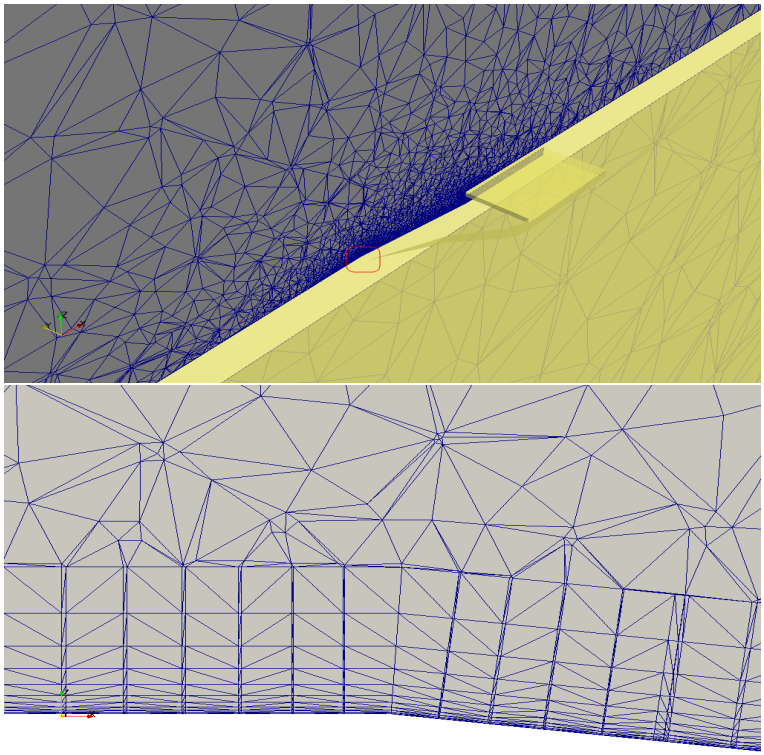

Figure 2.8: *Hybrid mesh with prism layers adjacent to tetrahedral unstructured mesh.*

In the next step, the 2D meshed surfaces are extruded for given number of layers and normal extrusion distance to generate the boundary layer volume mesh as shown in figure 2.8. The "ExtrudeSurfaceSurface ID,Layersnumber of layers,Layer Distance" does the task. It should be noted that the total prism layer thickness is calculated from the flow Reynolds number to resolve the viscous boundary layer and the height of the cell adjacent to the wall is calculated for $Y^+ = 1$. Complete set of calculation is given in Appendix. The growth rate is taken as 1.15-1.25 for consecutive cell height. The last cell of the prism layer is kept of equal sides to optimize transfer of information between the prism layer to outer unstructured mesh as shown in figure 2.9.

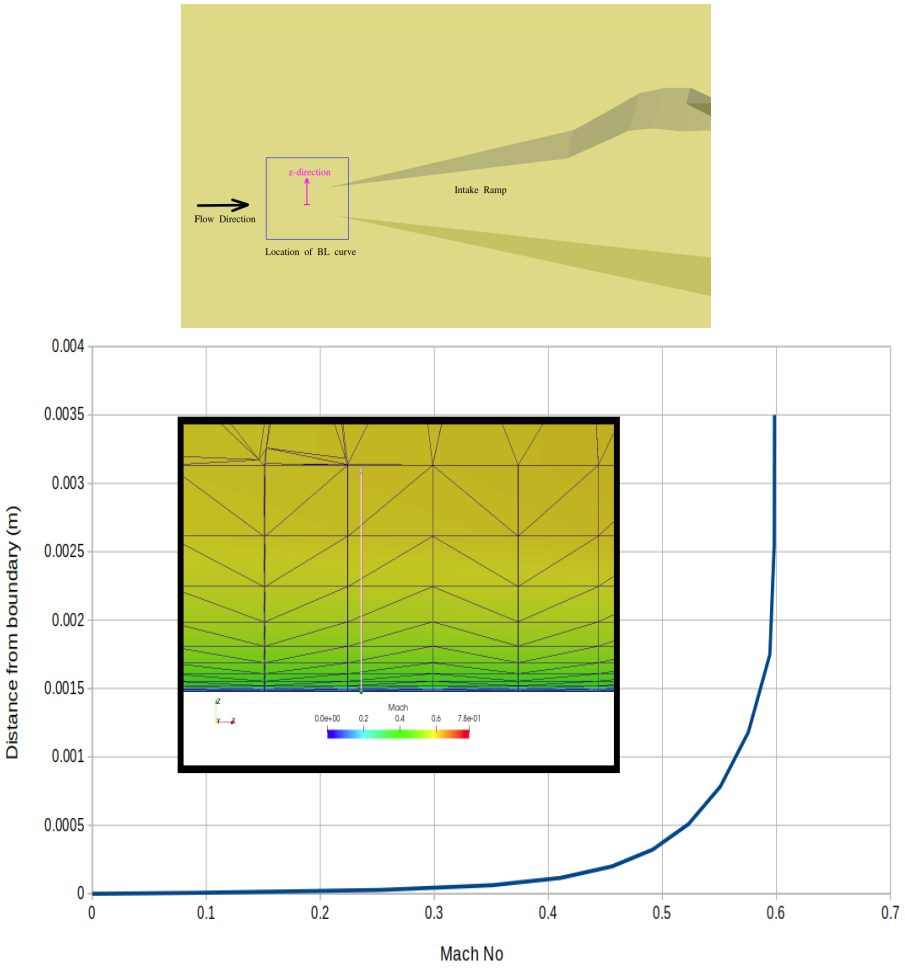

Figure 2.9: *BL profile at upstream location from onset of intake ramp.*

2.4 SU2 Solver Suite

The SU2 software is developed for solving PDE problems on unstructured meshes. The full suite is composed of several compiled C++ executable files and high-level Python scripts such as SciPY that perform a broad-spectrum of tasks requiring PDE analysis and PDE-constrained optimization. A brief discussion on modules specially SU2 _CFD is presented. Each module can be run separately however the real strength of SU2 lies in the structured execution of these modules which finally results in adjoint based shape optimization.

2.4.1 SU2- A Brief Description of Capabilities

A brief description of each of the C++ core tools is provided next. These modules are available at the time of writing, but additional modules can be added or removed from the framework with relative ease.

- 1) "SU2 _CFD" is the main **flow solver**. It gives solutions of direct, adjoint, and linearized problems for the Euler, RANS, etc. PDE‘s. Serial or parallel can both be employed by partitioning the mesh approach.
- 2) "SU2 _DEF" **mesh deformation** evaluates the geometrical deformation of surfaces within the computational mesh and the cells in the neighbourhood of the surfaces. A variety of geometric parameterization methods in vogue are also available in the suite such as Hicks Henne for 2D and FFD BOX for 3D meshes.
- 3) "SU2_DOT" **gradient projection** computes derivative of a PDE with respect to the shape design variables . "SU2 DOT" uses the surface sensitivities at each grid element such as node on the geometry provided by an adjoint solution from "SU2 _CFD" and the definition of the geometrical design variables to evaluate the derivative of a particular functional through a dot product operation. calculates the partial derivative of a functional such as drag, lift, pressure etc, for changes in the surface of interest by employing sensitivity, baseline flow results from CFD , and the definition of the geometrical

variable. This is basically a scalar product between the adjoint sensitivities and geometric sensitivities for the desired design variable parameterization.

- 4) "SU2_GEO" **geometry definition and constraints** gives the geometric properties of the surfaces such as surface area, volumes, thicknesses, etc.
- 5) "SU2_MSH" **mesh adaptation** performs grid adaptation to improve mesh quality for different requirements . In the present study gradient based adaptation refines mesh at cell locations where density gradients are large.
- 6) "SU2_SOL" **solution export** generates volume and surface solution files for desired format. The outputs as flow.vtk and surface.vtk for example can be read on PARAVIEW and processed for flow visualisation.

2.4.1.1 Boundary Conditions

The configuration file have the following available boundary conditions :

- Euler (flow tangency) and symmetry wall,
- "no-slip condition " at wall (adiabatic and isothermal),
- far-field BC ,
- near-field boundaries,
- "characteristic-based inlet boundaries" such as stagnation pressure , mass flow fixed, or supersonic Mach number BCs ,
- "characteristic-based outlet boundaries" such as back pressure defined,
- periodic boundaries, inflow boundaries for nacelle (AIP Mach number defined), and exhaust BC (nozzle stagnation temperature and pressure predefined).

The present study takes in the farfield with static pressure and freestream Mach number , no-slip for the wall boundary for body surfaces and pressure outlet with exit static pressure predefined for the engine AIP as the 3 basic boundary conditions.

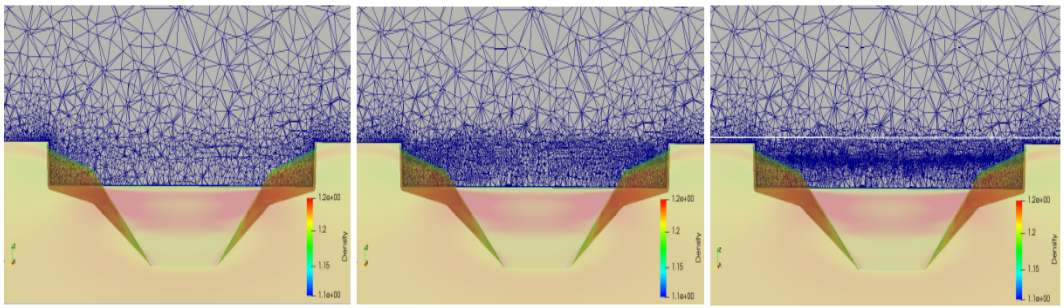

Figure 2.10: *Step-wise grid adaptation at the duct entrance section*

2.4.2 Mesh Adaptation in SU2

Mesh adaptation feature of SU2 is implemented for regions of interest. "WAKE" method is used which increases the cell density of cells surrounding the body. The number of cells to be refined can be specified such that the total increase in the cell size can be controlled. In the present study, the gradient adaptation scheme is utilized which clusters the elements with density gradient across cells greater than the threshold value of 0.5. This is observed to be near the duct entrance region surrounding the rear lip as shown in comparison to the unadapted meshes in figure 2.10.

2.5 Gradient Optimization

Aerodynamic shape optimization is currently being realized as an significant component of aerospace research and development. With the onset of improved computational resources as well as advent of new numerical tools and mathematical formulations, CFD-based optimization is the key component of future designs. The optimization process comprise of various steps. The most important are as following: the calculation of the flow field and calculation of the baseline objective function value, shape parameterization , adjoint gradients or sensitivity calculation , surface deformation based on sensitivity and hence the mesh volume deformation to adjust mesh to the newly deformed surfaces. All these steps are done in a SU2 based optimization cycle. The iteration of direct and adjoint steps are repeated till the optimum value of objective is achieved and gradient at the final design, approach negligible value. As aforementioned, the cost of solving a adjoint problem is

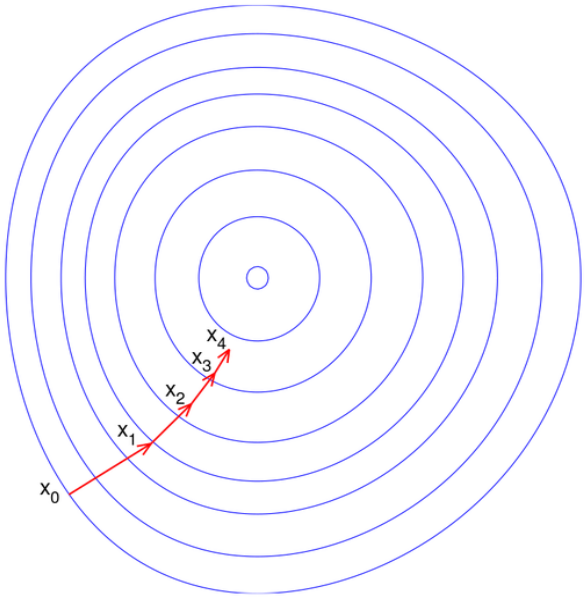

Figure 2.11: *Gradient descent - Approaching the minimum value [9].*

equivalent to the expense of solving the flow problem using CFD, accordingly the expense of calculating gradient with respect to randomly large number of parameters is same as that of two flow solutions. Subsequently , a descent method is employed to ascertain the regions and magnitude of shape deformation. A brief account of the role of gradient is mentioned. By definition , the gradient is directed towards the minimum or maximum of the function as well as ascertains the success of reaching it. The gradient can then be recalculated, and the whole process can be repeated until the design converges to an optimum solution, usually within 10 - 50 cycles. The fast calculation of the gradients makes optimization computationally feasible even for designs in three-dimensional viscous flow. Descent method, belongs to the gradient type of optimization and may converge to a local optimum and not the global optimum. For engineering applications, this does not pose a drawback, granted that the objective functions are appropriately selected representing true design needs. In gradient based methods, optimization is defined as the minimization of a chosen objective function by handling of a set of design variables in a specific framework. Nash and Sofer give the complete detail of the formulation [105]. A

general optimization framework can be formulated as:

$$\begin{aligned} Minimize \qquad & x \\ s.t \qquad for \qquad & J(x) \\ where: \qquad & g(x) > 0, \\ and \qquad & H(x) = 0 \end{aligned}$$

Where J is the objective function, x is the set of design variables and g and H are the inequality and equality constraints respectively. At the optimum point the inequality constraints can be neglected and hence the optimization problem is only constraint by equality constraints, Lagrange multipliers are employed to make the problem a closed set problem such that the total number of variables is the sum of original number of variables and the equality constraints. The gradients of the objective function with respect to the design variables are used to improve the design variables to methodically decrease (or increase) the cost function to arrive at a local minimum (or maximum). Initially it is a problem with n unknowns, and (n + m) equations. The additional unknowns for system closure is provided by Lagrange multipliers. Lagrange provided a way to address this problem. The manipulation is as follows: by subtracting the total derivative of the constraint from the objective and introducing the multipliers using equality constraint results in the Lagrange equation satisfying the KKT condition [105].

$$\begin{aligned} L &= J(x) - \lambda H(x) \\ \nabla L &= \nabla[J(x) - \lambda H(x)]dx = 0 \end{aligned}$$

Surface geometry optimization modifies shapes based on the gradient of objective function with respect to the shape change from a baseline shape. This makes selection of base line geometry or shape of greater importance than one would envisage. Incorrect selection of a certain starting base shape may only result in the localized optimum solution, preventing the derivation of a global optimum shape that would provide superior performance.

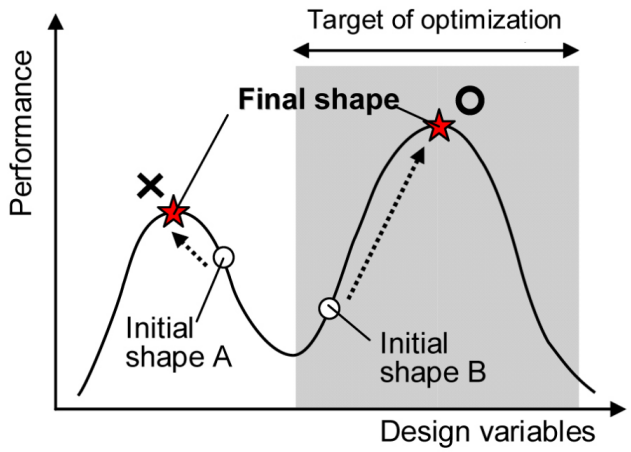

Figure 2.12: *Initial shape dependency on search direction [10].*

2.6 Design Space Specification

Hence its now relevant to discuss design space selection guidelines. The design variables chosen for optimization necessitate a specific limit on the ranges of space in which the optimal is found. Simulation or CFD based optimization include both gradient based and gradient free methods such as genetic algorithms GA as mentioned earlier.

Gradient based methods are considered for local optimization and the method relies upon steepest descent and sequential quadratic programming (SQP). The baseline case can be taken as the initial design. Lately adjoint methods have gained considerable grounds due to a higher degree of variability to account for a larger design space. In adjoint based gradient techniques, the search is within the provided constraints of flow functions and allowable space restrictions but is governed by the gradient . In this thesis, it is acknowledged that the baseline geometry for the case is obtained from already published designs such as NACA intake and trapezoidal intake. The placement of NACA intake on the flat plate is an innovation. This adventure was motivated by the necessity of measuring the C_L/C_D , which when measured for a flat base plate without thickness is a meaningless parameter. Similarly in the case of trapezoidal intake in slender body, the exact and complete measurement of the actual geometry are unavailable therefore the author admits the aberrations in the geometry which can be detrimental to flow results and parameters obtained to be off from published results. Angles of attack is kept zero for all configurations.

With regards to freestream flow, the Mach number for optimization for the NACA inlet on flat plate is taken at 0.6 where the maximum lift coefficient is obtained. In the case of trapezoidal inlet on slender body the same Mach number of 0.7 is taken which is same as reference study. Finally in the case of circular intake, the shape of entrance is changed while all the rest of the configuration and parameters is similar to the trapezoidal case. The circular entrance intake configuration is for the sake of optimization validation.

2.7 Optimization Algorithm in SU2

After the design space is designated and the desired functional are formulated the next step is to calculate the gradients of the functional . As described earlier, there are two methods to achieve this i.e. direct or inverse. The adjoint method is the inverse method in which gradient of objective functions with respect to design variable is calculated, which is present study, the FFD box control points. The result obtained from adjoint evaluation is the sensitivity analysis. The adjoint sensitivity dictate the surface deformation of the geometry critical to the objective function optimization. In following sections the very mathematical equations will be derived in this regards and it is important to mention both flow solutions and adjoint are iteratively solved. All operations are done in cycle of primary flow solution followed by gradient calculation and finally shape deformation. The calculation of the objective is in tandem with the initial flow solver process. Other additional steps auxiliary to the loop include volume deformation which is inherently iterative based upon spring analogy for mesh adjusting to the newly deformed surface geometry. The procedure is followed during SU2-based adjoint optimization execution. In SU2 the shape design cycle is governed by the SLSQP Sequential Least Squares Programming optimizer available in the SciPy library [69]. SciPy is an open ware tool written in Python which supports scientific and numerical applications. It can find roots, least square , curve fitting etc. It can solve a number numerical problems including gradient optimization required for the present study using "SciPy.optimize". SciPy optimize gives functions to minimize (or maximize) objectives, which can be both constrained or unconstrained [106] . The basic theory is mentioned in the upcoming sections related to adjoint

equations.

2.8 Governing Fluid Flow Equations in SU2

The governing equations for the present problem are the three-dimensional Navier-Stokes equations compactly given as follows:

$$\frac{\partial \rho}{\partial t} + \overrightarrow{\nabla} \cdot (\rho \overrightarrow{v}) = 0 \tag{2.1}$$

$$\frac{\partial (\rho \overrightarrow{v})}{\partial t} + \overrightarrow{\nabla} \cdot [\overline{\rho v \otimes v}] = -\overrightarrow{\nabla p} + \overrightarrow{\nabla} \cdot \overline{\overline{\tau}} + \rho \overrightarrow{f} \tag{2.2}$$

$$\frac{\partial (\rho E)}{\partial t} + \overrightarrow{\nabla} \cdot ((\rho E + p) \overrightarrow{v}) = \overrightarrow{\nabla} \cdot (\overline{\overline{\tau}} \cdot \overrightarrow{v}) + \rho \overrightarrow{f} \overrightarrow{v} + \overrightarrow{\nabla} \cdot (\overrightarrow{q}) \tag{2.3}$$

Given that the flux vector U :

$$U = \begin{Bmatrix} \rho \\ \rho \overrightarrow{v} \\ \rho E \end{Bmatrix}$$

SU2 can solve PDEs that are governing a physical system of a fluid mechanics problem and are written in the following expression:

$$\frac{dU}{dt} + \nabla . F^c - \nabla . \mu_1 F^{\nu 1 k} - \nabla . \mu_2 F^{\nu 2 k} = Q \tag{2.4}$$

the convective and viscous fluxes and heat transfer and source terms are:

$$F^c = \begin{bmatrix} \rho v \\ \rho v v + \overline{\overline{I}} p \\ \rho E v + p v \end{bmatrix} ; F^{\nu 1} = \begin{bmatrix} - \\ \overline{\overline{\tau}} \\ \overline{\overline{\tau}} . v \end{bmatrix} ; F^{\nu 2} = \begin{bmatrix} - \\ - \\ C_p \nabla T \end{bmatrix} ; Q = \begin{bmatrix} q_\rho \\ q_{\rho v} \\ q_{\rho E} \end{bmatrix}$$

The governing equation is now reorganized to define the residual, which will be driven towards zero by iterative numerical methods. The gradient of which is the function of the residual that will converge to zero and provide the necessary constraint equations.

2.8.1 Menter‘s Shear Stress Transport SST Model

A two equation turbulence model was formulated by Menter which has proved to be quite an effective and robust eddy-viscosity solving tool for most aerodynamic applications [107]. The two equations have blending functions which combine the powerful inner boundary layer resolution from K-omega and effective shear flow capturing by K-epsilon.

$$\mu_{turb} = \frac{\rho a_1 k}{max(a_1\omega, Sf_2)} \tag{2.5}$$

$$S = \sqrt{2S_{ij}S_{ij}} \quad \bar{F^c} = \rho k\bar{v} \quad \bar{F^\nu} = -(\mu_{dyn}+\sigma_k\mu_{turb})\nabla k, \quad Q = P-\beta^*\rho\omega k \tag{2.6}$$

$$\bar{F^c} = \rho\omega\bar{u} \quad \bar{F^\nu} = -(\mu_{dyn}+\sigma_k\mu_{turb})\nabla\omega, \quad Q = \frac{\gamma}{\nu_t}-\beta^*\rho\omega^2+(1-f_1)\frac{\rho\sigma\omega^2}{\omega}\nabla k\nabla\omega; \tag{2.7}$$

The blending functions denoted by f1 and f2 are devised such that they tend to zero at their respective limits. Blending functions are the very tools that transform the K-ω formulation in the inner boundary layer portions consisting of near wall and logarithmic regions into K- ϵ outside the boundary layer to resolve wake and free shear. SST has been checked for its efficacy through rigorous validations with experimental results and is excellent in prediction of pressure induced boundary layer separation.

2.8.2 SU2 Fluid Flow Solver Settings

The present study is for 3D aerodynamic objects in high subsonic and transonic flow regimes. The solver settings with RANS are done by taking into account compressibility and viscous flow considerations. SST model for turbulence modeling is employed while flux splitting schemes such as 2nd order HLLC and ROE for convective flow upwind resolution are used.

2.9 Formulation for Adjoint Based Optimization in SU2

The adjoint method as already delineated in preceding sections, follow the process of inverse design by evaluating the sought after change in the objective function in lieu of directly finding the value of/or change in objective function with respect to any change of design variables. The numerical determination by one matrix manipulation provides complete gradient of the objective in this technique, notwithstanding the number of variables. The full analysis would require a direct flow computation using CFD and succeeding by adjoint step for the given objective. Sensitivity analysis is the crucial manoeuvre in which the gradients are determined for which, as mentioned earlier, the Lagrange multipliers are employed to transform constrained type of optimization problem into unconstrained optimization which is thus mathematically less involved. This is essentially well-suited to aerodynamic design optimization whereby the population of mesh nodes or geometric points comprising the design parameters is numerous compared to that of aerodynamic constraints. Hence the derivatives with respect to all design variables for each objective function or aerodynamic constraint can be obtained with a computational sort roughly equivalent to that for a single solution of the flow equations. Adjoint methods can generally be divided into discrete and continuous adjoint methods. In the discrete adjoint approach, the augmented cost function is discretized before variations are taken. For the continuous adjoint formulation, the process is reversed: variations are performed first, followed by the discretization. It should be appreciated that the differentiation and discretization do not abide by commutation generally. Hence, derivatives obtained by using the two approaches may not be identical and would differ according to the level of truncation error. The formulation of adjoint based aerodynamic optimization is discussed in several studies and recently started to be implemented in different computational platforms [55] , [108], [109]. A form of governing equation can be written in the following semi-discrete form:

$$R(U) = 0 \tag{2.8}$$

The flow variable U being a function of the mesh coordinates:

$$R\left(U(X), X\right) = 0 \tag{2.9}$$

Therefore as derived in the earlier section the residual is obtained:

$$R\left(U,X\right)=\frac{dU}{dt}+\nabla.F^{c}-\nabla.\mu F^{\nu k}-Q=0 \tag{2.10}$$

Here X is the mesh coordinates and $\mathbf{U}$ is the vector of the fluid system variables and $\mathbf{R}$ is the residual which diminishes as the solution converges. This residual tends towards 0 and will be effectively the equality constraint for the KKT condition application. It is later combined with the objective condition.

$$R\left(U,X(x)\right)=0 \tag{2.11}$$

which can be differentiated w.r.t design variable to give:

$$\frac{dR}{dx}=\frac{\partial J}{\partial U}\frac{dU}{dx}+\frac{\partial J}{\partial X}\frac{dX}{dx}=0 \tag{2.12}$$

The objective function J depends on the mesh points and flow variables which depend upon x , the space coordinates,

$$J\left(U,X(x)\right) \tag{2.13}$$

Differentiating with respect to design variable gives another differential equation where multiplier functions are specified.

$$\frac{dJ}{dx}=\frac{\partial J}{\partial U}\frac{dU}{dx}+\frac{\partial J}{\partial X}\frac{dX}{dx} \tag{2.14}$$

Now equation 2.12 and equation 2.14 can be combined by choosing a vector such that:

$$\frac{dJ}{dx}=\frac{\partial J}{\partial U}\frac{dU}{dx}+\frac{\partial J}{\partial X}\frac{dX}{dx}+\Psi^{T}\left(\frac{\partial R}{\partial U}\frac{dU}{dx}+\frac{\partial R}{\partial X}\frac{dX}{dx}\right) \tag{2.15}$$

Rearranging:

$$\frac{dJ}{dx}=\frac{\partial J}{\partial X}\frac{dX}{dx}+\Psi^{T}\frac{\partial R}{\partial X}\frac{dX}{dx}+\frac{dU}{dx}\left(\frac{\partial J}{\partial U}+\Psi^{T}\frac{\partial R}{\partial U}\right) \tag{2.16}$$

Now the term in bracket can be put to zero for a certain value of the Ψ^{T} term:

$$\left(\frac{\partial J}{\partial U}+\Psi^{T}\frac{\partial R}{\partial U}\right)=0 \tag{2.17}$$

This is fundamentally the Adjoint equation with Ψ^T term called the Adjoint solution. What is left of the equation 2.16 is

$$\frac{dJ}{dx} = \frac{\partial J}{\partial X}\frac{dX}{dx} + \Psi^T \frac{\partial R}{\partial X}\frac{dX}{dx} \tag{2.18}$$

Multiply whole eq by dx/dX:

$$\frac{dJ}{dX} = \frac{\partial J}{\partial X} + \Psi^T \frac{\partial R}{\partial X} \tag{2.19}$$

The adjoint volumetric sensitivity can be obtained from equation 2.19. Hence it is observed that the sensitivity analysis can be done by only using the objective function. To determine surface sensitivity consider equation 2.14; again the derivative of objective function with respect to the geometric coordinates by first dividing by dx/dX is given by the volumetric sensitivity:

$$\frac{dJ}{dX} = \frac{\partial J}{\partial X} + \frac{\partial J}{\partial U}\frac{dU}{dX} \tag{2.20}$$

The change in performance dJ with respect to change in surface coordinates Xs can be given as:

$$\frac{dJ}{dx} = \frac{dJ}{dX}\frac{dX}{dX_s}\frac{dX_s}{dx} \tag{2.21}$$

Therefore a combination of the volumetric sensitivity with inverse of surface moving speed using the chain rule gives the surface sensitivity:

$$\phi = \frac{dJ}{dX_S} = \frac{dJ}{dX}\frac{dX}{dX_S} \tag{2.22}$$

As mentioned earlier, the shape optimization is based upon adjoint sensitivity gradient and shape parameterization [60].

Sequential quadratic programming (SQP) is an iterative technique for solving nonlinear optimization which are usually constrained. The condition which is required to be satisfied is for the cost function to be differentiable two times in continuity. SQP works out a optimization sub-problems arranged in order , with every sub-problem optimizing a quadratic representation of the constrained objective function . For problems with just equality constraints it is similar to solving Newton's method to the gradient of function equal to zero i.e. the KKT

condition [110]. SciPY utilizes SLSQP which is also solving the same quadratic problem but in a rather sophisticated fashion where by applying the square-root-free Cholesky decomposition by the optimizer first which factorizes Lagrange Hessian and then works out the linearized SQP [111] . The benefit of SLSQP over sımpler version as SQP is the ability to solve large size problems such as adjoint gradient in aerodynamics optimization.

2.10 Objective Functions and Constraints in SU2

SU2 has a number of objective functions which can be used as constraint as well. The list of all these functions can be found in the `"config_template.cfg"` file which can be used in a variety of formats inside the "OPTIMAL SHAPE DESIGN DEFINITION". The most common and easy to apply is the single objective without constrain, in which only a single objective function such as `"OPT_OBJECTIVE= SURFACE_ TOTAL_ PRESSURE*1e-07"` as in the present case can be written. Here 1e-07 is the weight multiplied with the objective and is also called the "SCALING FACTOR". The ease of using a single objective lies in the match of number of surfaces in the `"MARKER_MONITORING"`. If a single objective function is used there can be as many markers surfaces in the list for monitoring but for multi objectives, there is a limit to the number of surfaces which must match the number of objective functions. In the present study in configuration II, III and IV the multi-objective format is employed with pressure on AIP and lift as the main functions while drag is used as penalty function which acts basically as constraint. In any case since the number of objective functions is three therefore the number of monitor surfaces is also three and given as `"MARKER_MONITORING" = (outlet, intake, body )` . It should be mentioned here that the deformation surfaces are not required to be explicitly mentioned in the monitors and are separately defined in the design variable settings.

2.11 Functional for Objective Functions in SU2

In order to develop flow based adjoint equations it is imperative to get the change in the respective functional. Therefore the given functional in the form of expanded equation of change is presented in here which are originally derived and implemented for SU2 by Kline and complete details of the same can be found in thesis [68]. There are basically two types of functionals: force based i.e. coefficients of lift and drag, also called projected force functional, which require integration of momentum on the wall surface and the other being the integrals of flow parameters at a boundary of the flow such as total pressure at defined locations of interest, in present case the AIP.

2.11.1 Total Pressure Functional

The objective function is defined as the surface averaged total pressure and the final form will be in terms of the flow variables :

$$J = \int_{\Gamma} P_t \, dS \tag{2.23}$$

$$\delta J = \int_S g^{\frac{1}{\gamma-1}} \left(\frac{|\overline{v}|^2}{2} \delta\rho + \rho\overline{v}.\delta\overline{v} + \left(g - \frac{|\overline{v}|^2 \rho}{2P} \right) \delta P \right) ds \tag{2.24}$$

2.11.2 Aerodynamic Force Functional

The objective function is defined as the surface force in the direction of the projection with respect to the reference frame, and again the final form will be in terms of the flow variables as well the direction vector :

$$J = \overline{d}.\overline{f} \tag{2.25}$$

$$\delta J = \int_S \left(\overline{\overline{I}} P - \overline{\overline{\sigma}} \right) .\overline{n} ds + \int_S \left(\overline{d}.\overline{q} + \nabla\overline{d} \colon \left(\overline{\overline{I}} P - \overline{\overline{\sigma}} \right) - \left(\overline{\overline{I}} P - \overline{\overline{\sigma}} \right) .\overline{n}.\partial_n \overline{d} \right) \delta S ds \tag{2.26}$$

2.12 Adjoint Based Shape Optimization in SU2

At this juncture a brief account is given for the optimization problem and integration with flow solver equations in SU2. The components of the design vector can for example be chosen as the control points of the free form deformation (FFD) method for 3D problems in other words the surface points of interest is the design vector. According to a movement of the surface based on the current values of the design variables, a mesh deformation routine via Linear Elasticity method using spring analogy solves iteratively to generate mesh for next design cycle let it be X. The flow solver then evaluates the flow variable vector U from which objective function J is calculated. Gradient of objective function is preceded by shape parameterization. The surfaces of interest where the sensitivities are required are parameterized by FFD box and geometric surfaces transfer control to the lattice points on the FFD box by point inversion. The **"shape optimization.py"** script organizes the relevant

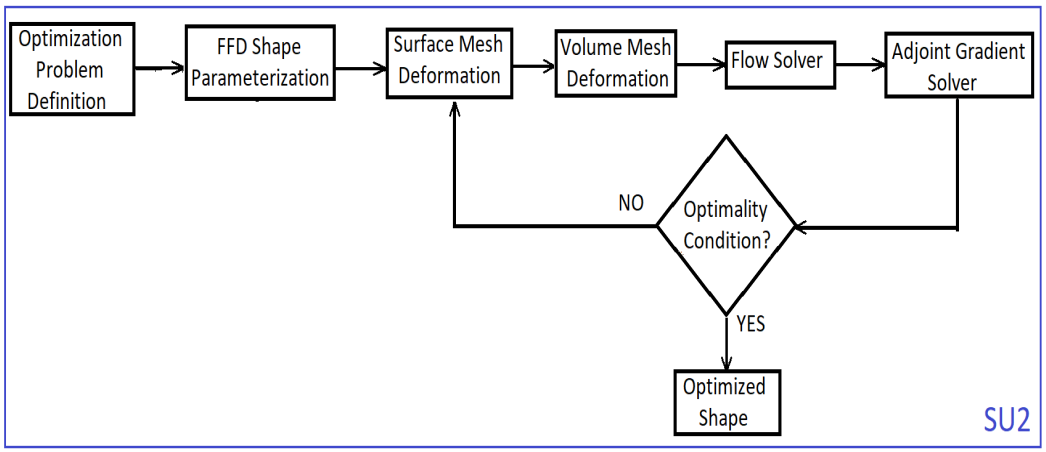

Figure 2.13: *Shape optimisation process cycle in SU2*

.

modules in SU2 modules to undertake the shape optimization process. The choices for the objective function, design variables, and additional module settings that define the optimization problem are controlled through options in the configuration file.

2.12.1 Available Modes of Shape Optimization

SU2 enables different modes of optimization. The following tutorial examples are available in the Github to learn and implement shape optimization process in a step by step fashion [112] :

- Unconstrained single objective shape design -transonic inviscid 2D airfoil
- Constrained single objective shape design - transonic turbulent 2D airfoil
- Constrained single objective shape design - transonic in-viscid 3D wing
- Constrained multi-Objective shape design- inviscid Supersonic 2D Ramp

In the present study, the solutions are solved for 3D shape using RANS with SST model. The tutorials for SU2 do not include such case for optimization however this task will be undertaken in the present study for all the cases to shape optimize a 3D shape at given subsonic/transonic viscous flow conditions with geometric and functional constraints.

2.13 Shape Parameterization in SU2

In aerodynamic shape optimization, a shape is either specified by parameterization itself or manipulated by deformation based upon parameterization. This implies that depending on the given parameters, a geometry is constructed by set of design variables. Additionally, the achieved geometry possess characteristics of interest such as drag, lift etc. Hence, aerodynamic shape optimization improves the design vector and the shape for identified aerodynamic objectives. The surfaces are deformed in a calculated fashion. The delineated deformation is achieved by using parameterization tools. The available methods in SU2 for this purpose are enlisted for 2D and 3D types of deformation in the configuration file under section "OPTIMAL SHAPE DESIGN DEFINITION ". In each design a fraction of deformation is done and the objective function evaluated . Hence the most commonly used deformation techniques are : HICKS HENNE funtion for 2D and FFD Control point for 3D [113].

Basic considerations for shape parameterization as mentioned by Kwang [114] are as follows:

- Smoothness: Surface uniformity and smoothness during deformation
- Local control: Authority on the surface points for local control
- Analytical sensitivity: Degree of viability for estimating sensitivity
- Grid deformation: Deformation of volume grid following parameterization
- Set up time: Speed of setting up the parameterization application
- Existing grid: Re-usability of grid
- CAD: Transition between different modules such as CAD to CFD

2.13.1 Free Form Deformation Box Method in SU2

In the present study , shape parameterization is carried out by FFD Box. FFD box is a small structured mesh block with (i,j,k) indices for the control points, and the number of control points in each direction is the specified polynomial degree (plus one +1). FFD can treat surfaces of any formulation or degree and it is independent from the domain or the mesh which is used for its discretization. It features a good compromise between generality and simplicity. A distinguishing aspect of this method is that, by deforming the whole volume around (or inside) the object, the computational grids are also being automatically deformed with the object, which is a valuable characteristic for automated design optimization procedures. Lattice defined by the Bernstein polynomials ensure that by just moving one control point in one direction will allow the smooth deformation of all the surface. However, the linked lattice points are altered in position by restrictions imposed in the definition of deformation settings hence geometric variation occurs in a defined and co-related manner. The Bernstein polynomials reduces the number of shape parameters. This gives the advantage of defining a local FFD box so as to deform just a specific surface in the whole body only. These lattice points are governed by restrictions imposed by deformation rule hence geometric variation occurs in a defined and co-related

manner. Employing FFD box ascertain high calibre of modifications , however it will be difficult to strictly abide by geometrical constraints i.e. shape topology.

$$P_{l,m,n}\mu_{l,m,n} = P^0_{l,m,n} + \mu_{l,m,n}$$

The parametric domain map is constructed for the FFD control points as :

$$(\Psi(x);\mu) = \Psi^{-1}\left[\sum_{i=0}^{L}\sum_{i=0}^{M}\sum_{i=0}^{N} b^{L,M,N}_{l,m,n} P_{l,m,n}(\mu_{l,m,n})\right]$$

Control points on the FFD box hold a certain coordinate on the volume mesh and act as anchors for surface of design variable as shown in figure 2.14. Here $b^{L,M,N}_{l,m,n}$ is the Bernstein Tensor , where $P_{l,m,n}$ are the FFD Box control points for the given indices $\mu_{l,m,n}$ (and corresponding movement directions l, m ,n respectively) defined on the unit square with local variables (s, t, p) , and the function :

$$\Psi : (x_1, x_2, x_3) \rightarrow (s, t, p)$$

This is also called "Point inversion method". Accordingly, as mentioned in SU2 related documentation and experiences during the present study suggest that "Point-inversion" is not a robust method and several iterations of "FFD setting" are done before a stable configuration is achieved for a particular optimization problem [115]. The grid deformation solver is an iterative process analogous to the CFD flow solver. The error bounds limit the range of shape deformation for a certain cycle. Therefore when bounds are increased the deformation will be more pronounced and correspond to a wider line search allowing for a higher optimal value of the objective function. FFD box surface deformation technique is thus an excellent tool for an optimization problem, which is inherently an iterative process .

2.13.2 Setting up a Free Form Deformation Box

The mesh file exported from GMSH will be redefined with an overlay mesh block called the FFD or free form deformation box. The FFD box is defined in the configuration file of SU2. The control points are written with reference to the surface. As the current implementation requires each FFD box to be a 6 faced box with 4 sided or quadrilateral faces on each side. The 8 corner points of the box can

be prescribed along with the degree of polynomial required to denote each axes for creating full control points lattice structure . The FFD box is analogous to a structure meshed volume just large enough to fit in the surfaces of interest with (i,j,k) indices for the control points.

As aforementioned, the requirement is for the FFD box to be a hexahedron (6 faces, 12 edges, 8 vertices), therefore the coordinates of the 8 corners are stated and the polynomial which is desired for direction and degree of allowable movement to account for each coordinate direction (x,y,z) so as to create the full lattice of control points as shown in figure 2.14. In the FFD DEFINITION option, a specific name is given to the box, and then list out the x, y, and z coordinates of each corner point. The order is important, and you can use the example given to match the convention. The degree is then specified in the FFD DEGREE option. A view of the box with the control points numbered is shown in figure 2.14. Note that the numbering in the figure is 1-based just for visualization, but within SU2, the control points have 0-based indexing. For example, the (1,1,1) control point in the figure is control point (0,0,0) within SU2. This is critical for specifying the design variables in the configuration file. The FFD set up allows for ensuring surface smoothness within SU2 setup by selecting control of Bezier curve solver by choosing 1st or 2nd derivative of the surface with the FFD CONTINUITY option. The shape deformation in which the FFD box uses the control points on its surface to change position of the surface mesh points the new surface emerges which may have undesired crevices and non-smooth edges. This newly emerged surface is based upon the adjoint sensitivity

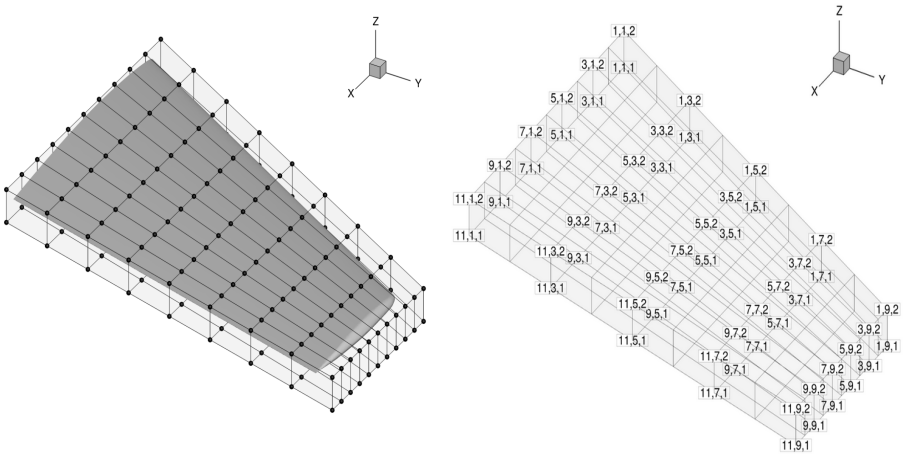

Figure 2.14: *Left: FFD box enclosing wing geometry. Right: FFD box with control point numbered*

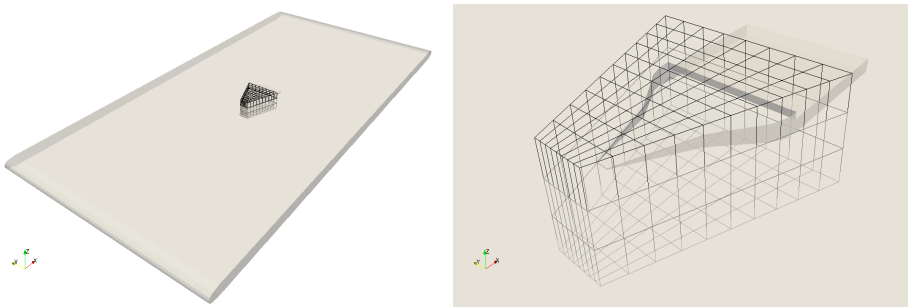

Figure 2.15: *FFD box of [11,9,4] configuration for NACA intake on flat plate.*

and geometric bounds, however solver is nonetheless required to run in 2 lags, the linear and nonlinear mode to ensure the surface smoothness.

2.13.3 Volume Mesh Deformation by Spring Analogy

In SU2 the volume mesh is deformed using elastic deformation theory where internal mesh is analogous to spring lattice as proposed by Batina [116] [71] .

The modifications to the shape of the boundary are transferred to the volume mesh using the spring method. This approach has been found to be adequate for the computations performed in this study. The spring method can be mathematically conceptualized as solving the following equation:

$$\frac{\partial \Delta x_i}{\partial t} = \sum_{j=1}^{N} K_{ij}(\Delta x_i - \Delta x_j) \tag{2.27}$$

where Kij is the stiffness of the edge connecting node i to node j and its value is inversely proportional to the length of this edge; Δx_i is the displacement of node i; and Δx_j is the displacement of node j, the opposite end of the edge. The position of static equilibrium of the mesh is computed using a Jacobian iteration with known initial values for the surface displacements [74] .

2.14 Adjoint Solver Settings in SU2

The adjoint solver, gives the sensitivity, where by the shape optimization solves for the gradient of the objective function for variation in shape of the design variables

which in the present case consist of only the intake surfaces. As mentioned in earlier sections, the cost of this solution is almost same as that of the direct CFD solution. The adjoint solver settings include similar settings as those of the direct solution such as suitable convective numerical methods which can be chosen from JST, LAX-FRIEDRICH or ROE methods. The objective functions for the present cases are used as single or multiple format. In both formats proper weights can be used for achieving desired order of magnitude of the adjoint hence expediting the optimization cycles.

2.15 Specifying Optimization Surfaces

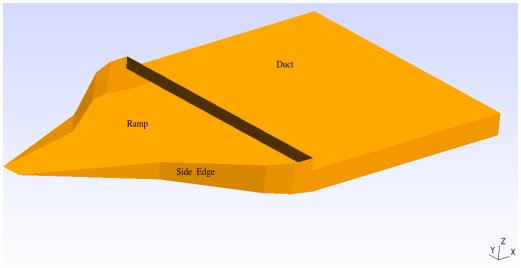

Figure 2.16: *The intake surfaces are defined as design variables.*

The design variable settings for shape deformation are given as the MARKER ID of the surfaces and the deformation variables as direction index for each control point on the FFD box MARKER in the present case which is named "WING". The details are present in the configuration file in Appendix. Inclusion of the body surface in the neighbourhood of the intake flush region is of critical importance with respect to design space. A fully submerged intake geometry demands a perfectly rigid body surface with respect to any deformation. In initial cases in this study this constraint was implemented. The sensitivity map for the objective function revealed available design space therefore the constraint was relaxed in later cases to include some portion of the body surface as well and improved values of optimized functions were achieved. However as a result of this geometric relaxation , the intake obtained , in the strict sense, was not fully submerged as will be observed in the later discussions.

2.16 Code Execution

After the configuration file is defined for every setting then the shape optimization script is executed by the command: "shape optimization.py -g CONTINUOUS ADJOINT -f subsonicintake.cfg ". The number of cores are also additionally given to increase the computational resources. The additional packages required to run the script are Python, NumPy, and SciPy . As the tolerances prescribed in the SciPy optimizer are achieved the design cycle stops. An already converged solution for both CFD and adjoint sensitivity can be taken for a given baseline mesh as the initial case for which the restart option must be given affirmative in the configuration file.

2.17 Post-Processing with ParaView

The PARAView free-ware package is employed for the illustration of results by defining the name of the tool in the "write solution" in configuration file. The results include force monitored on surfaces such as body drag, outlet average flow parameters and .vtk files of the surface and flow solutions.

2.17.1 DC(90) calculation

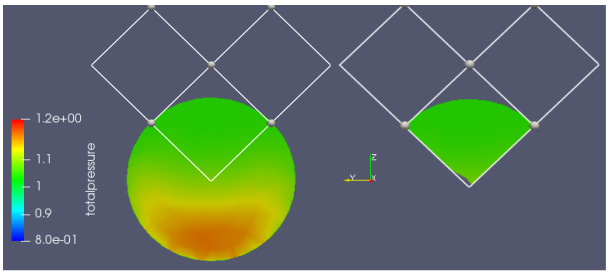

Figure 2.17: *DC(90) calculation using sector cut in PARAView.*

Most of different parameters are calculated by SU2 and can be obtained from history file. However DC(90) is not available in SU2 output files therefore PARAView is employed. The sector is generated by slice and clip command and total pressure is calculated by integral calculator. The worst sector is checked through continuous cuts although it is observed that the worst total pressure is on the top sector. The value DC(90) is then estimated using the formula in equation 1.1.

CHAPTER 3

VALIDATION STUDY

The present study aims to shape optimize submerged intake. Three different geometries are considered namely: NACA intake, trapezoidal entrance intake and circular entrance intake. The first and second intake are already present in literature. These reference studies are therefore validated by using the tools mentioned in the previous section and CFD results are compared with experimental and numerical results before proceeding to optimization. Mesh independence is also established simultaneously and the mesh with the validated CFD solution is henceforth termed respectively as the baseline mesh and solution for the design optimization iterations.

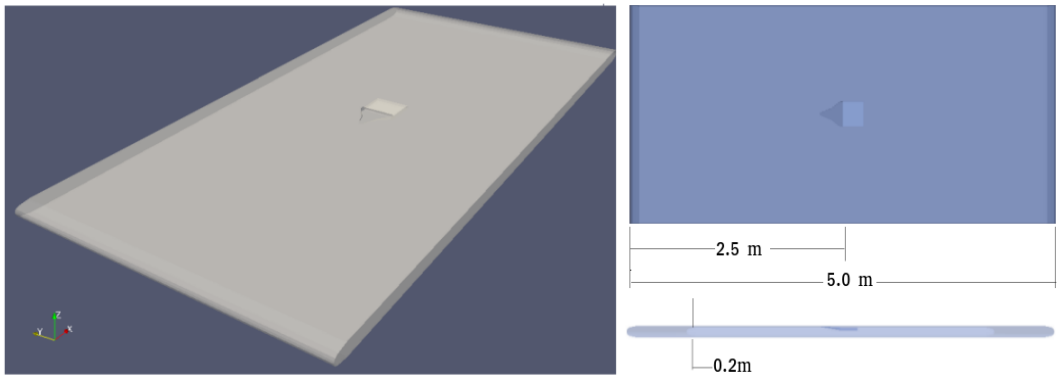

Figure 3.1: *Geometry of flat plate with NACA intake mounted on upper surface*

3.1 Case I : NACA Intake on Flat Plate

NACA generic intake on flat plate is taken as initial case for the present study. The intake performance is evaluated using qualitative CFD results and Cp distribution on ramp centre-line is compared with experimental results as given in Pignier [5].

3.1.1 Geometry Definition and Mesh Generation

The NACA type submerged intake is a non-protruding geometry which acts as a complex cavity. The value C_L/C_D from a intake at zero angle of attack can be unrealistic. In order to give a geometrically tangible body , the intake is centre mounted on a flat plate of plan-form area of 5mx2.5m and thickness of 0.2 m that gives a thickness to width ratio of 0.08 hence it can be safely considered as a flat plate where the total depth of the intake when submerged from the top surface of the plate is 0.07 m. The solid modeling and mesh generation process is illustrated in previous chapter. The Y+ distribution resulting from flow solved over the surface is shown in figure 3.2. The angle of attack of the plate is zero in a free stream subsonic flow. Reference length is flat plate length = 5 m and Reynolds no = 66.9E6 at ambient conditions (T=288K P= 1.01bars). Outlet pressure BC is given in table 3.1.

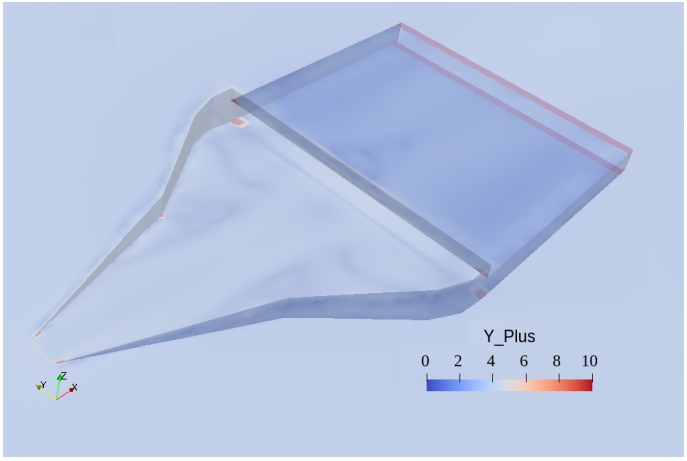

Figure 3.2: *Y+ distribution on the NACA intake.*

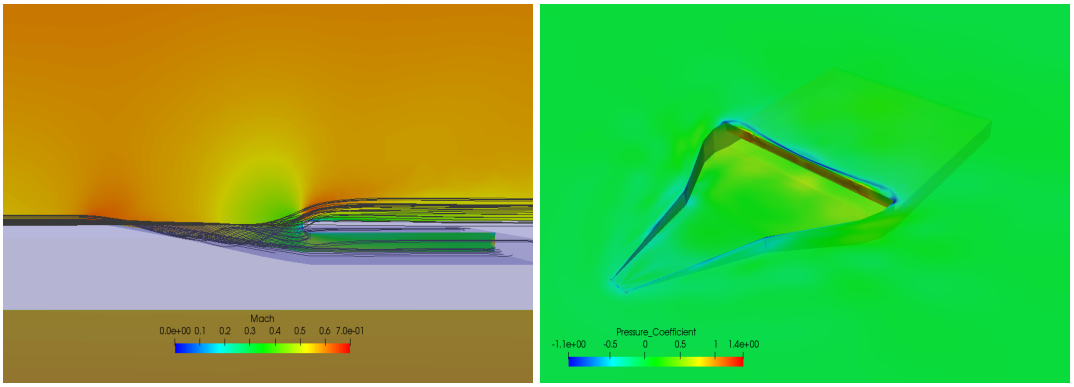

Figure 3.3: *Left:Mach filled centre plane and grey streamlines. Right: Cp distribution.*

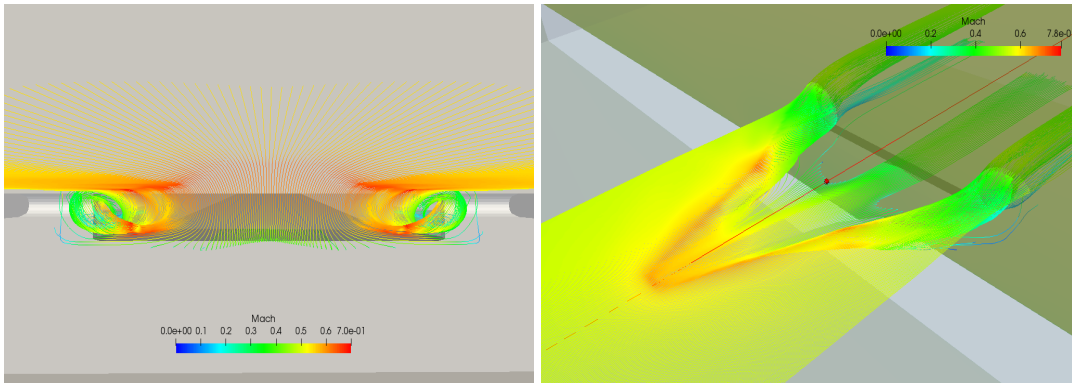

Figure 3.4: *Stream lines showing vortex pair emanating from side edges*

Table 3.1: *Outlet Pressure BC vs intake velocity ratio* V_1/V_0.

p_2/P_0	V_1/V_0
0.80	1.0
0.85	0.8
0.90	0.6
0.95	0.4

3.1.2 Flow Solution and Mesh Independence

The flow is solved for the given geometry and mesh using the direct CFD solver in SU2. The flowfield around the NACA intake is at freestream Mach number 0.6. The results are illustrated in figure 3.2 - 3.4. Vortex pair is observed to emanate from the the side edges. This vortex pair entrain the flow into the intake cavity and thereafter eases the flow into the duct. The validation of present CFD study is done. Mach contours and streamlines on the centre plane at different velocity ratios are illustrated in figure 3.5. As clearly observed, the bulk of the flow branches out into the external flow at V_1/V_0=0.4 while for V_1/V_0=1.0 almost all of the flow entering the intake cavity entrains into the duct of the intake. The same same phenomena with very small difference is seen in both the reference images at the top as well as the present benchmark study. It should be appreciated at this juncture that, the CFD results obtained also verify the velocity ratios as shown by the color-map of the streamlines in the corresponding figures. The qualitative comparison reveals similar behavior of flow. The pressure coefficient along the ramp centre-line is shown in figure 3.6.

Experimental and numerical results from reference study are plotted viz-a-viz present study. The results indicate similarity in trend as well as agreement of value of Cp at different stations along the centre-line. The solution adapted mesh give better results to initial mesh with respect to favorable comparison with the reference results.The ram recovery factor at the AIP for free stream Mach number = 0.2 is evaluated at different velocity ratios. The results are compared with experimental and CFD results from Mossman [3] and Pignier [5] respectively. The maximum recovery is obtained at velocity ratio in the range of 0.4-0.6 for all three studies at around 0.9 as shown in figure 3.7.

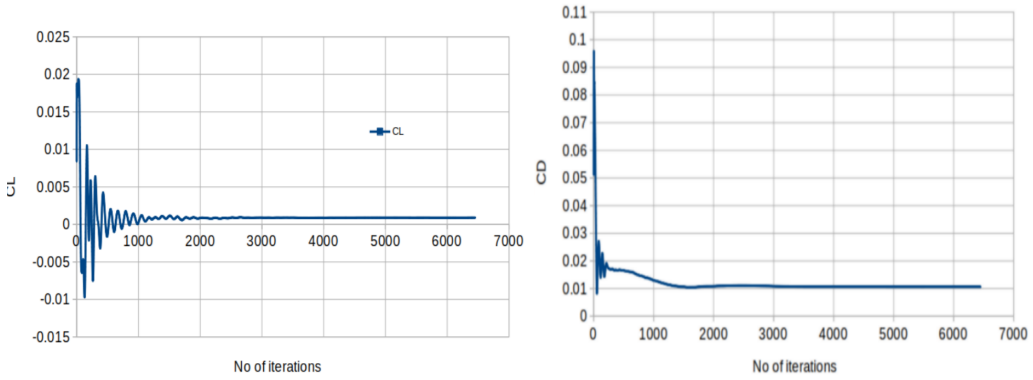

Figure 3.5: *Convergence history of NACA intake on flat plate at Mach number 0.6.*

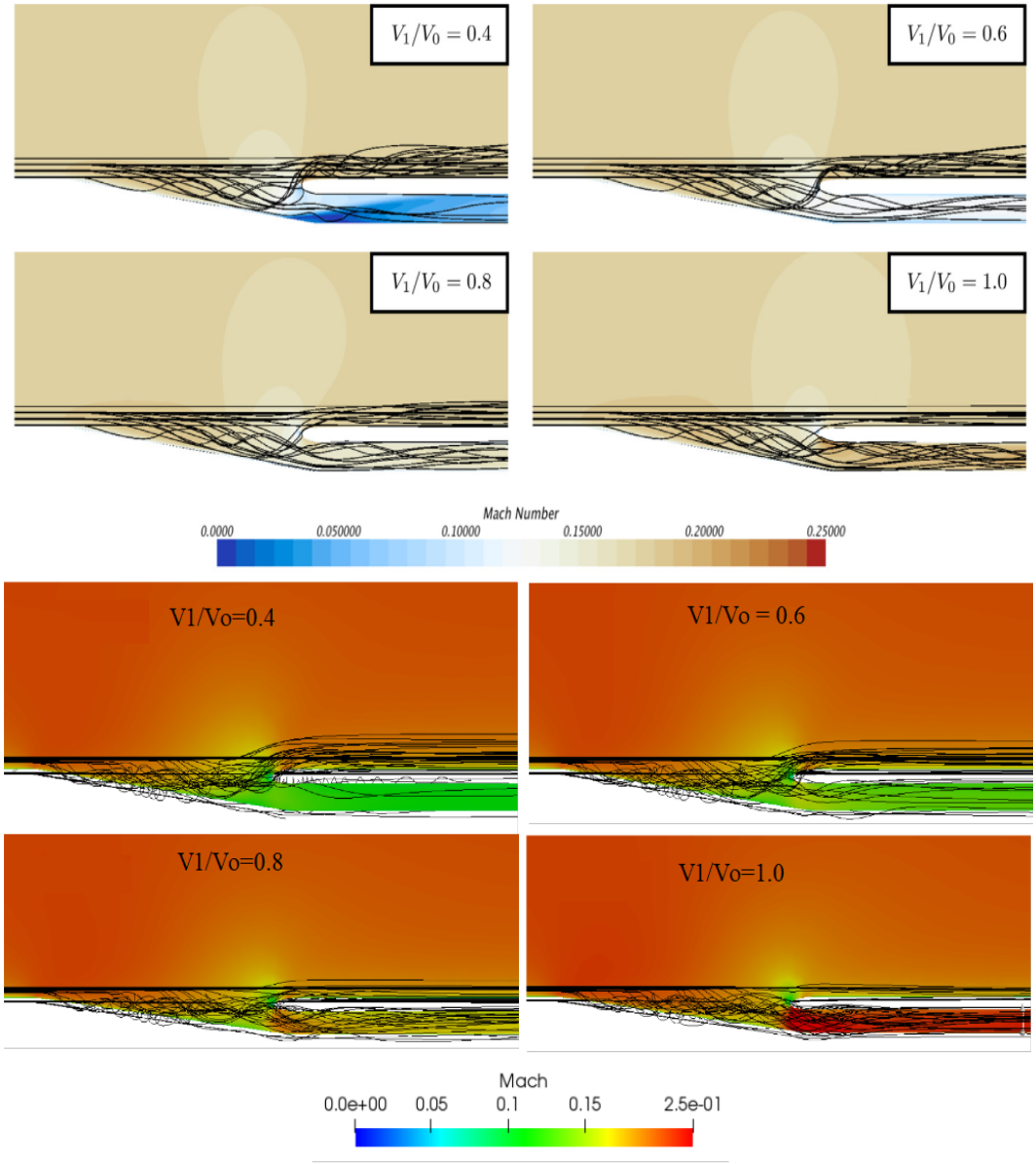

Figure 3.6: *Top:Mach filled centre-plane slice with streamlines [5]. Bottom: CFD result corresponding to present study.*

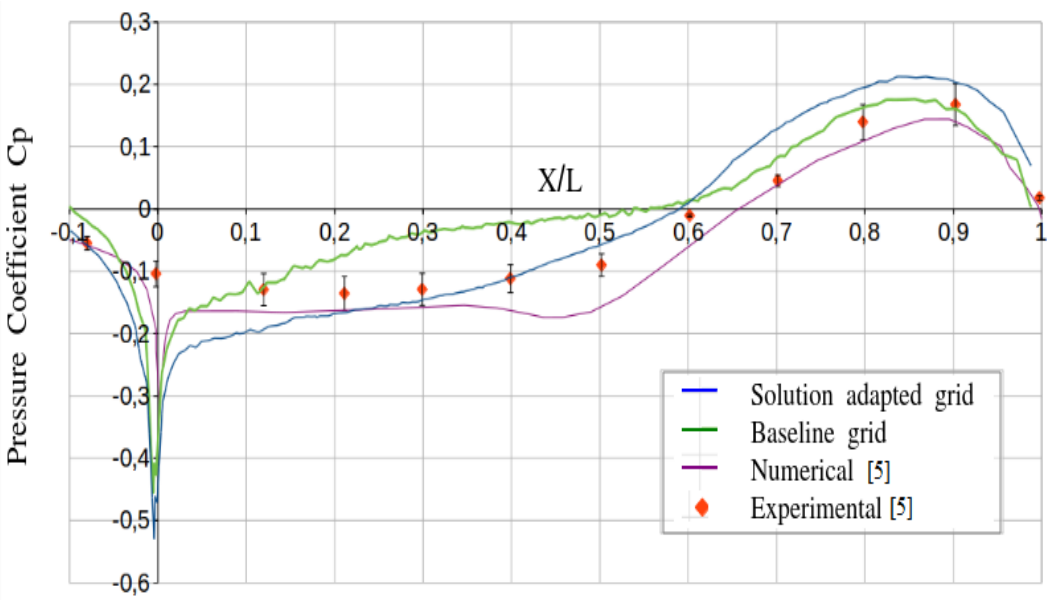

Figure 3.7: *Comparison with reference study of Cp distribution along intake ramp center line*

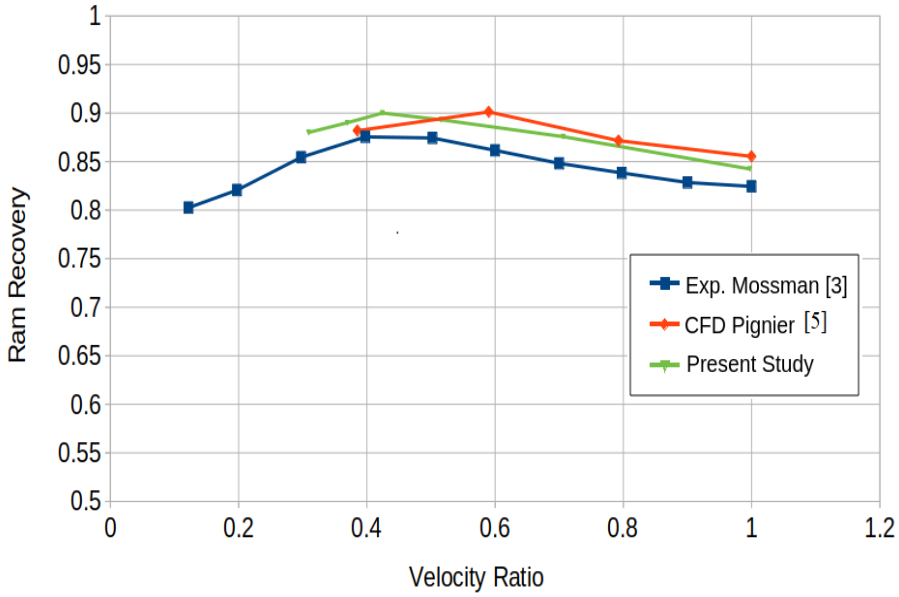

Figure 3.8: *Comparison of ram recovery for NACA intake at Mach=0.2*

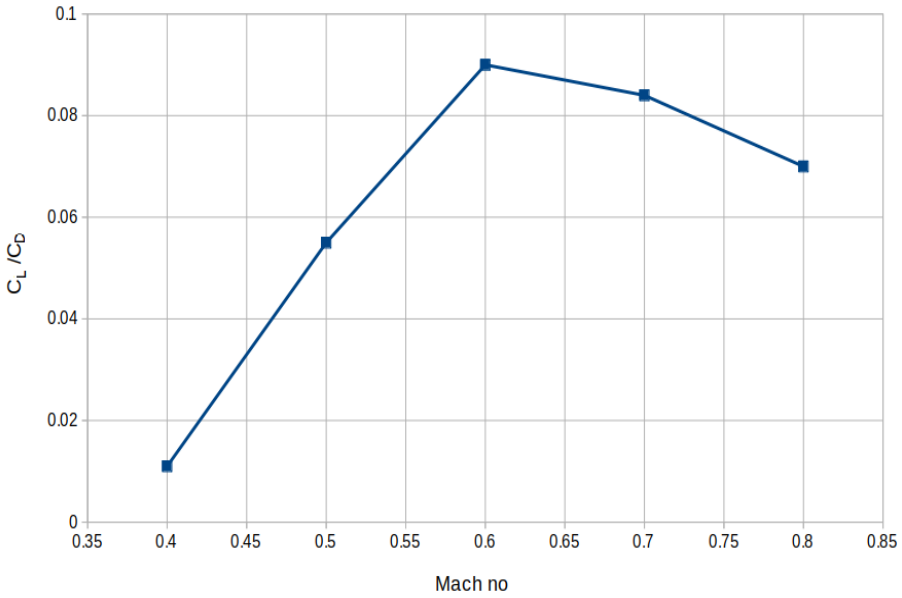

Figure 3.9: *C_L/C_D of NACA intake a flat plate.*

Lifting properties of the NACA intake on flat plate are observed and estimated. Figure 3.9 shows the behavior of C_L/C_D for different values of freestream flow Mach number and it can be clearly observed that while the values remain nominal for the whole range however the maximum is achieved at Mach number 0.6. As it will be seen later this value will be taken as the baseline and then considerable improvement will be obtained by undergoing the shape optimization procedures. The flight conditions are determined for the baseline case which will be used in the shape optimization study. The objective function to be employed is C_L/C_D therefore the performance of the intake is evaluated at different flight conditions. The maximum C_L/C_D is obtained at freestream Mach number of 0.6 therefore it will be the baseline case for optimization.

3.2 Case II: Trapezoidal Entrance Intake on Slender body

In this case Case II and III are for aerodynamic shape optimization of a trapezoidal submerged intake placed on a slender body. The geometry is defined in identically however the difference is in the definition of design variable surfaces as described later. The shape is already optimized manually and characterization study provides detailed experimental data on its design and off-design performance [4].

3.2.1 Geometry Definition and Mesh Generation

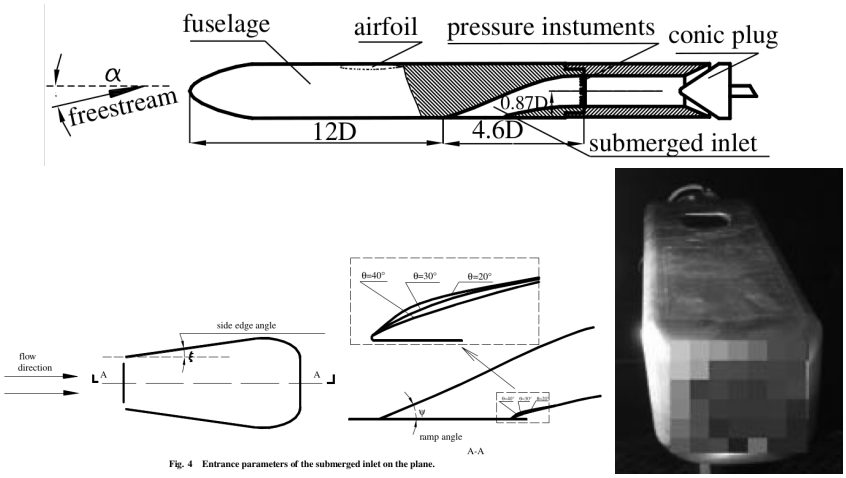

Figure 3.10: *Reference geometry for trapezoidal submerged intake [4].*

The geometry for the present study is obtained from a published study by Shu Sun [4] in which characterization study of the trapezoidal submerged intake is done by varying side edge and ramp angle at operating Mach number = 0.7 based on both experimental and numerical results.

The reference trapezoidal intake geometry and placement in the slender body is shown in figure 3.9. Similar geometry is modeled in SALOME for 4° side edge angle and 23° ramp angle and location is at the same ratios while some arbitrary dimensions are used since exact geometric specifications such as AIP diameter and duct curvature splines are not available. The modeled geometry is flipped over such that the intake faces towards the positive y-direction as shown in figure 3.10. This is done in order to align the geometry for lift optimization. The dimensions of the computational domain is shown in figure 3.11. The size of the computational domain is same as the previous

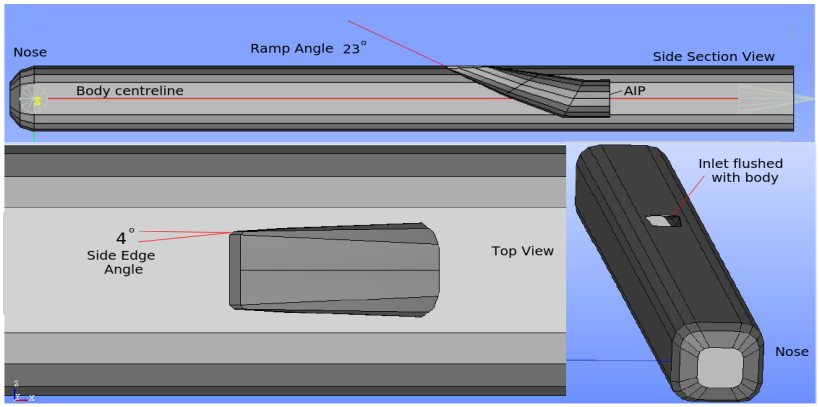

Figure 3.11: *Solid modeling of intake in a slender body by SALOME.*

case with 20 times the body diameter in the side direction and 20 times the length of the body in axial direction. GMSH [117] is used to generate hybrid 3D mesh with a boundary layer zone as shown in figure 3.12. The GMSH provides extrude feature for prism layer mesh with gradual size steps to resolve viscous boundary layer over which the unstructured tetrahedral mesh can be created. The height of the wall adjacent cell is 1.6e-06 m which is calculated for Mach number = 0.7 and Reynolds no = 1.56e6. Note that the last prism layer cell before the unstructured mesh starts is almost square cross section.

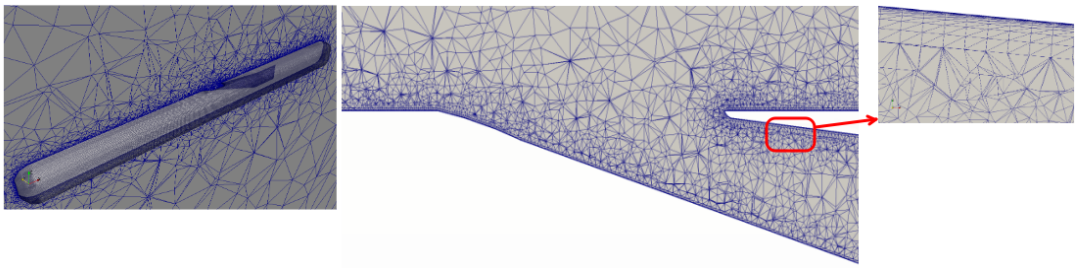

Figure 3.12: *3D hybrid mesh generated by GMSH . Inset shows the prism layer clustering in boundary layers.*

3.2.2 Flow Solution and Mesh Independence

The direct solution for the case is run in SU2 direct flow solver for for Mach number = 0.7 and Reynolds no = 1.56e6 for grid sensitivity study. Wall surfaces taken at adiabatic condition (Heat flux = 0). The intake AIP is taken at $p_2/P_0 = 0.8$ as the outlet boundary condition. The turbulent flow solutions are obtained on a baseline grid as well as the solution adapted grid. SST model are used to resolve the flow.

The Y+ distribution on surface due to flow solution is shown in figure 3.13. The Y+ is within 1 for the surface except edges where it approaches value of 4. The mesh independence is achieved through the mesh adaptation process as described in previous section. The baseline mesh generated by GMSH is solution adapted repeatedly allowing the mesh size grow twice its current size. The grid size and solution obtained at each adaptation level in terms of total pressure recovery factor is given in table 3.2. As seen, the adapted grid after the first adaptation step with 1.55 million cells provides a converged solution and differs from the reference study by -0.504%. Therefore it is taken as the optimum mesh which provides grid independent solutions and is used for the verification and optimization studies.

Table 3.2: *Mesh Independence Study at* $M = 0.7$.

Mesh Size	Total pressure recovery factor	Difference%
750,000	0.8935	1.380
1,550,000	0.898	-0.504
2,500,000	0.899	-0.111
3,250,000	0.8995	-0.056
6,020,000	0.8996	-0.011
[4] Sun	0.906	-

Both qualitative and quantitative verification of the flow solutions are carried out for the baseline case. The Mach number contours are presented and favorably compared

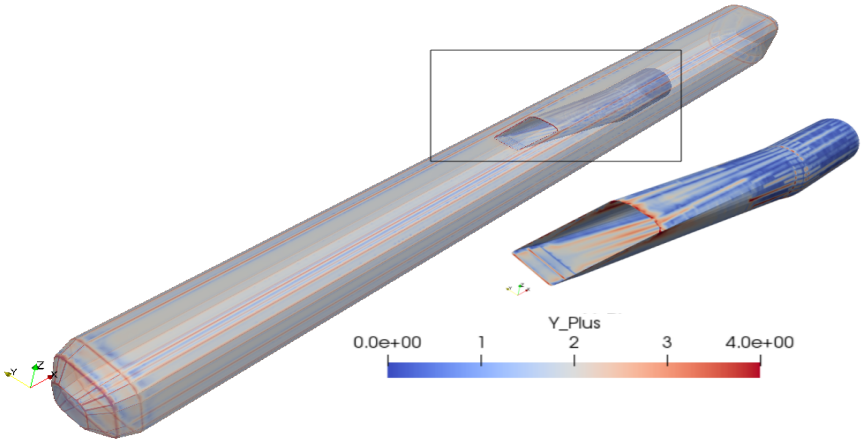

Figure 3.13: *Y+ distribution on body and intake surface.*

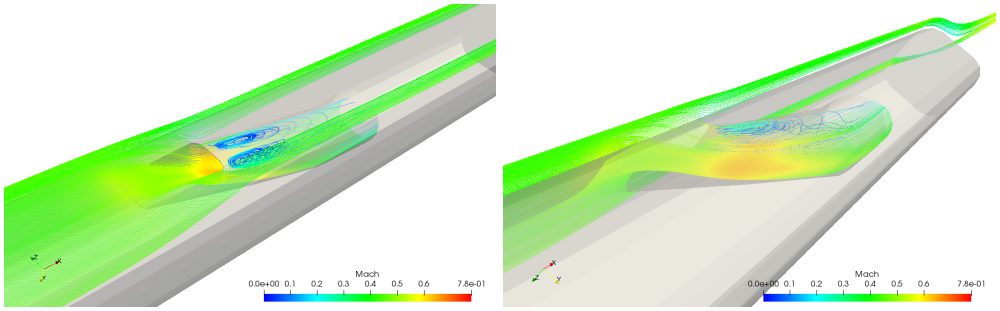

Figure 3.14: *Mach colored streamline around intake.*

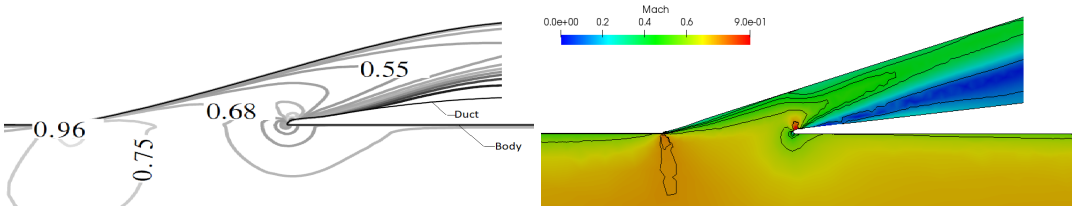

Figure 3.15: *Mach contours. left: Reference study [4] Right: Baseline solution.*

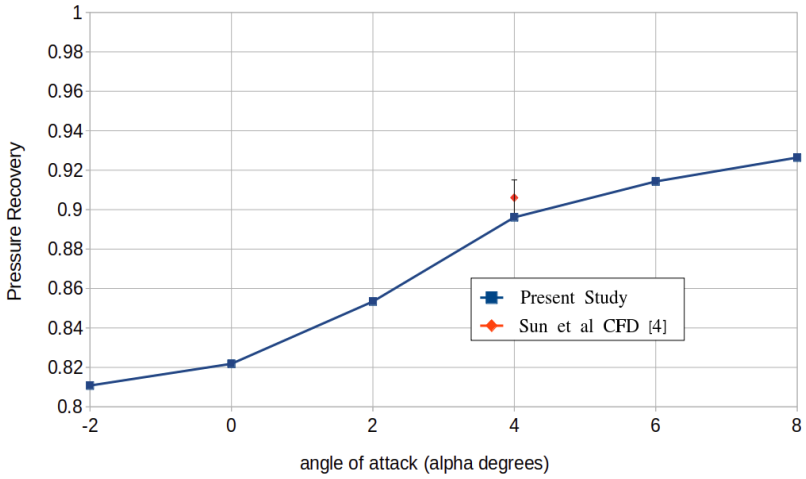

Figure 3.16: *Total pressure recovery factor versus angle of attack.*

to the reference study in figure 3.14 and 3.15. It is observed that flow enters the intake smoothly and remains attached along the ramp however on the the lip side of duct surface flow separates aft of the lip. The separation is accompanied by a local shock formation at the lip. The flow separation causes pressure losses but at the same time helps the pressure over the duct upper surface decrease and thus creates the pressure differential in favour of generating a lifting force. For a clean body with no intake cavity, the net force lateral to body is zero at zero angle of attack, in other words lift does not exist for such a symmetric flow but in the present study the flow enters the submerged intake laterally in an asymmetric fashion and contributes to the lift generation. The validation of present study deduced on the basis of the mesh

independence study is presented in table 3.2. Total pressure recovery factor compares favorably with the reference results with a difference of less than 1% as shown in figure 3.16.

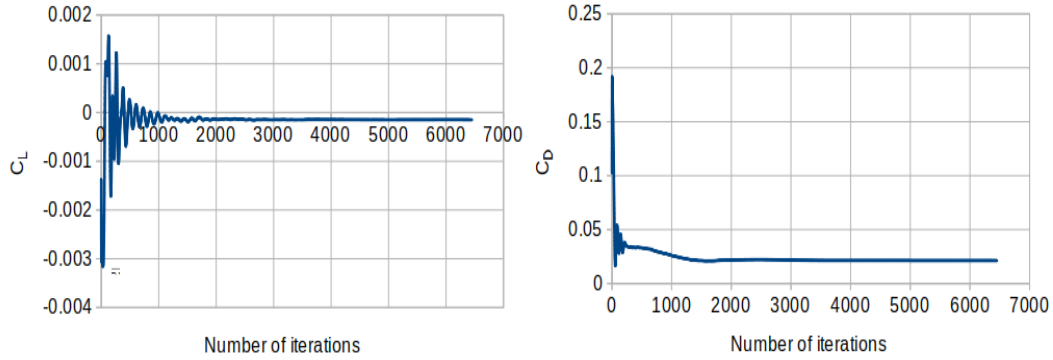

Figure 3.17: *Convergence history for trapezoidal intake on slender body at Mach number 0.7.*

CHAPTER 4

OPTIMIZATION STUDY

Aerodynamic shape optimization results for four cases of submerged intake are presented. The first case is that of a NACA intake on flat plate optimized for lift. The second case is for trapezoidal flush intake on slender body optimized using multi-objectives and multiple FFD boxes. The third case is of a circular intake optimized as semi-submerged intake using multi-objective function and finally trapezoidal intake is optimized with similar semi-submerged deformation as in third case. Lift and total pressure at AIP are the objective functions for all multi-objective cases and drag is the penalty constraint.

4.1 Case I: NACA Intake on Flat Plate

A NACA intake placed on a flat plate placed at 0 angle of attack in freestream flow of Mach 0.6 is solved as baseline for optimization. The intake AIP is fixed at $p_2/P_0 = 0.95$ as the outlet boundary condition. The objective function is taken as lift coefficient C_L while the intake surface as the design variable. The optimization surface employed as design variable is already shown in figure 2.16.

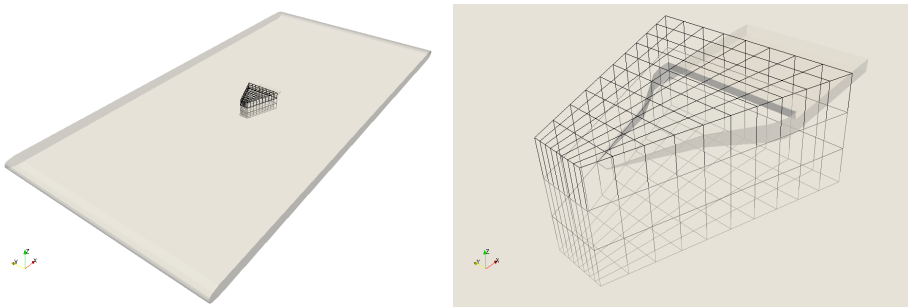

Figure 4.1: *FFD Box enclosing the NACA intake.*

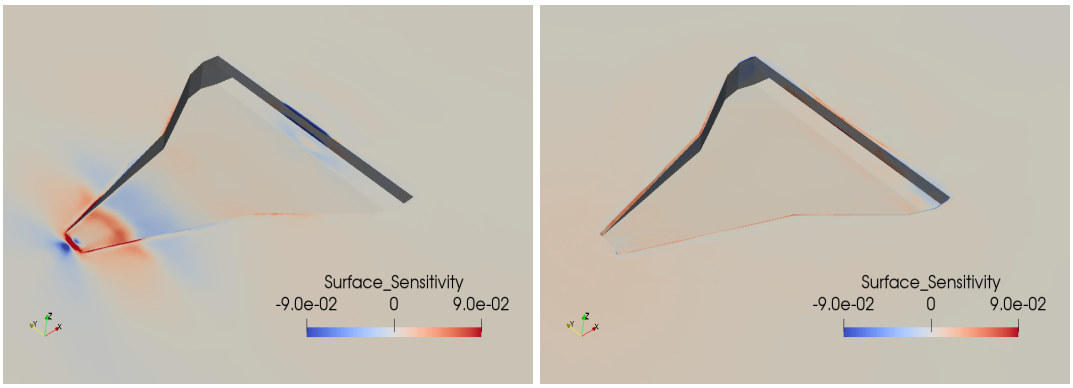

Figure 4.2: *Lift calculated surface sensitivity; Left: Baseline; Right: Optimum design.*

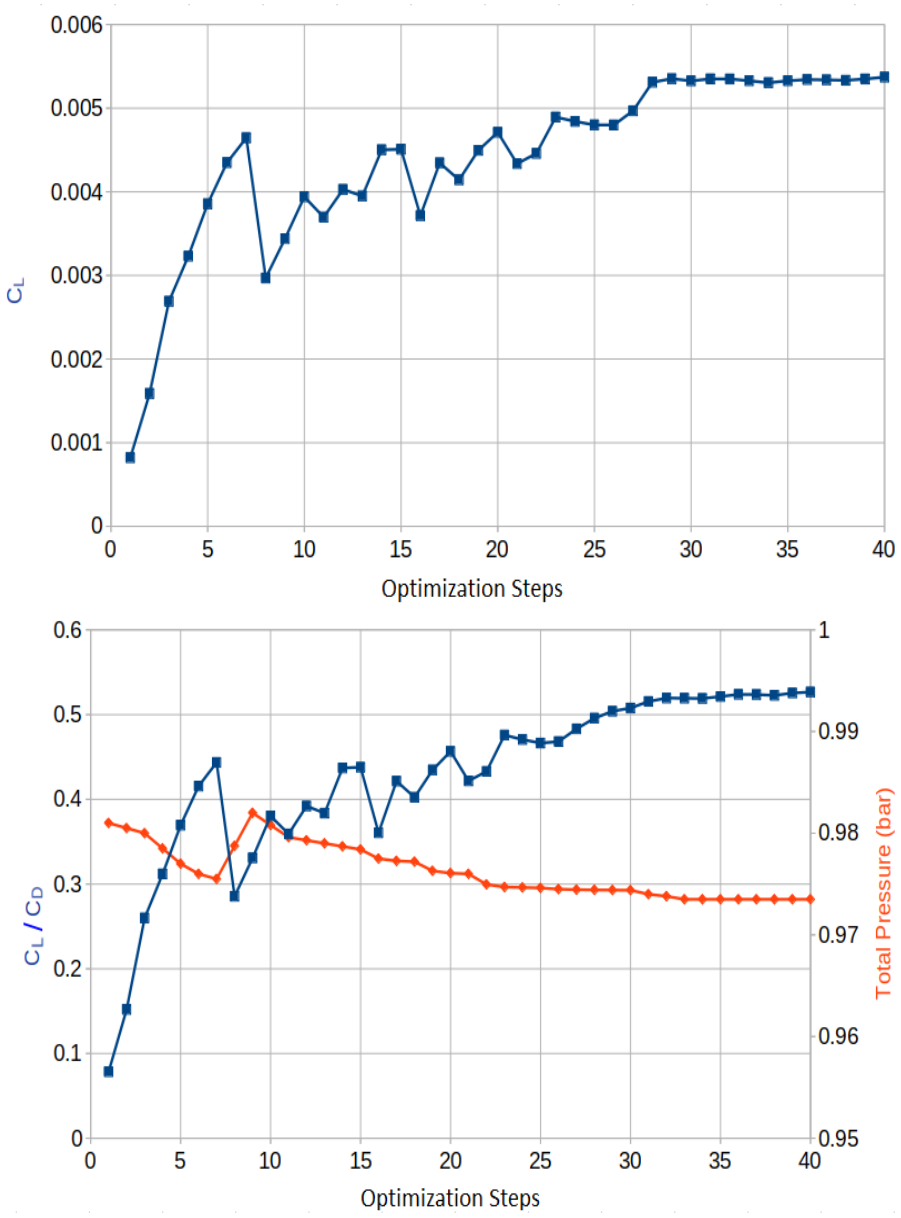

Figure 4.3: *Top: Optimization steps for C_L. Bottom: C_L/C_D and Total pressure recovery (monitors).*

The shape optimization of the NACA intake for the single objective function commences once converged mesh independent results from direct CFD solvers are obtained.The FFD box placed over the design space, which defines the design variables, is shown in figure 4.1. The control points on the FFD box (10,8,3) provides a total of 396 design variables. The adjoint sensitivity for the objective function of lift is shown in Figure 4.2. The baseline design clearly indicates a strong variation at the fore lip however in the optimum design the surface adjoint values become less pronounced to give a uniform value. The optimizer iterations for C_L is given in figure 4.3. The lift coefficient as the objective function increases from 0.0009 to 0.0053 The result of the shape modification due to the optimization study gives the final value at the 40th optimization step of $C_L/\ C_D$ = 0.52 which is more than six times the baseline value. The shape variations can be seen in figures 4.4 to 4.6. The 3D close up view indicate fore lip shape variation is prominent. The section view for the fore lip shows that while the ramp is flushed at the baseline there is initially an increase in height in the intermediate case (red) which later changes into a depth for the optimized design (blue). The top view shows a nominal bend in fore lip which develops into a convex curve. The Cp distribution on sections along axial direction of the ramp floor are shown in figure 4.7. At both the locations the Cp for optimized case is lower in value as compared to the baseline case.

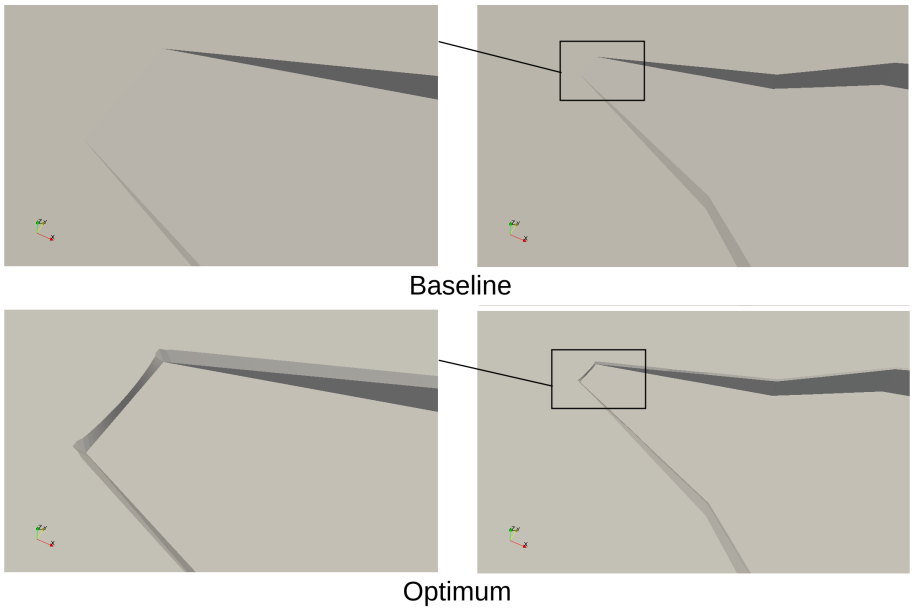

Figure 4.4: *Fore lip deformation due to optimization; Top:Baseline design; Bottom:Optimum design*

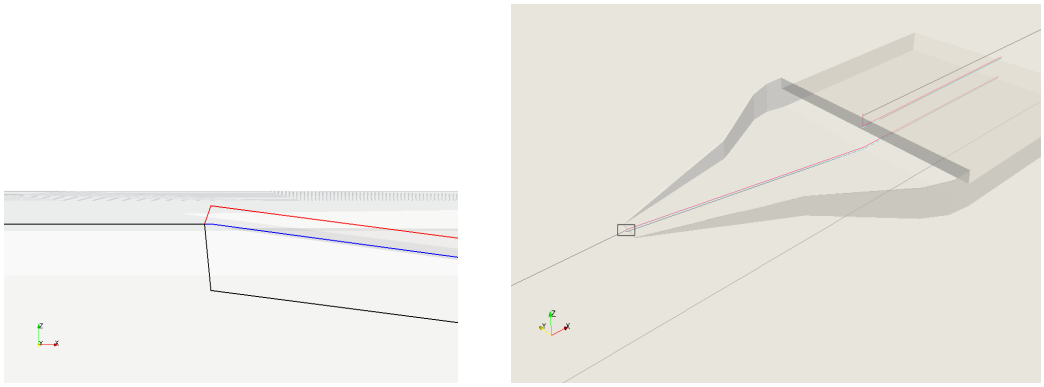

Figure 4.5: *NACA intake fore lip section view at different optimization steps; Outlines: Blue: Baseline ; Red: Intermediate ; Black: Final step*

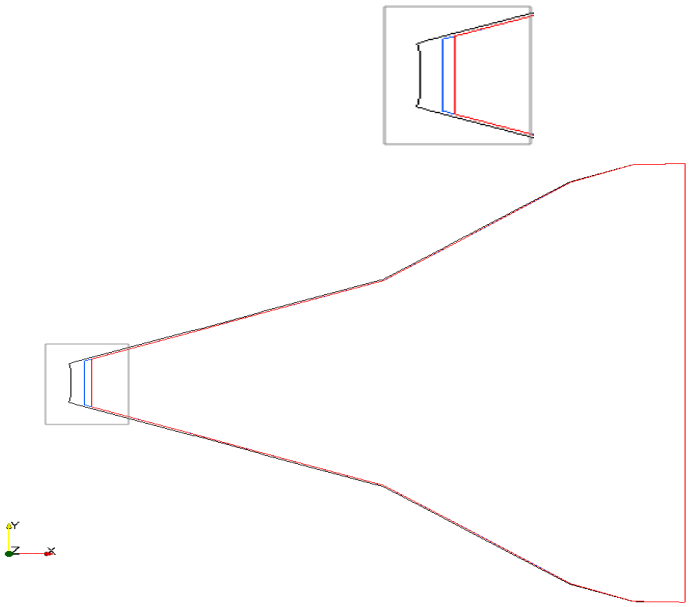

Figure 4.6: *NACA intake top view at different optimization steps; Outlines: Blue: Baseline ; Red: Intermediate; Black: Final step*

The Cp distribution also changes inside the duct due to which a net negative ΔCp is obtained between the upper and lower duct wall surfaces as shown in figure 4.8. The flow variation due to shape deformation is observed in figure 4.9, where it can be seen that there is increase in flow entering the duct which is mostly flowing outside for the baseline .

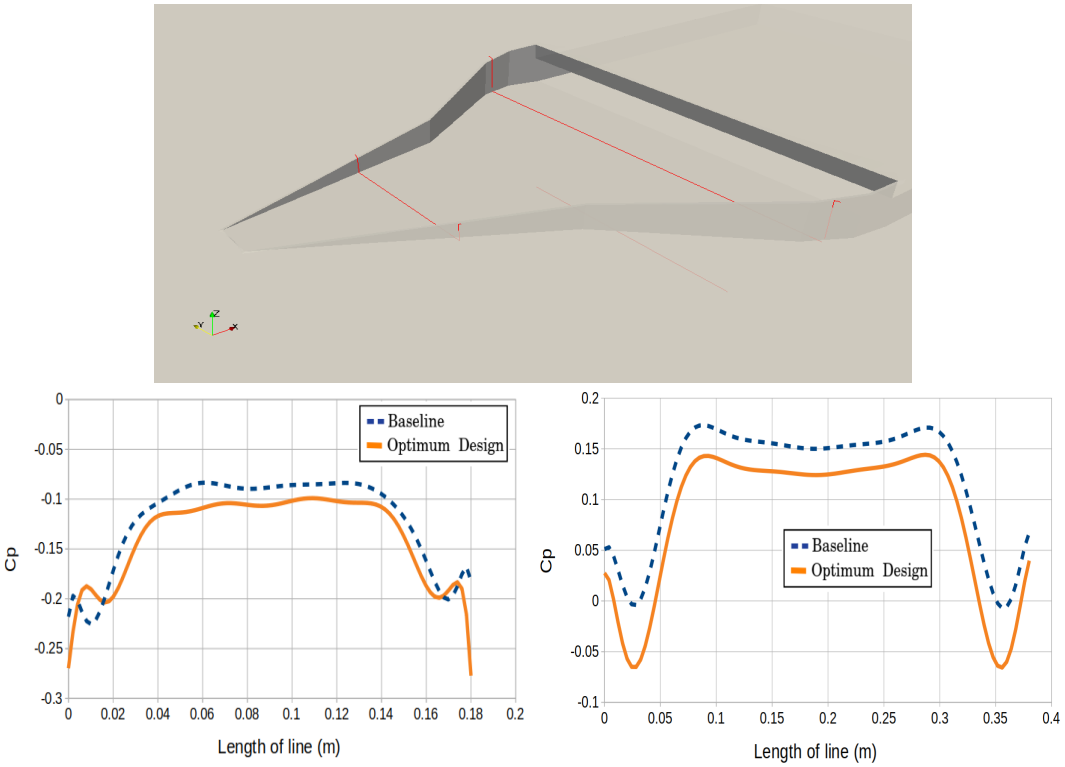

Figure 4.7: *Cp distribution along intake ramp sections.*

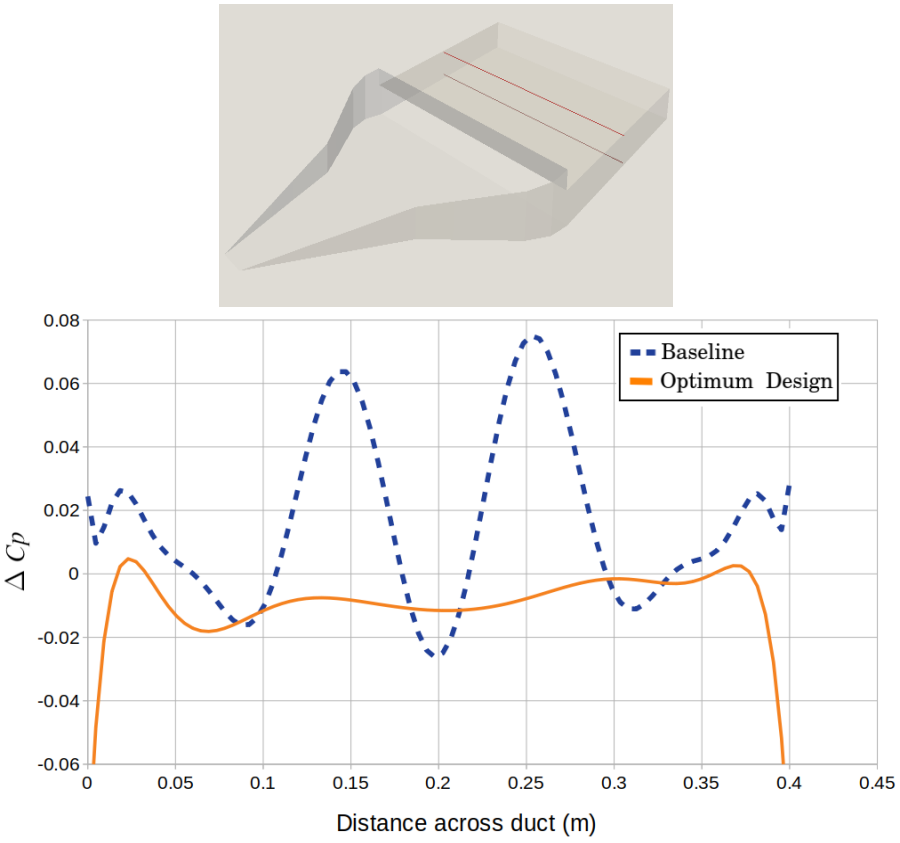

Figure 4.8: *Δ Cp distribution between upper and lower duct walls.*

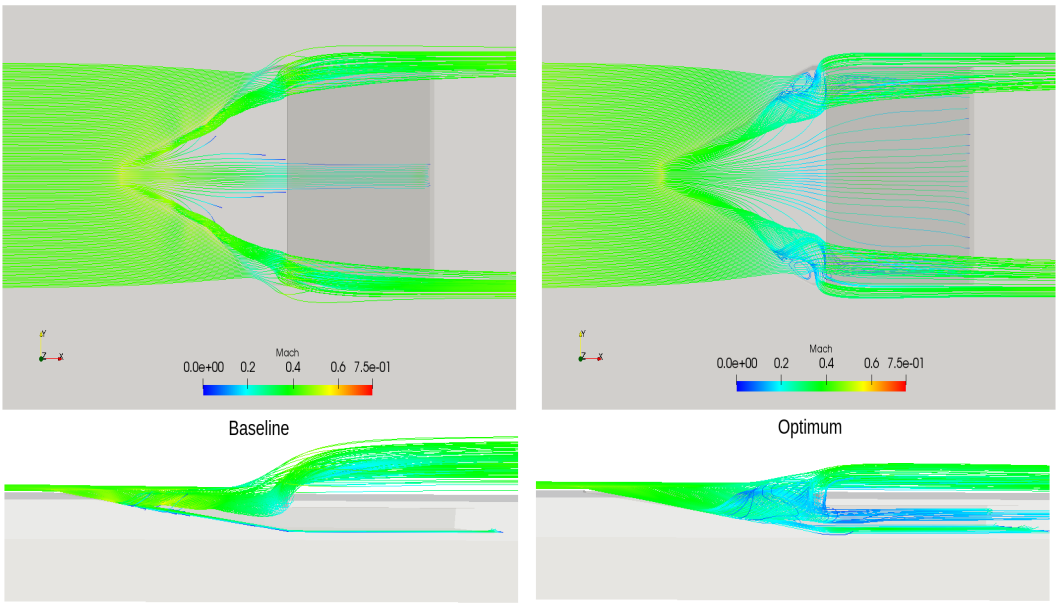

Figure 4.9: *Mach filled streamlines. Left: Baseline Right : Optimum design*

Table 4.1: *Optimization Summary for case I.*

	Baseline	Optimum Design	Change
C_L	0.0009	0.0053	0.0044
$C_L/\ C_D$	0.085	0.52	0.435

4.2 Case II: Trapezoidal-entrance Flush Intake on Slender Body

Case II is of trapezoidal-entrance flush intake. In this case the intake remains flush with the body such that body surfaces remain intact. The design space is shown in figure 4.10. The design surfaces include the intake duct only which deform accordingly during optimization and improvement in performance relate to the shape variation in the internal flow through duct.

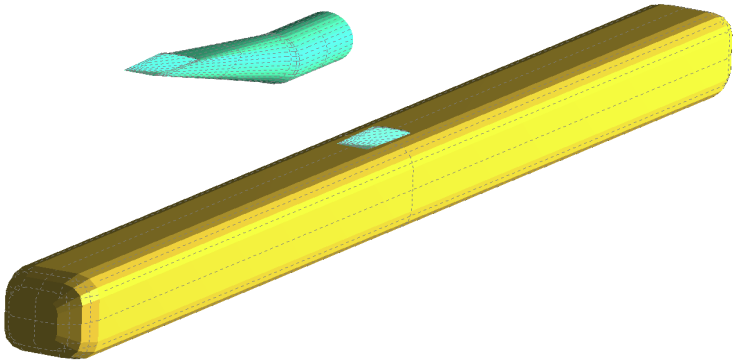

Figure 4.10: *Design variable surfaces in blue with and without full body in yellow.*

Multiple FFD boxes approach is undertaken for this case. There are two FFD boxes placed over the design space as shown in figure 4.11. The ramp surface leading from the fore lip to the AIP pipe is enclosed by red FFD box while the rear lip and portion of duct downstream is enclosed by blue FFD box. Both FFD boxes of (8,6,6) configuration provide a total of 2x441 control points. The main feature of this case is the simultaneous deformation process of multiple FFD boxes operating over a design surface.

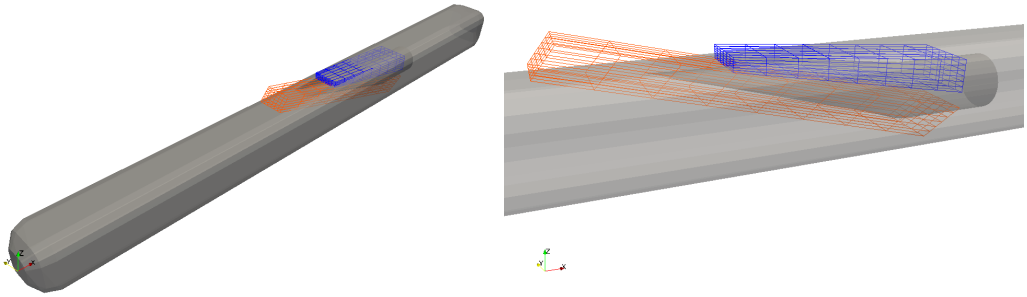

Figure 4.11: *Multiple FFD boxes enclosing the design variable surfaces; FFD box-1 in orange; FFD box-2 in blue.*

The optimization history for the objective function as total pressure at AIP is given in

figure 4.12. The design optimization stops after 25 steps when the combined objective function attains constant value. The total pressure recovery factor increases from baseline value of 0.82 to optimum value of 0.84 which is a 3 $\%$ increment considering that the full body drag constraints the optimization process. The overall lift also increases where the value of C_L/C_D of the complete vehicle increases from -0.007 to 0.01.

The shape deformation enclosed in the deformed FFD box is shown in comparison with the baseline design in figure 4.13. The adjoint sensitivity distribution of the combined objective for baseline and optimum design are compared in figure 4.14. It should be noted that at the end of the optimization process the surface sensitivities reduce to give almost negligible distribution at the optimum design.

The 3D views and the center-plane cross-sectional outlines are also given in Figures 4.15 and 4.16 respectively. As illustrated, in the optimum design the upper portion of duct aft the rear lip up to the fixed duct is deformed considerably. The intake duct which is initially a straight diverging duct deforms to form a curved shaped duct. While the upper duct surface bulges towards the outer direction, lower surface bends inwards. There is a formation of a backward facing step at the onset of ramp as shown in figures. Overall the variation is prominent and duct remains flush with the body. The pressure distribution at baseline and optimum design can be seen in figure 4.17 and 4.18. As observed the quality of flow improves and the pressure distribution shows an increase in the total pressure value in the optimum design as compared to the baseline. The mach filled streamlines are illustrated in figure 4.19. The new shape improves the flow as the re-circulation zone is reduces in size due to curvature of duct in optimum geometry compared to the straight duct of the baseline.

Hence it is observed clearly that the baseline geometry is of a fully submerged intake in which the entrance is tangential to the freestream flow while after optimization the shape remains flush.

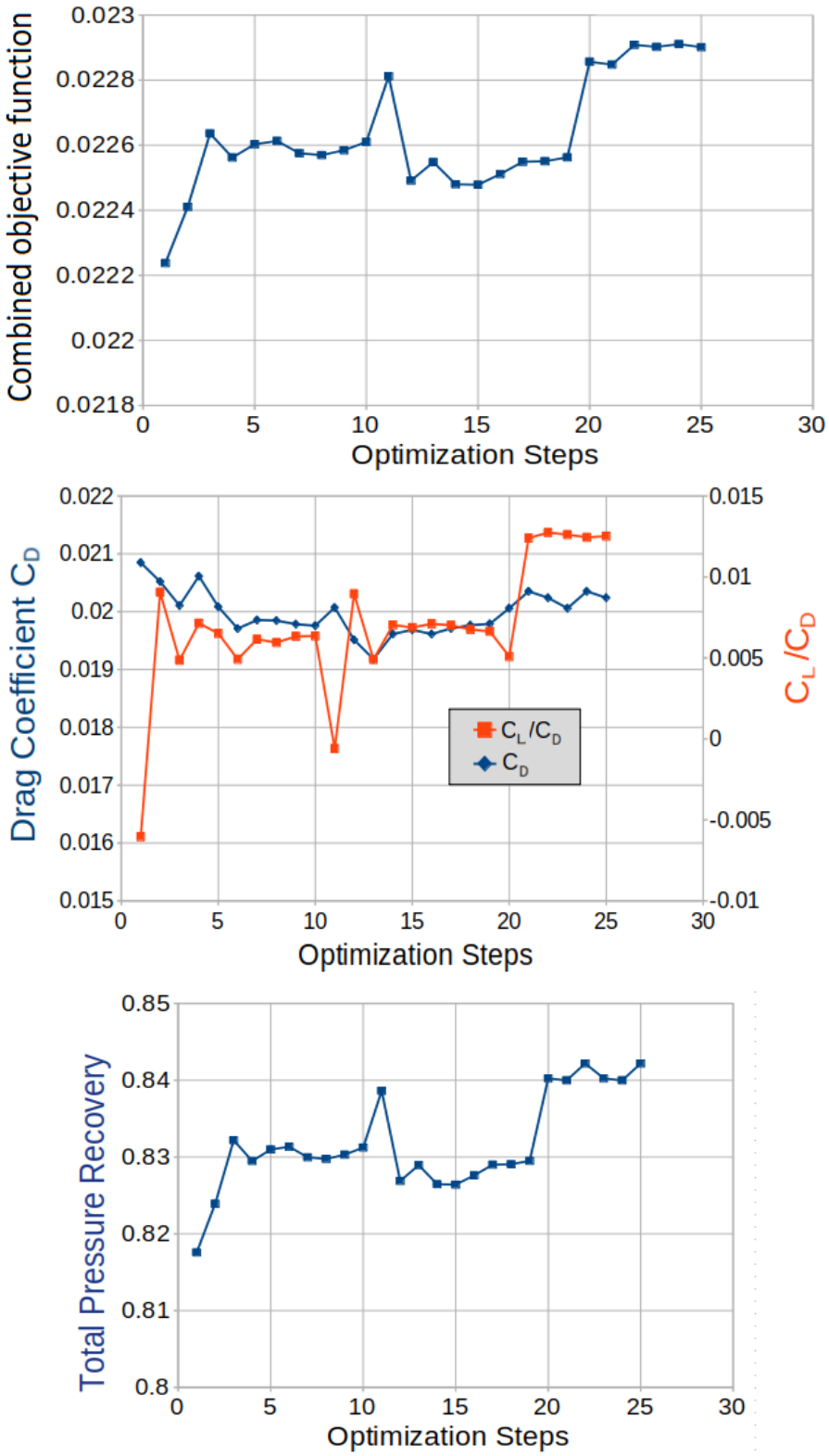

Figure 4.12: *Optimization history C_L/C_D and σ total pressure recovery factor*

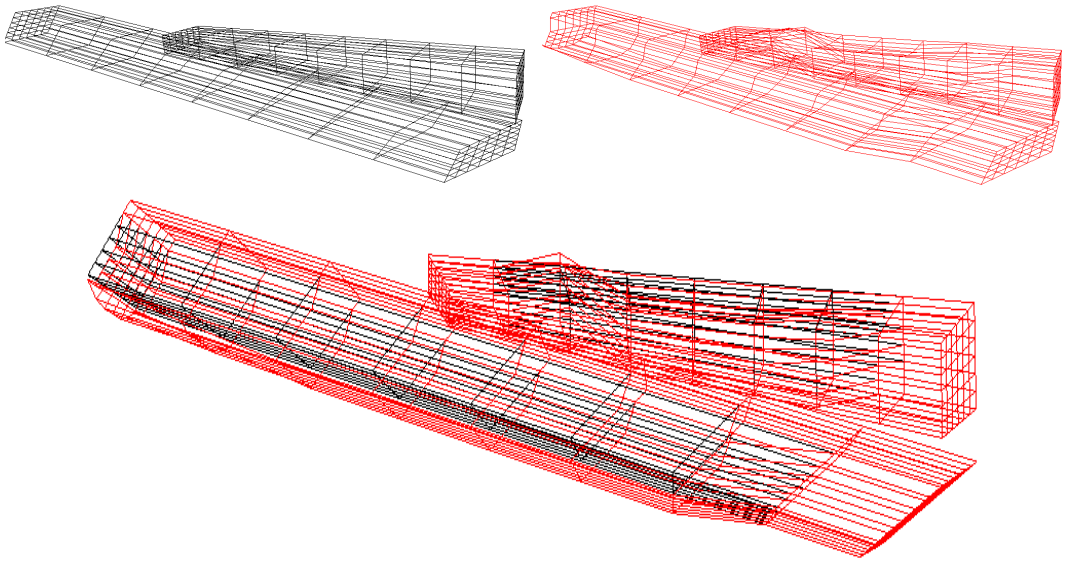

Figure 4.13: *FFD Box deformation: Top left in Grey: Baseline ; Top right in Red: Optimum; Bottom: Overlap of baseline and deformed FFD boxes.*

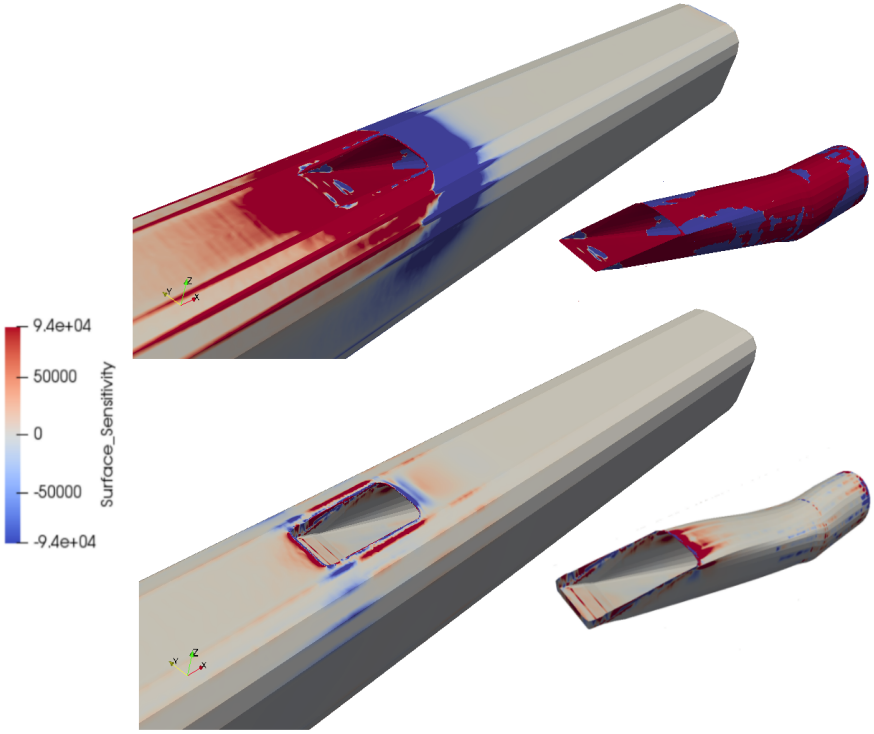

Figure 4.14: *Surface sensitivity: Top Baseline design ; Bottom Optimum design*

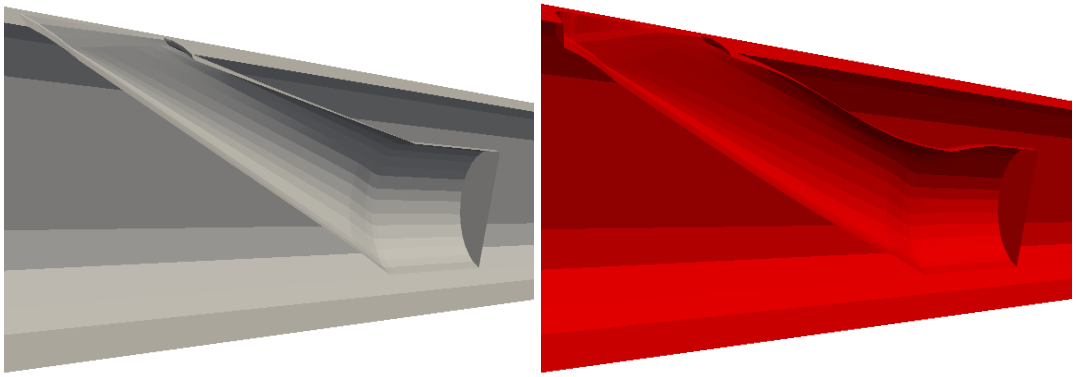

Figure 4.15: *3D view of shape deformation process: Left: Baseline, Right: Optimum design.*

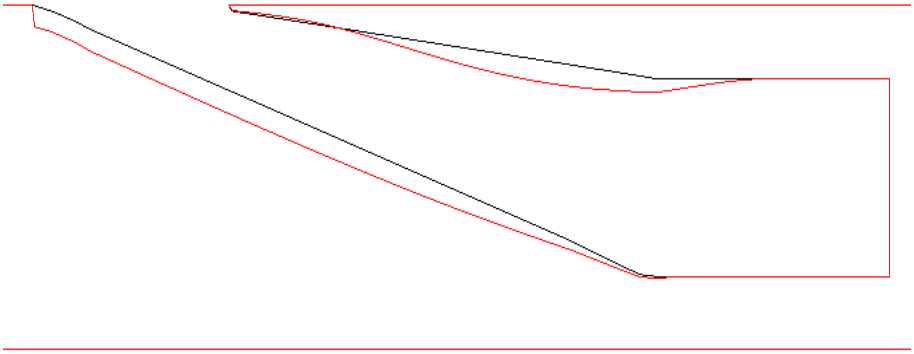

Figure 4.16: *Intake duct at center plane : Black: Baseline, Red: optimum design.*

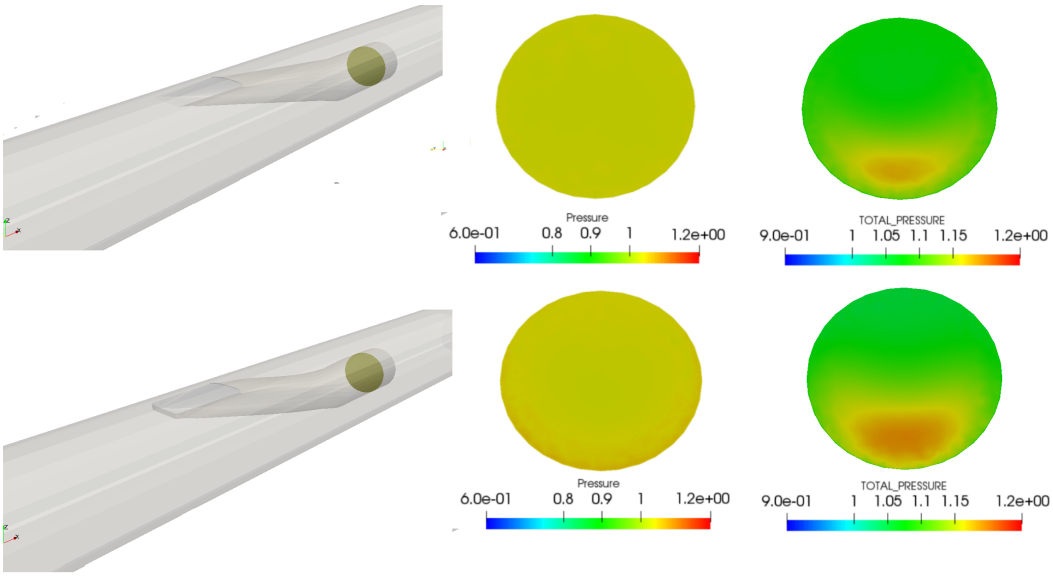

Figure 4.17: *Pressure at AIP. Top: Baseline; Bottom: Optimum design*

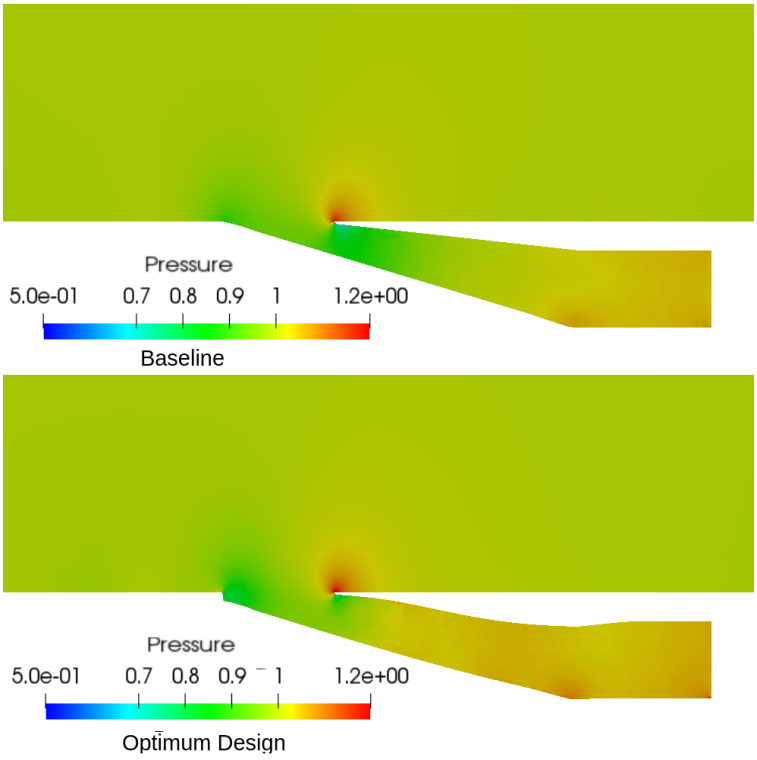

Figure 4.18: *Pressure distribution on center-plane - Top: Baseline , Bottom: Optimum design.*

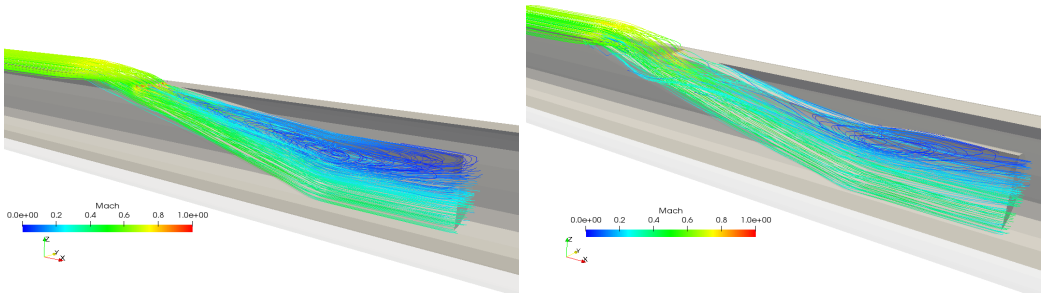

Figure 4.19: *Stream lines coloured with Mach number. Left: Baseline; Right: Optimum design.*

Table 4.2: *Optimization summary for case II.*

	Baseline	Optimum design	Change
σ	0.82	0.845	+3 %
$C_L/\ C_D$	-0.007	+0.011	+0.018
C_D	0.021	0.02045	-2.8 %
DC(90)	18.1	7.7	-10.4

4.3 Case III: Circular-entrance Semi-submerged Intake on Slender Body

Case III is aerodynamic shape optimization for a circular entrance intake placed on a slender body.

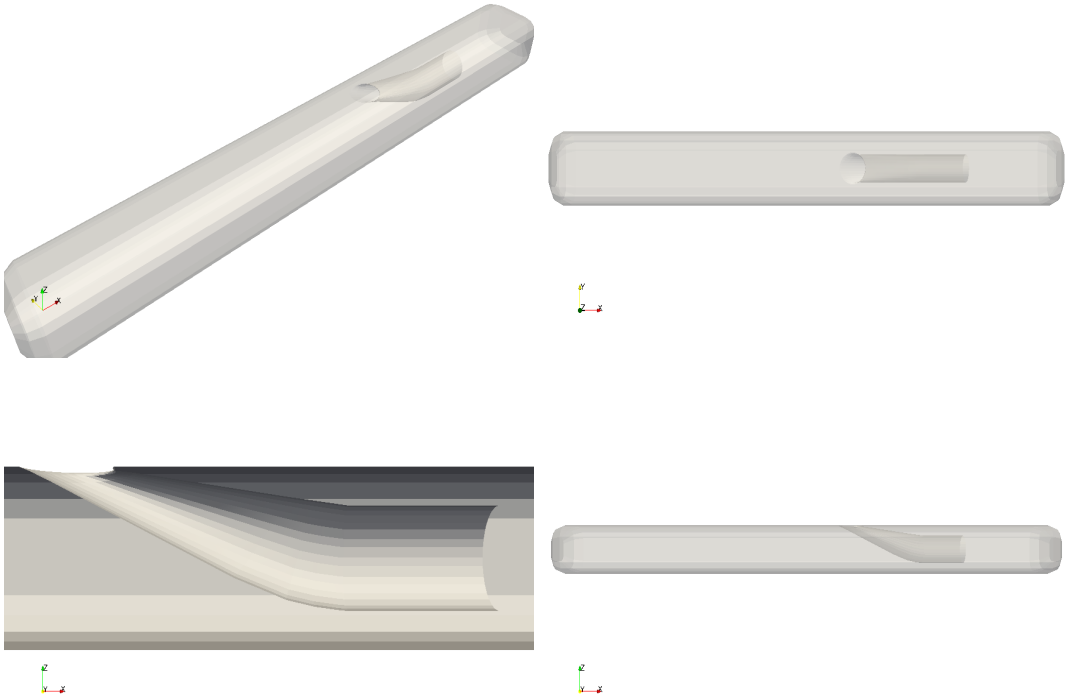

Figure 4.20: *Circular intake top-mounted on slender body*

In this case study a slender body of similar shape and dimensions as in case II is employed , however the entrance is not trapezoidal but with a circular entrance. The slender body is also not of equal sides as in the previous case and a width twice the height is taken. The AIP is of the same area as the opening as shown in figure 4.20. The length of the body is approximately the same as that of slender body in trapezoidal case.

The geometry and surfaces were modeled in SALOME and meshed in GMSH using the same hybrid mesh technique as mentioned in chapter 2. The prismatic boundary layer mesh with the unstructured tetrahedral mesh around the intake region are shown in Figure 4.21. The mesh size used in the study has 3.2 million cells with 1.8 million cells in the prism layer and 1.4 million tetrahedral cells. The height of wall-neighbour prism cell is evaluated as 1.7e-06m for y+ = 1 and Reynolds‘ no =

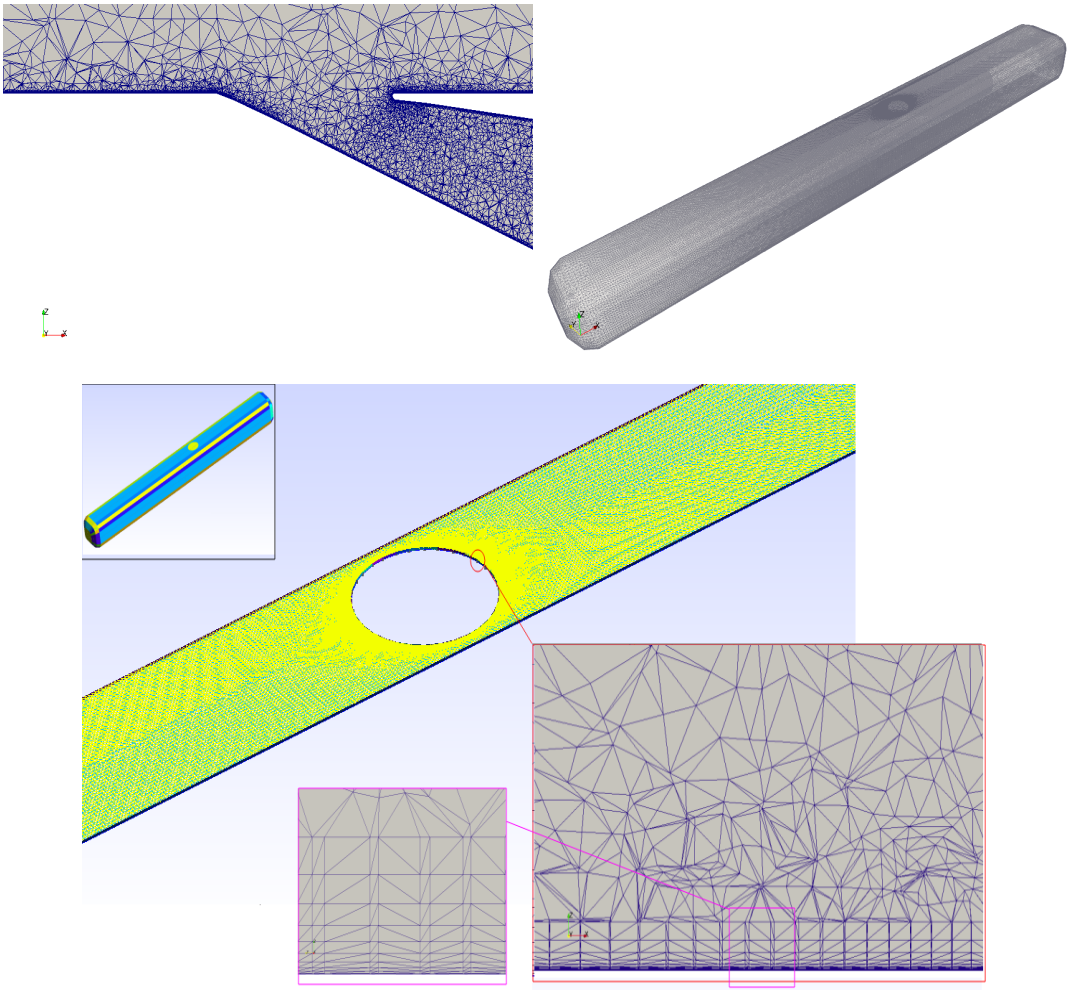

Figure 4.21: *Hybrid mesh developed in GMSH. The prism layer mesh is visible around circular intake region.*

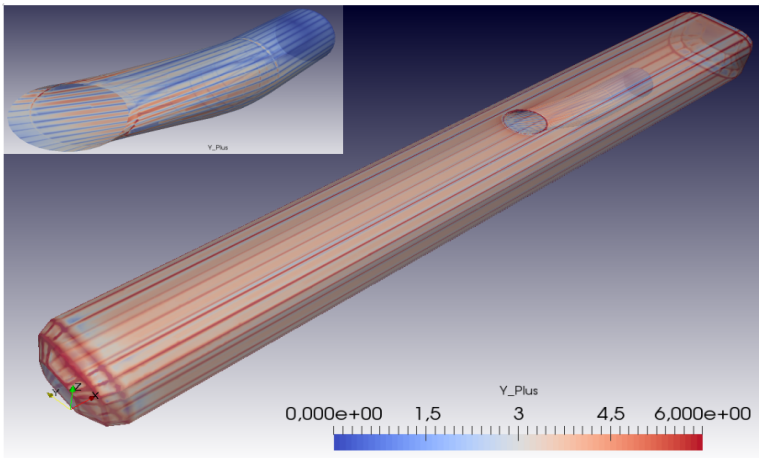

Figure 4.22: *Y+ Distribution on surface.*

2.5e06 at Mach number = 0.7. The cell growth is 1.15-1.25 for 10 cells as total prism layer corresponding to BL thickness while maintaining a square shaped final

cell before merging with the tetrahedral mesh. The size of the computational domain is same as the previous case with 20 times the body diameter in the side direction and 20 times the length of the body in axial direction. The Y+ distribution from the flow solution is shown in figure 4.22. As aforementioned, this geometry is introduced as a arbitrary shape in the present study and since no published result is available therefore the flow solution is not required to be validated. The optimization surfaces are shown in figure 4.23. The surfaces include the intake duct and the upper body surface which is flush with the intake. The rest of the body as shown in blue is not part of the optimization process. The optimization procedure is similar to the case of the trapezoidal-entrance intake and almost all solver and deformation parameters are same including the combined objective function in which total pressure and lift are optimized and drag is the penalty constraint. The FFD box information is embedded in the .SU2 file by running the SU2_DEF command after the mesh is generated. The direct CFD solution obtained from the baseline are employed to find the sensitivity of objective function due to the deformation of the design variable with respect to the given control point movement on FFD box using the equations derived. The FFD box which define the control points is placed over the design space as shown in figure 4.24.

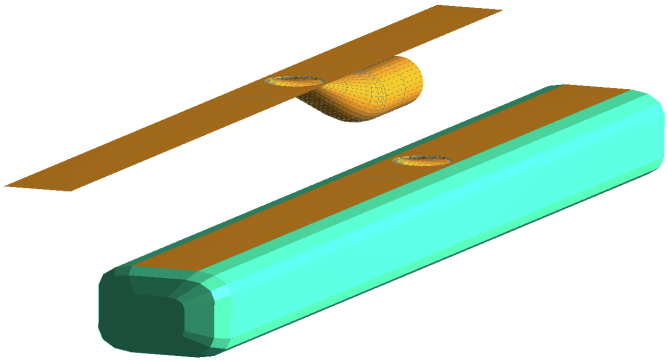

Figure 4.23: *Optimization surfaces in brown with and without full body in blue.*

The control points on the FFD box (8,6,6) provides a total of 441 points. Once the grid sensitivities for the combined multi-objective function are computed by the adjoint solver, they are projected onto the design variables through SU2_DOT. The optimization history for the combined and the individual objective functions are given in figure 4.25. The design optimization converges after 23 steps as the

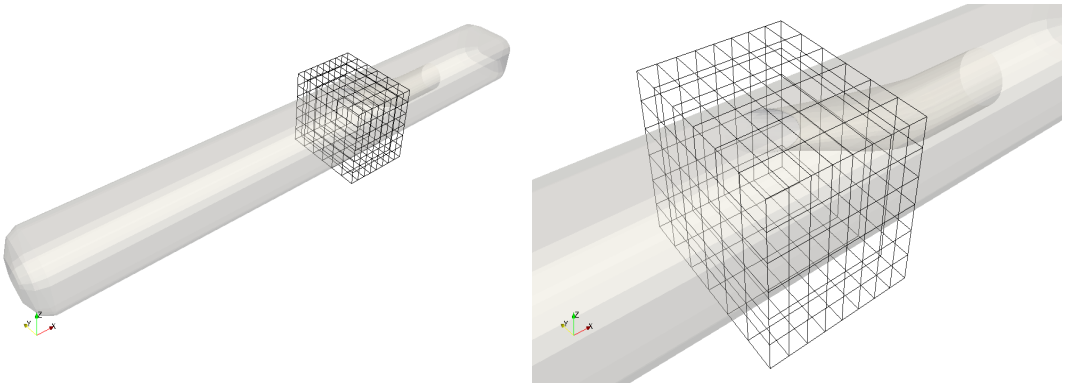

Figure 4.24: *The FFD Box composed of control points enclosing the intake and regions of interest.*

combined objective approaches a constant value. The total pressure recovery factor increases from baseline value of 0.81 to optimum design value of 0.825 which is a 2 $\%$ increment considering that the full body drag constraints the optimization process and C_L/C_D increases from 4.5 to 5.2. The sensitivity distribution of combined functions is given in figure 4.26 in which the reduction in intensity from baseline to optimum design can be clearly observed. The shape deformation together with the FFD box deformation is shown in comparison with the baseline design in figure 4.27. As seen, in the optimum design the intake surface and the rear lip are raised considerably and the ramp curvature increases which apparently improves the overall flow characteristic entering the duct.

The center-plane cross-sectional outlines and the 3D views are also given in figures 4.28 and 4.29. The drag is taken as penalty constraint which restricts deformation and hence optimization concludes even though the pressure is continues to rise as seen earlier in the optimizer iteration history. The pressure distribution before and after the shape deformation can be seen in figures 4.30 and 4.31. As it can be clearly observed that the quality of flow improves and the total pressure distribution at AIP shows an increase in the pressure value in the optimized case as compared to the baseline. The static pressure remains almost similar.

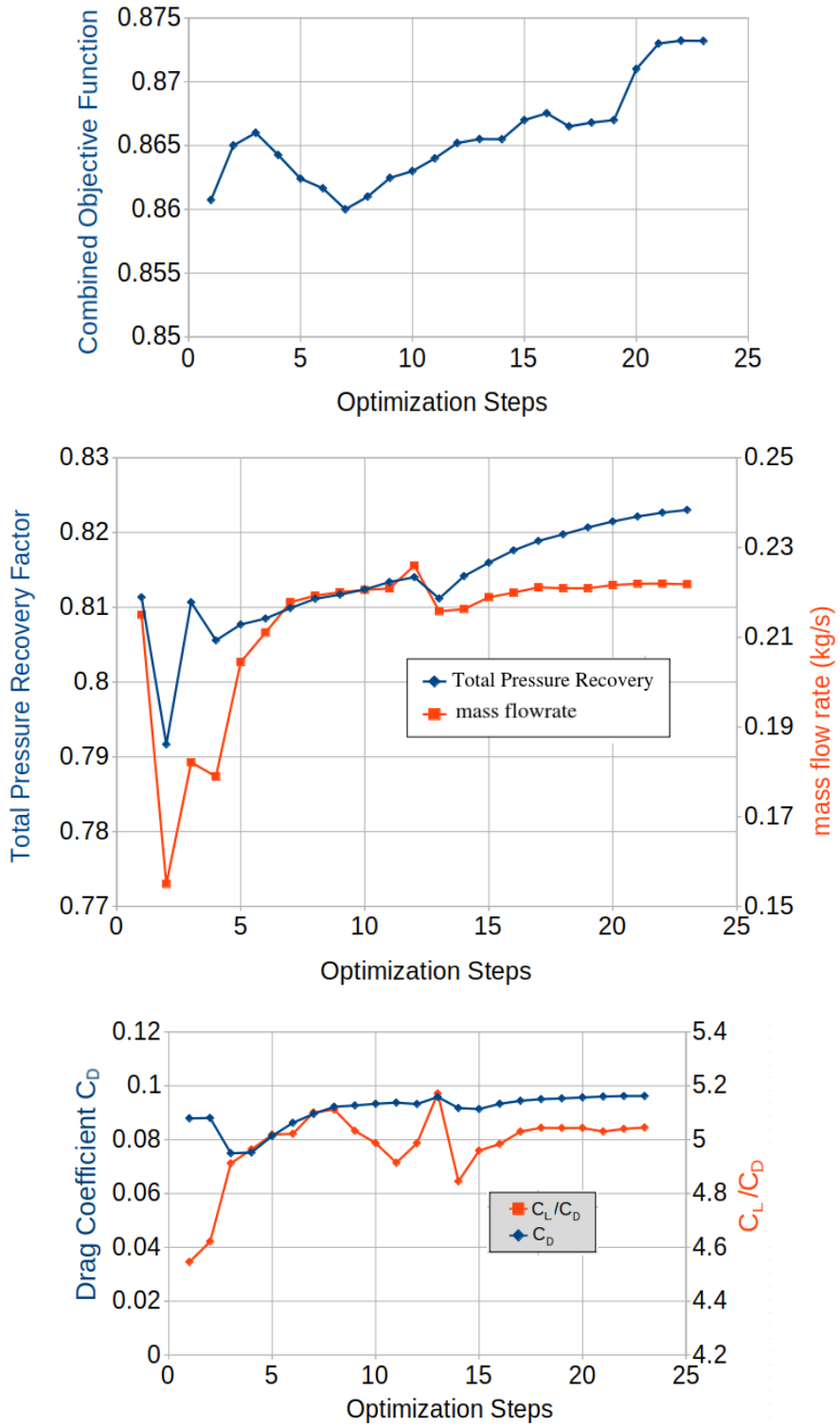

Figure 4.25: *Optimization history C_L/C_D and σ total pressure recovery factor.*

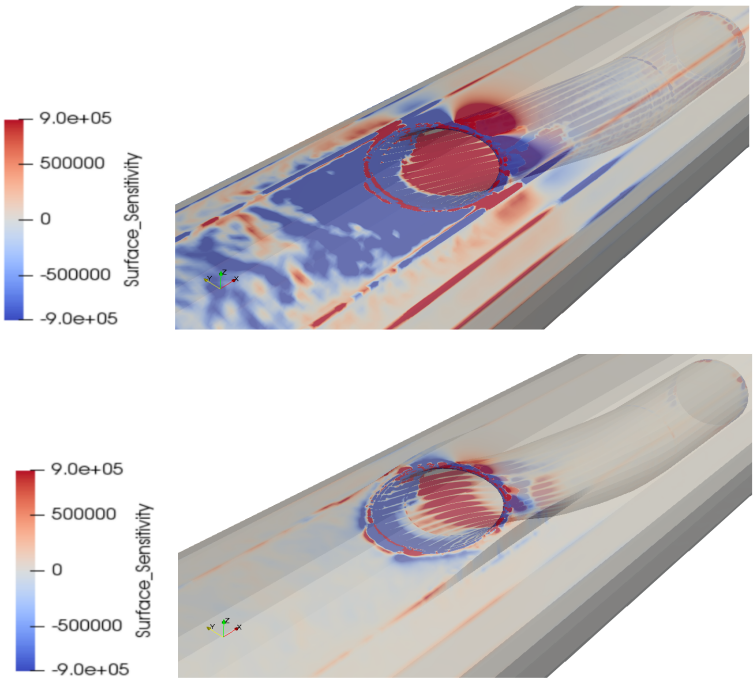

Figure 4.26: *Surface sensitivity: Top Baseline; Bottom Optimum design*

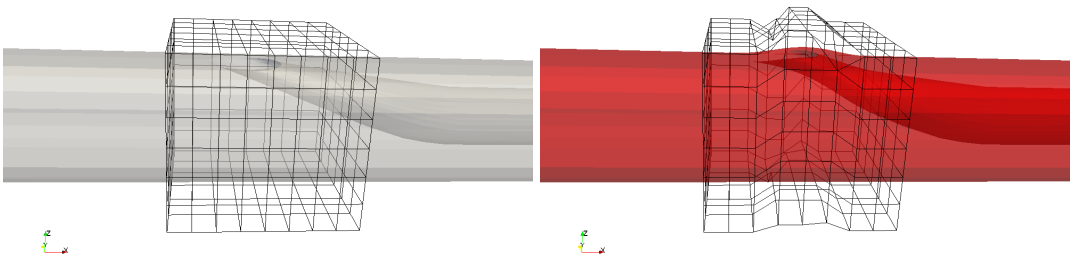

Figure 4.27: *FFD Box deformation; Left:Baseline; Right:Optimum Design.*

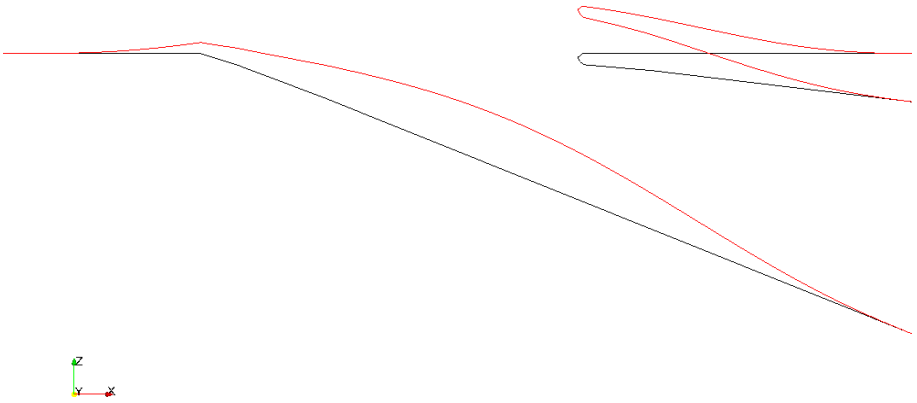

Figure 4.28: *Outlines of shape deformation process: Black: Baseline ; Red: Optimum design*

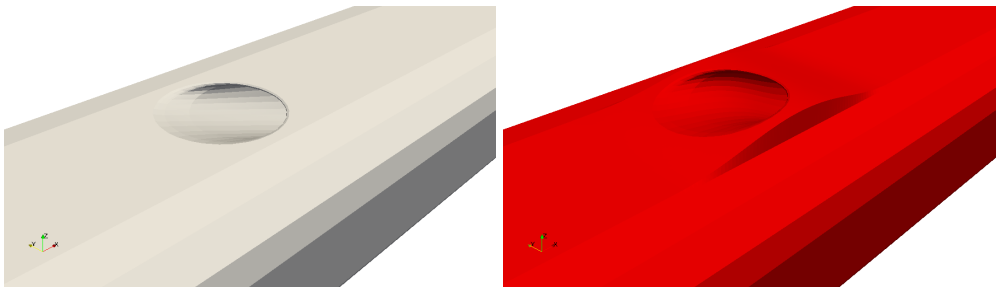

Figure 4.29: *3D view of shape deformation Left: Baseline ; Right: Optimum design*

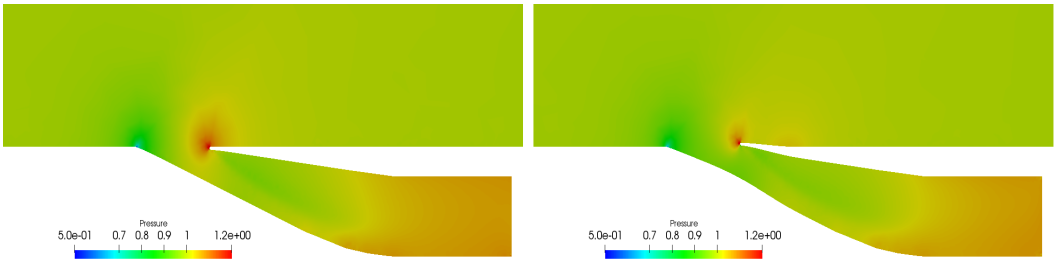

Figure 4.30: *Pressure Distribution for Left: Baseline ; Right: Optimum design*

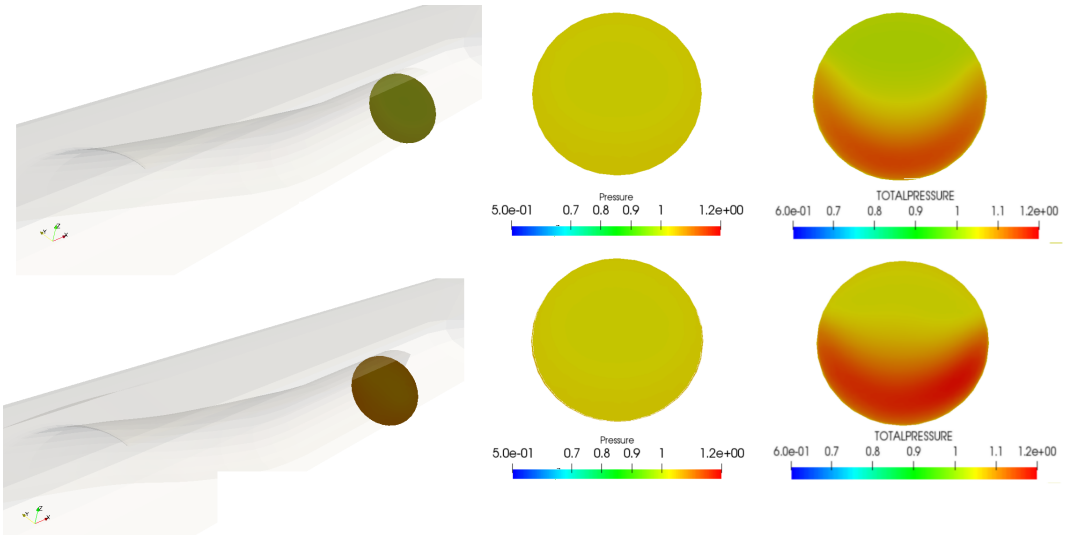

Figure 4.31: *Pressure at AIP for Top: Baseline ; Bottom: Optimum design*

Table 4.3: *Optimization Summary for case III.*

	Baseline	Optimum Design	Change
σ	0.81	0.825	+2 %
$C_L/\ C_D$	4.5	5	+0.5
C_D	0.088	0.097	10 %
DC(90)	10.5	10.64	0.14

4.4 Case IV: Trapezoidal-entrance Semi-submerged Intake

The shape optimization of the submerged intake is performed at α =0 ° where the total pressure recovery factor is 82% (figure 3.16). The optimization process commences in an iterative fashion. The shape deformation process is governed by the adjoint sensitivity gradients of the design variables. The optimization surfaces are shown in figure 4.32. The surfaces include the intake duct and the upper body surface flush with the intake. Hence in this case the deformation from a fully submerged to semi-submerged intake is allowed and the intake is not restricted to remain flush as in case II.

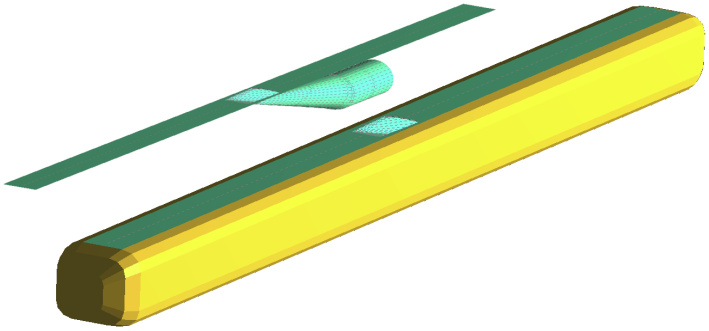

Figure 4.32: *Design variable surfaces in blue with and without full body in yellow.*

The FFD box placed over the design space, which defines the design variables, is shown in figure 4.33. The control points on the FFD box (8,8,11) provides a total of 484 design variables. Once the grid sensitivities for the combined multi-objective function are computed by the adjoint solver, they are projected onto the design variables through SU2 _DOT.

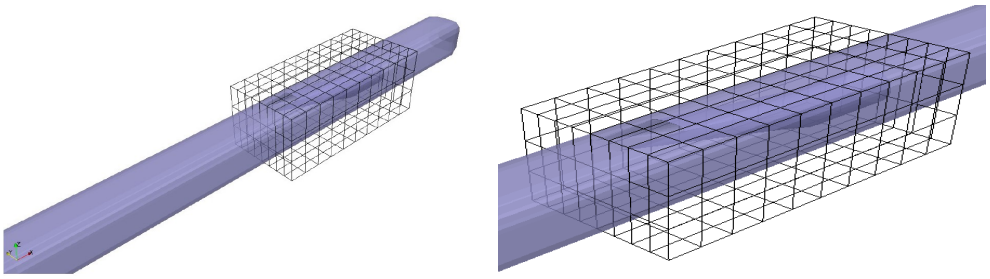

Figure 4.33: *FFD Box enclosing the design variable surfaces.*

The initial surface sensitivity distribution on the baseline design and the final distribution on the optimum design attained are compared in figure 4.34. The regions

of high sensitivity are shown in blue and red colors. It should be noted that at the end of the optimization process the surface sensitivities reduce to give almost negligible distribution at the optimum design.

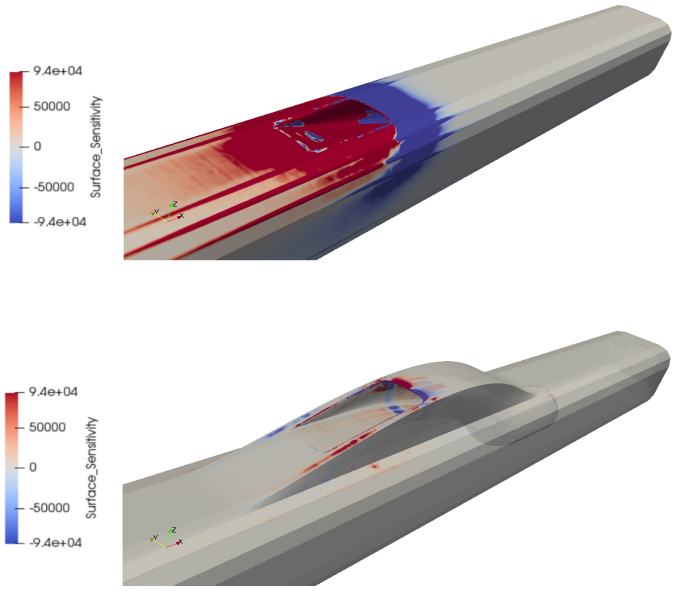

Figure 4.34: *Surface sensitivity: Top Baseline; Bottom Optimum design*

The optimization history for the combined and the individual objective functions are given in figure 4.35. The design optimization converges after 26 steps. The Total pressure recovery factor increases from 0.82 to 0.87 which is a 6 $\%$ increment. The optimization process stops when the combined function which attains a constant value. The C_L/C_D also increases from -0.007 to 0.04.

The shape deformation together with the FFD box deformation is shown in comparison with the baseline design in figure 4.36. As seen, in the optimum design the intake surface and the rear lip are raised considerably and the ramp curvature increases which apparently improves the overall flow characteristic entering the duct. The 3D views and the center-plane cross-sectional views are also given in Figures 4.37 and 4.38. Hence it is observed clearly that the baseline geometry is of a fully submerged intake in which the entrance is tangential to the freestream flow while after optimization the shape deforms into a semi-submerged intake. The upcoming air is now exposed to a intake entrance with a projection at an angle to it and hence higher pressure is achieved at the AIP due to ram effect which augments the pressure. The overall thickness of the mid-body increases accordingly as show in overlay of

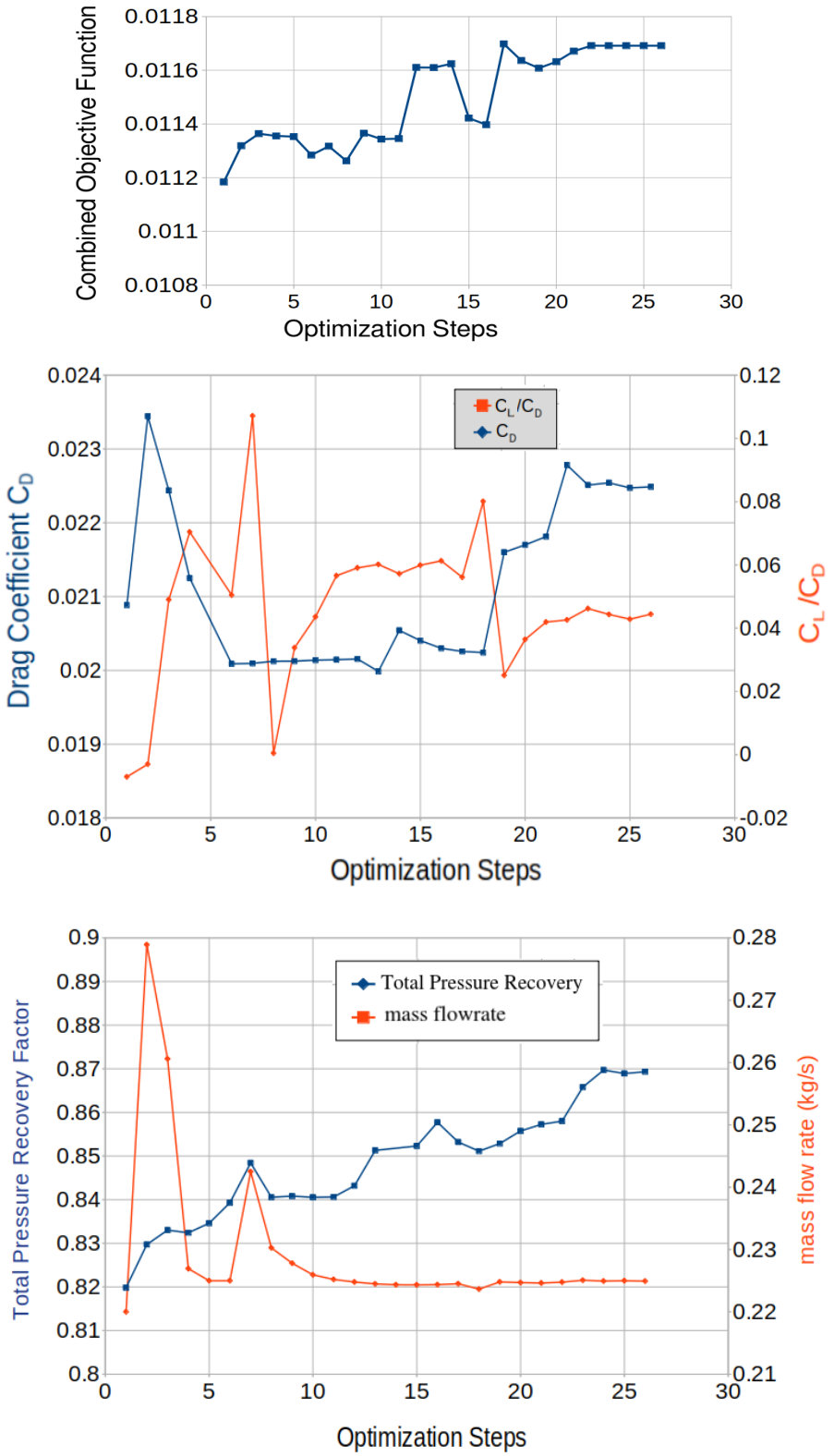

Figure 4.35: *Optimization history*

the surfaces in figure 4.39.

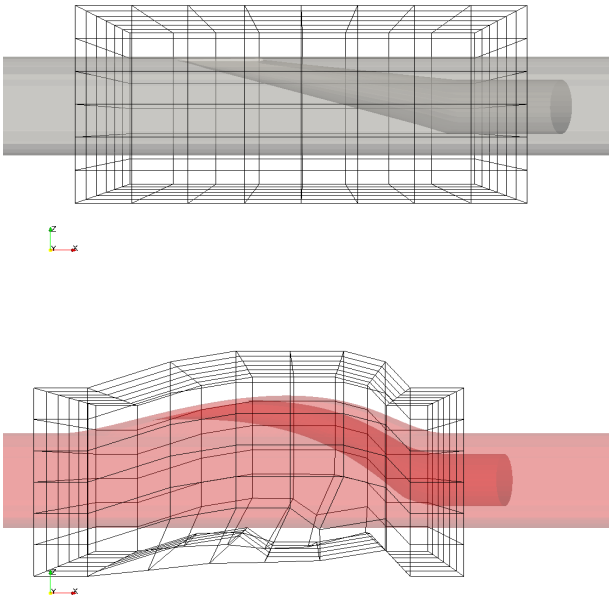

Figure 4.36: *FFD Box deformation; Top: Baseline; Bottom: Optimum design.*

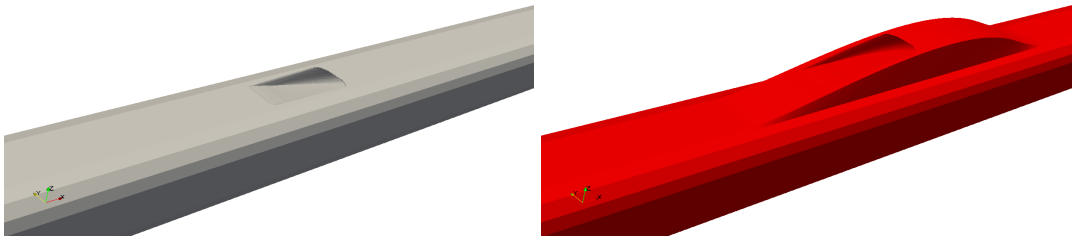

Figure 4.37: *3D view of shape deformation process; Left: Baseline, Right: Optimum design.*

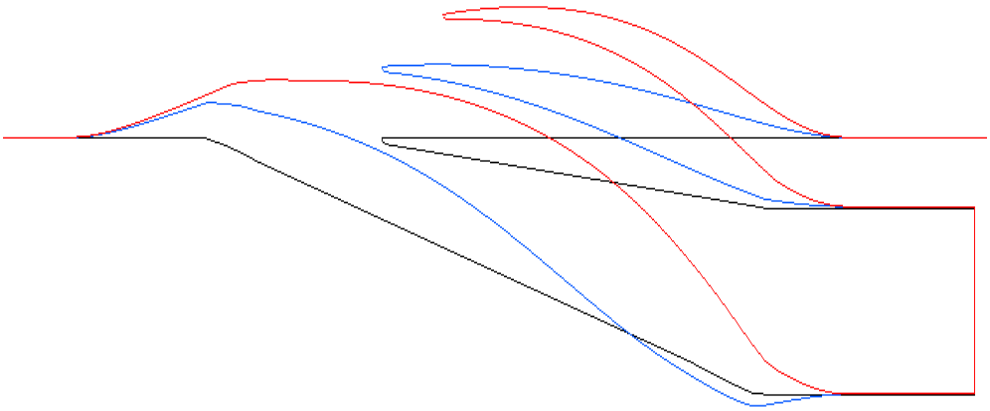

Figure 4.38: *Intake duct outlines at center plane ; Black: Baseline, Blue: Intermediate, Red: optimum design.*

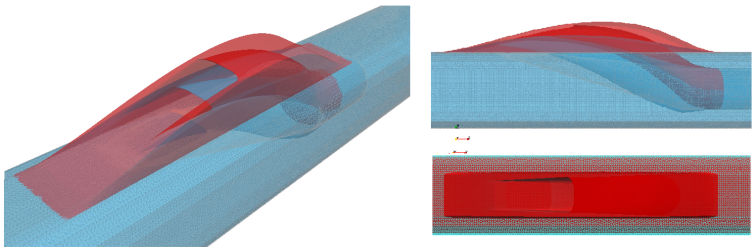

Figure 4.39: *3D overlay view of shape deformation process.*

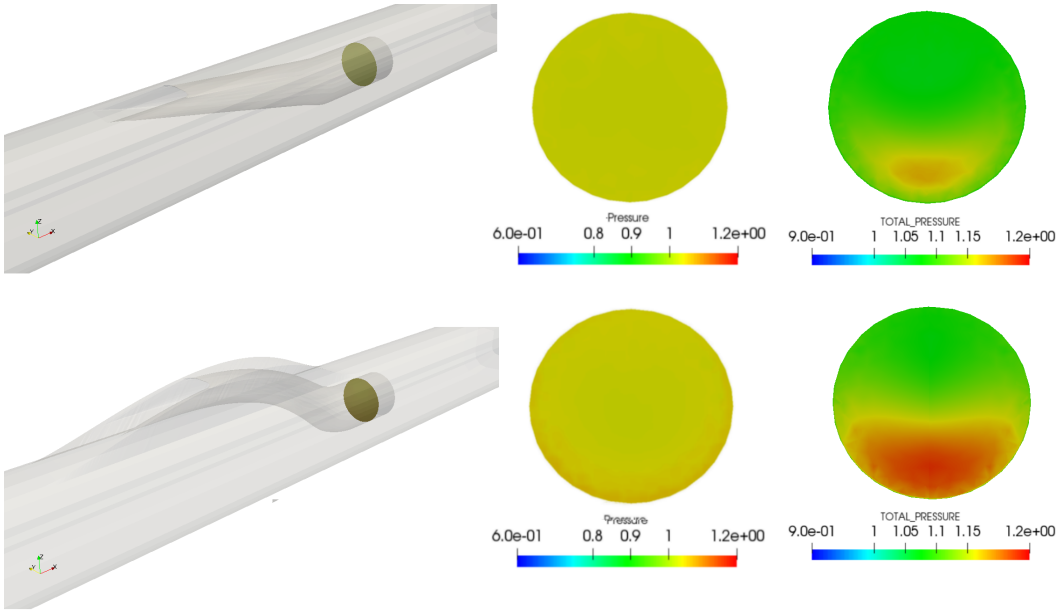

Figure 4.40: *Pressure at AIP; Top: Baseline; Bottom: Optimum design*

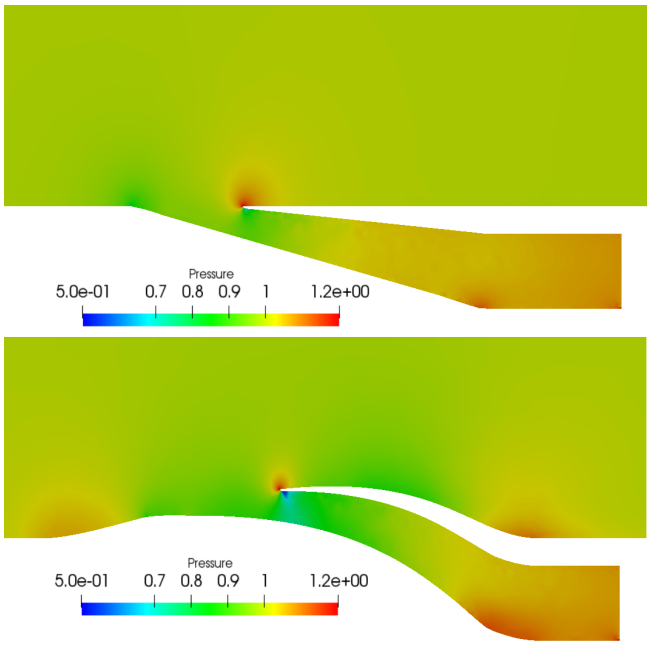

Figure 4.41: *Pressure distribution on center-plane ; Top:Baseline; Bottom: Optimum design.*

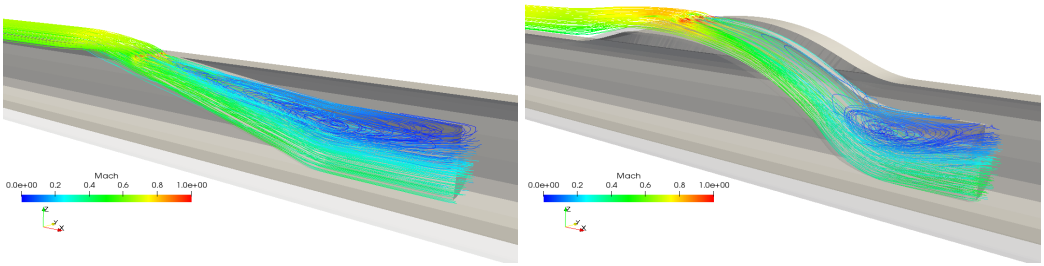

Figure 4.42: *Stream lines coloured with Mach number; Left: Baseline; Right: Optimum design.*

The intake duct deforms along with the centre body to form a bump which contributes to lift generation. The pressure distribution before and after the shape deformation can be seen in figure 4.40 and 4.41. As observed the quality of flow improves and the pressure distribution show a substantial increase in the pressure value at the AIP in the optimum case as compared to the baseline. The rise in the surface along with the intake duct now facing the flow instead of the tangential flow in the baseline gives greater flow with higher higher ram effect as shown by streamlines illustrating the captured flow in figure 4.42. The delay in flow separation and reduction in the re-circulation zone are noteworthy effects which are observed aft the rear lip region inside the duct. The separation point shifts from the lip to the duct bend where it connects to the fixed portion ahead of the AIP. It should also be noted that although the total pressure recovery factor is improved by the shape deformation which resulted in a semi-submerged intake, such a deformation increases the overall drag as mentioned earlier as well as it can increase the RCS signature of the slender body. The summary of the optimization is given in table 4.4.

Table 4.4: *Optimization summary for case IV.*

	Baseline	Optimum Design	Change
Pressure Recovery σ	0.82	0.87	+6 %
C_L/ C_D	-0.007	+0.04	+0.047
C_D	0.021	0.0225	7 %
DC(90)	18.1	15.9	-2.2

The results from shape optimization of case III and IV are show for comparison in figure 4.43 and 4.44. As clearly observed the shape of both cases deformed in an identical fashion given the same flow parameters, solver and optimization settings which validates the optimization process undertaken in the present study.

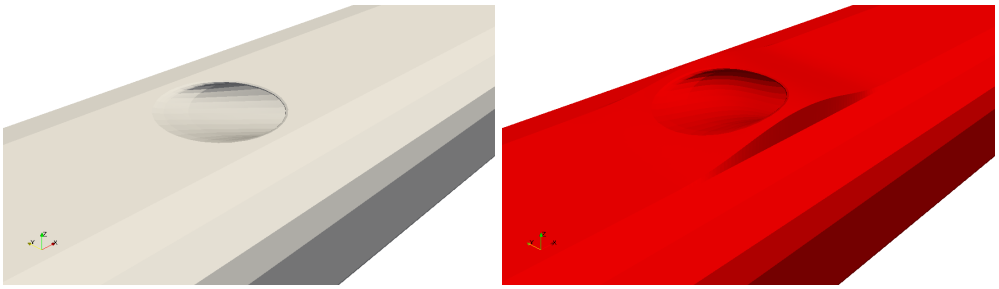

Figure 4.43: *Shape deformation for case III; Left : Baseline ; Right: Optimum design*

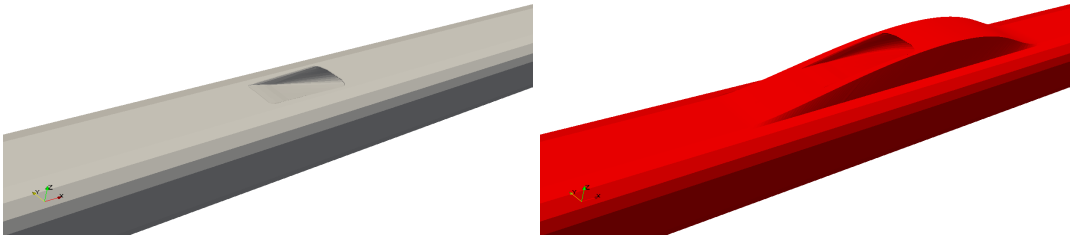

Figure 4.44: *Shape deformation for case IV intake; Left: Baseline; Right: Optimum design.*

4.5 Off-Design Analysis

The performance of the optimum configurations for the trapezoidal intake top mounted on a slender body (Case II and IV) is investigated at off-design conditions. It should be noted that the design optimizations are performed at $\alpha = 0^\circ$ and $M = 0.7$. The angle of attack and the Mach number are now varied by $\pm 2.5^\circ$ and ± 0.1, respectively.

Figure 4.45 shows the variation flow fields in terms of the mid-plane streamlines colored with Mach number. It is observed that the optimum flush and semisubmerged profiles perform better than the baseline by reducing the flow separation for both the lower and the higher Mach number cases. The better performances are quantified in the corresponding performance parameters, C_L/C_D and total pressure recovery at AIP given in Figure 4.46.

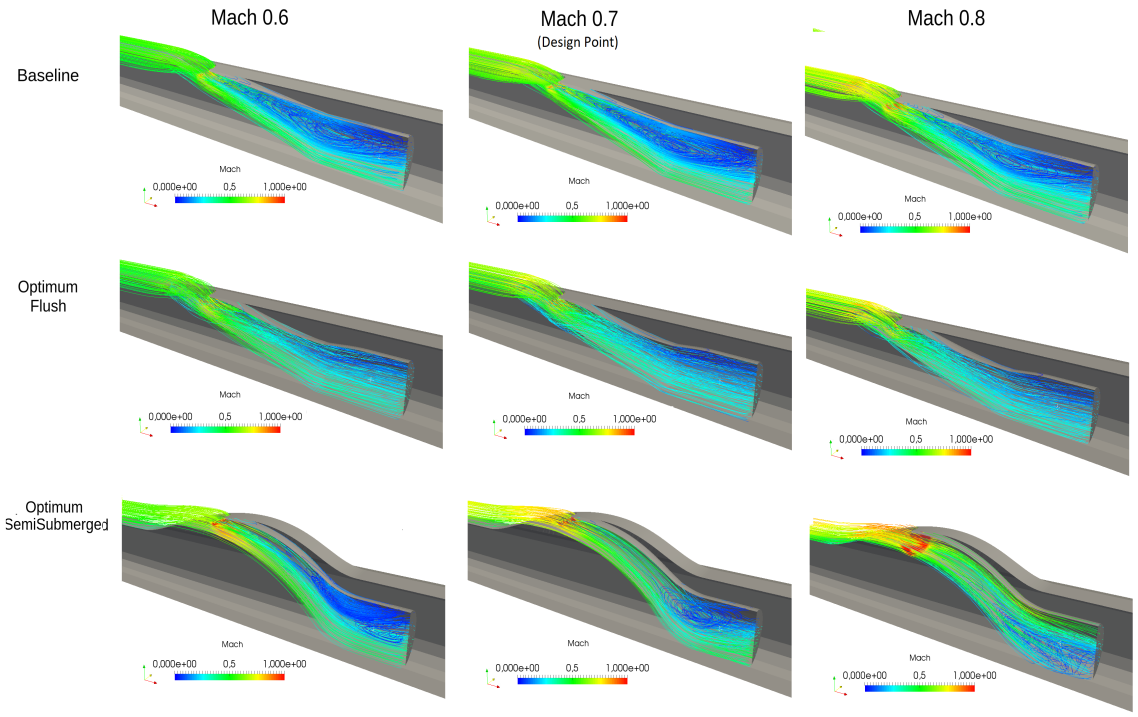

Figure 4.45: *Comparison of flow at design and off-design Mach numbers for fixed alpha=0°.*

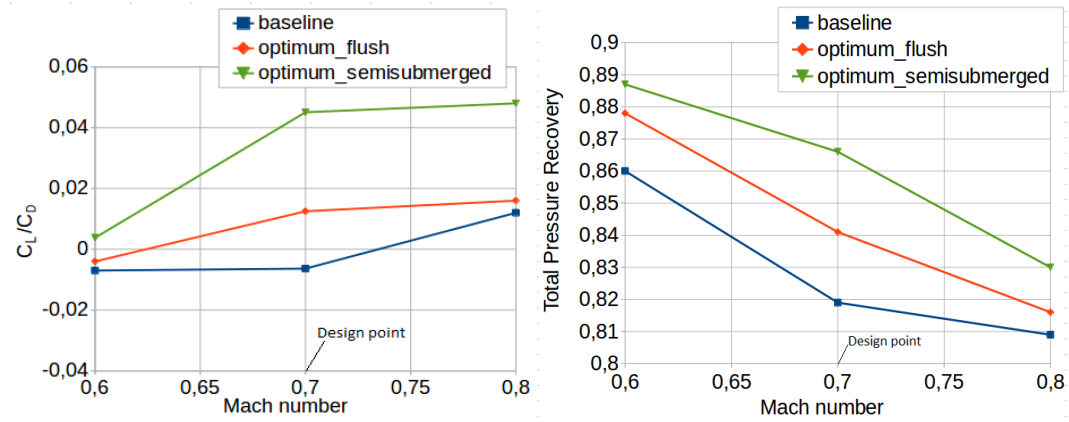

Figure 4.46: *Off-design performance at different Mach numbers for fixed alpha=0°.*

Figure 4.47 similarly shows the flow fields for the off-design angle of attack cases. The separated, recirculating flow regions are similarly reduced for the optimized configurations for both negative and positive angle of attack perturbations. The performance parameters support this observation as well (Figure 4.48). It is concluded that although a single point optimization is performed, the optimum configurations perform better than the baseline in the off-design conditions.

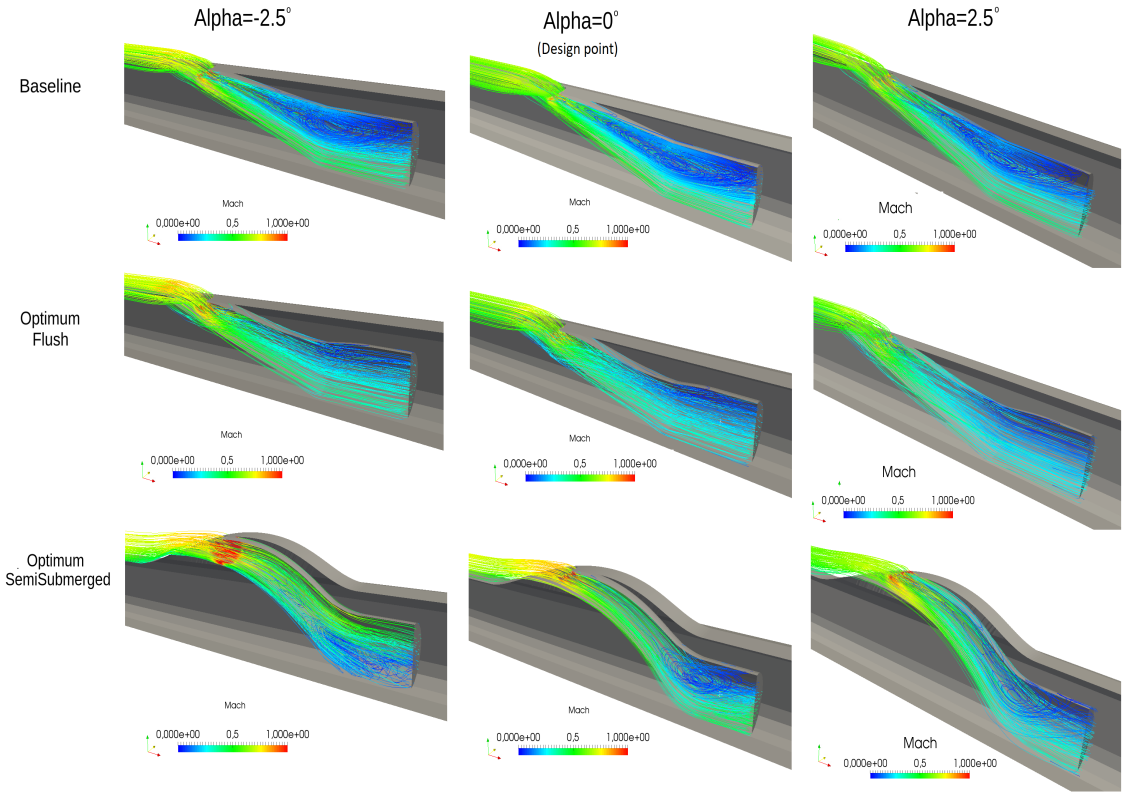

Figure 4.47: *Comparison of flow at design and off-design alpha for fixed Mach 0.7.*

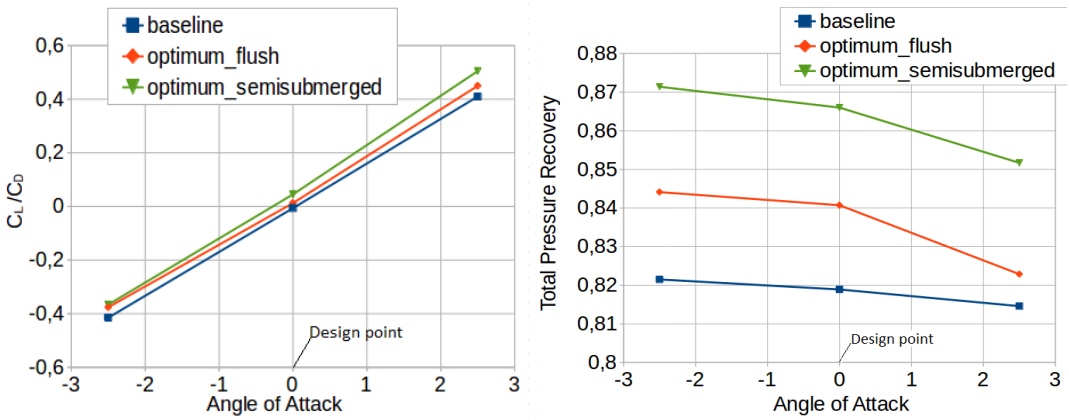

Figure 4.48: *Off-design performance at different alpha for fixed Mach 0.7.*

CHAPTER 5

CONCLUSION

In this study the adjoint based aerodynamic shape optimization study is performed for subsonic submerged intake. It is demonstrated that open-source SU2 software together with Salome, GMSH and ParaView can be effectively used to perform aerodynamic shape optimization of submerged intake configurations. The solutions are carried out in parallel computing environment. Flow solutions on adapted grids with SU2 over two intake configurations are validated against the limited experimental data. Free form deformation box technique is used as parameterization tool in-built continuous adjoint method is used to determine the sensitivity of objective function with respect to design variable.

Initially NACA intake placed on a flat plate is solved and result is compared with reference study at subsonic flow conditions. Thereafter single objective shape optimization is employed which enhances the lift from 0.08 to 0.53 at the end of design cycles. The other three cases of optimization are done using multi-objective function with total pressure and lift combined with drag as penalty constraint. The second case is of trapezoidal-entrance intake placed in slender aerodynamic body. The results are compared with reference study and baseline case for optimization is established. Multiple free form deformation boxes are employed. The intake remains flush with the body during the shape deformation process. The intake internal surface is then allowed to deform along the optimization steps. The pressure recovery increases by 3%. The third case is similar but with circular entrance on slender body. A single free form deformation box encloses the intake region and the deformation is allowed such that optimization creates a semi-submerged shape. The total pressure recovery factor increases by 2% and C_L/C_D also increases by 10%. In last case again

the trapezoidal entrance intake is employed. The optimization process is similar to the third case. The optimum shape produces a substantial deformation at the intake surface and a semi-submerged intake is finally formed. The total pressure recovery factor improves by 6% and an additional C_L/C_D ratio of 0.04 is achieved. The similar shape deformation and optimization results for third and last case validate the optimization procedure. Finally an off-design performance evaluation is done for the two optimum configurations of trapezoidal intake and it is concluded that although a single point optimization is performed, the optimum configurations perform better than the baseline in the off-design conditions.

This study gives a unique perspective into the flow characteristics of the different types of subsonic submerged intake design and its integration with the aerodynamic platform. The study also successfully demonstrates the efficacy of submerged intake as a lift generation device. Hence, with this newly gained knowledge and experience, further studies into the applications of such intakes can be undertaken. This study also expands the horizon into the field of aerodynamic shape optimization in general whereby an internal surface such as an intake duct can be specifically considered and deformed accordingly for given cost functions while being part of a larger external flow at subsonic free stream conditions.

REFERENCES

[1] C. W. Frick, F. D. Wallace, L. Randall, and A. E. Mossman, "An experimental investigation of a naca submerged- duct entrances," *NACA MR. No. A5E23 May 23*, 1945.

[2] A. H. Sacks and J. R. Spreiter, "Theoretical investigation of submerged inlets at low speeds," *TECHNICAL NOTE 2323 NACA*, 1951.

[3] E. A. Mossman and M. Randall, L., "An experimental investigation of the design variables for naca submerged duct entrances airplane," *NACA RM No. A7I30 January 8*, 1948.

[4] S. Sun, R. wei Guo, and Y. zhao Wu, "Characterization and performance enhancement of submerged inlet with flush-mounted planar side entrance," *JOURNAL OF PROPULSION AND POWER Vol. 23, No. 5, September October 2007*, 2007.

[5] N. J. Pignier, C. J. O'Reilly, and S. Boij, "Aerodynamic and aeroacoustic analyses of a submerged air inlet in a low-mach-number flow," *Computers and Fluids 133 15–31*, 2016.

[6] S. Menzel, M. Olhofer, and B. Sendhoff, "Application of free form deformation techniques in evolutionary design optimisation," *6 th World Congress on Structural and Multidisciplinary Optimization Rio de Janeiro, 30 May - 03 June 2005, Brazil*.

[7] J.Seddon and E. Goldsmith, "Intake aerodynamics," *AIAA Education Series*, 1985.

[8] J.Seddon and E. Goldsmith, "Practical intake aerodynamic design," *AIAA Education Series*, 1993.

[9] "https://en.wikipedia.org/wiki/gradient descent,"

[10] T. Shigefumi, K. Masato, and N. Yasushi, "Development of cfd shape optimization technology using the adjoint method and its application to engine intake port design," *SAE International Journal of Engines , Vol. 6, No. 2 (June 2013), pp. 833-842*.

[11] N. J. Martin and C. A. Holzhauser, "An experimental investigation at large scale of several configurations of an naca submerged air intake," *NACA RM No. A8F21 October*, 1948.

[12] R. A. Taylor, "Some effects of side-wall modifications on the drag and pressure recovery of an naca submerged inlet at transonic speeds," *NACA RM A51L03a*, 1952.

[13] L. S. Rolls, "A flight comparison of a submerged inlet and a scoop inlet at transonic speeds," *NACA RM No. A53AO6 March 19*, 1953.

[14] J. S. . Dennard, "A transonic investigation of the mass- flow and pressure recovery characteristics of several types of auxiliary air inlets," *NACA RM L57B07 April 10*, 1957.

[15] A. J. W. Smith and K. M. McCreath, "Boundary layer influence on the performance of submerged intakes," *The Aeronautical Journal Vol 71 Issue 680 August*, 1967.

[16] https://dokumen.tips/documents/esdu-inlets characteristics.html, "Drag and pressure recovery characteristics of auxiliary air inlets at subsonic speeds," *Standards and Technical Documents from IHS ESDU*, 1971.

[17] A. V. Roe and C. Ltd, "Tests on the naca-type flush air intake fitted to the sundstrand alternator and oil-cooler units," *Wind Tunnel Report ARD/WT/698/179*, 1958.

[18] L. Throndson, "Combat survivability with advanced aircraft propulsion development," *AIAA 81-1506R Journal of Aircraft VOL. 19, NO. 11, NOVEMBER*, 1982.

[19] J. W. Odendaal and D. Grygier, "Rcs measurements and results of an engine-inlet system design optimization," *IEEE Antennas and Propagation Magazine Vol 42 No 6 Dec*, 2000.

[20] AGARD270, "Air intakes for high speed vehicles," *AD-A248 September*, 1991.

[21] da Silveira, de Souza, and Almeida, "Numerical investigation of a naca air intake for a canard type aircraft," *IJAERS Vol-4, Issue-5, May*, 2017.

[22] Kornev and Boychuk, "Complex approach to aerodynamic design of inlet ducts with submerged vortex-free air intakes," *I.P. Aerospace and Mechanical Engineering. V.16, no.2*, 2017.

[23] S. SUN and R. GUO, "Numerical analysis and experimental validation of a submerged inlet on the plane surface," *Vol. 18 No. CHINESE JOURNAL OF AERONAUTICS August*, 2005.

[24] C. CHEN and ChungLung-Tan, "Numerical simulation of the submerged inlet," *AIAA 2137 26th Joint Propulsion Conference 1990*.

[25] T. BARDAGI and J.-L. LECORDIX, "Advanced sst auxiliary air intakes design and analysis," *AIAA 2304 29th Joint Propulsion Conference and Exhibit, Joint Propulsion Conferences*, 1993.

[26] E. Taskinoglu and D. Knight, "Numerical analysis of submerged inlets," *AIAA 3147 20th AIAA Applied Aerodynamics Conference, Fluid Dynamics and Co-located Conferences*, 2002.

[27] E. S. TASKINOGLU, "A multiobjective shape optimization study of a subsonic submerged inlet," *Phd Thesis Rutgers The State University of New Jersey May*, 2004.

[28] Wang, Wang, Xiao, Bing, Shuo, Guo, and Sun, "Construction methodology for lip surface of a submerged inlet," *Aerospace Science and Technology 54*, 2016.

[29] M. Ddo Carmo, "Differential geometry of curves and surfaces," *M Prentince-Hall*, 1976.

[30] O. AKMAN, "Subsonic- transonic submerged intake design for a cruise missile," *MS Thesis METU*, 2014.

[31] U. C. Küçük, "Passive flow control in boundary layer ingesting semi-submerged inlet," *MS Thesis METU*, 2015.

[32] C. C. Perez, S. B. Ferreira, and L. F. F. da Silva, "Computational study of submerged air inlet performance improvement using vortex generators," *JOURNAL OF AIRCRAFT Vol. 44, No. 5, September October*, 2007.

[33] G. Kaldschmidt and C. T. Syltebo, B. E.and Ting, "A 727 airplane center duct inlet low speed performance confirmation model test for re-fanned jt8d engines," *NASA CR-134534, Nov*, 1973.

[34] A. Jirasek, "Design of vortex generator flow control in inlets," *JOURNAL OF AIRCRAFT Vol. 43, No. 6, November December*, 2006.

[35] S. R. Wellborn, B. A. Reichert, and T. H. Okiishi, "An experimental investigation of the flow in a diffusing s-duct," *NASA Technical Memorandum 105809 AIAA-92-3622 July*, 1992.

[36] G. J. Harloff, C. F. Smith, J. E. Bruns, and J. R. DeBonis, "Navier-stokes analysis of three-dimensional s-ducts," *JOURNAL OF AIRCRAFT Vol. 30, No. 4, July-Aug*, 1993.

[37] D. shu Cheng, H. jun Tan, S. Sun, and Y. Tong, "Computational study of a high-performance submerged inlet with bleeding vortex," *JOURNAL OF AIRCRAFT Vol. 49, No. 3, May June*, 2012.

[38] M. Ruetten and H. Wendland, "Performance enhancement of auxiliary air intakes using vortex generators," *DOI:10.2514/6.2012-57 AIAA Conference Paper January*, 2012.

[39] M. Ruetten, L. Krenkel, and M. Freund, "Parametric design, comparison and evaluation of air intake types for bleedless aircraft," *39th Fluid Dynamics Conference DLR Institute of Aerodynamics and Flow Technology*, 2009.

[40] S. Sun, H.-J. Tan, and X. W. Chen, "Submerged inlet performance enhancement using a unique bump-shaped vortex generator," *JOURNAL OF PROPULSION AND POWER Vol. 32, No. 5, September-October*, 2016.

[41] D. Thévenin and G. Janiga, "Optimization and computational fluid dynamics," *ISBN 978-3-540-72152-9 Springer-Verlag Berlin Heidelberg*, 2008.

[42] A. S. Jamshid, "Survey of shape parameterization techniques for high-fidelity multidisciplinary shape optimization," *Aiaa Journal - AIAA J. 39. 877-884. 10.2514/2.1391*, 2001.

[43] A. S. Jamshid, "Geometry modeling and grid generation for design and optimization," *ICASE/LaRC/NSF/ARO WORKSHOP ON COMPUTATIONAL AEROSCIENCES IN THE 21st CENTURY Hampton, Virginia April 22-24*, 1998.

[44] A. Nitish, S. Vitale, P. Matteo, and P. Colonna, "Assessment of ffd and cad-based shape parametrization methods for adjoint-based turbomachinery shape optimization," *Proceedings of Montreal 2018 Global Power and Propulsion Forum 7 th - 9 th May, 2018 www.gpps.global GPPS-NA-2018-135*.

[45] M. J. Lighthill, "A new method of two-dimensional aerodynamic design.," *Reports and Memoranda No 2112, 1945.*

[46] R. M. Hicks and P. A. Henne, "Wing design by numerical optimization.," *Journal of Aircraft, Vol. 15, No. 7, pp. 407–412, 1977.*

[47] H. Sobieczky, "Parametric airfoils and wings," *Notes Numer. Fluid Mech., Vol. 68, pp. 71–88, 1999.*

[48] A. Shahrokhi and A. Jahangirian, "Airfoil shape parameterization for optimum navier-stokes design with genetic algorithm," *Aerosp. Sci. Technol., Vol. 11, pp. 443–450, 2007*.

[49] B. Epstein and S. Peigin, "Accurate cfd driven optimization of lifting surfaces for wing-body configuration," *Computers and Fluids, Vol. 36, pp. 1399–1414, 2007*.

[50] B. Epstein and S. Peigin, "A new efficient technology of aerodynamic design based on cfd driven optimization," *Aerospace Science Technology, Vol. 10, pp. 100–110, 2006*.

[51] A. Jameson, "Aerodynamic design via control theory," *Journal of Scientific Computing,3(3) - 233260, 1988*.

[52] G. S. Dulikravich, "Aerodynamic shape optimization methods," *in New Design Concepts for High Speed Air Transport by H. Sobieczky, Ed. Springer-Verlag, 1997, pp. 175–187.*

[53] "https://en.wikipedia.org/wiki/surrogate model,"

[54] R. P. Dwight, "Robust mesh deformation using the linear elasticity equations," *Proceedings of the Fourth International Conference on Computational Fluid Dynamics, Springer, Berlin, July 2006, pp. 401– 406.*

[55] W. K. Anderson and V. Venkatakrishnan, "Aerodynamic design optimization on unstructured grids with a continuous adjoint formulation," *Computers Fluids 28 (1999) 443-480.*

[56] E. Fabiano and D. J. Mavriplis, "Adjoint-based aerodynamic design on unstructured meshes," *AIAA 2016-1295 Session: Special Session: Aerodynamic Design Optimization Benchmark Problems IPublished Online:2 Jan 2016https://doi.org/10.2514/6.2016-1295.*

[57] (Wang, . E. F. He, and D. J. Mavriplis, "(wang and he) report from dagstuhl seminar 14371," *Adjoint Methods in Computational Science, Engineering, and Finance Edited by Nicolas R. Gauger , Michael Giles, Max Gunzburger , and Uwe Naumann.*

[58] L. Hascoet and Pascual, "The tapenade automatic differentiation tool: Principles, model, and specification," *ACM Trans. Math. Softw. 39, 3, Article 20 (April 2013), 43 pages. DOI: http://dx.doi.org/10.1145/2450153.2450158.*

[59] L. Hascoët, "Tapenade: a tool for automatic differentiation of programs," *Proceedings of 4th European Congress on Computational Methods, ECCOMAS' 2004, Jyvaskyla, Finland, 2004.*

[60] F. Palacio, T. D. Economon, A. C. Aranakez, S. R. Copelandz, A. K. Lonkarz, T. W. Lukaczykz, D. E. Manosalvasz, K. R. Naikz, A. S. Padronz, B. Traceyz, A. Variyarz, and J. J. Alonsox, "Stanford university unstructured (su2): Open-source analysis and design technology for turbulent flows," *AIAA SciTech 52nd Aerospace Sciences Meeting 13-17 January 2014.*

[61] B. M. Kulfan and Bussoletti, "Fundamental parametric geometry representations for aircraft component shapes," *11th AIAA/ISSMO Multidisciplinary Analysis and Optimization Conference: The Modeling and Simulation Frontier for Multidisciplinary Design Optimization, AIAA Paper 2006-6948, 2006.*

[62] G. Farin, "Curves and surfaces for computer aided geometric design," *Academic Press, New York, 1990.*

[63] U. Schramm, W. D. Pilkey, R. I. DeVries, , and M. P. Zebrowski, "Shape design for thin-walled beam cross sections using rational b-splines," *AIAA Journal, Voi. 33, No. 11, 1995.*

[64] T. Sederberg and S. Parry, "Free-form deformation of solid geometric models," *(1986) ACM Siggraph Computer Graphics. 20. 151-160.10.1145/15886.15903.*

[65] A. H. Barr, "Global and local deformations of solid primitives," *Computer Graphics 17,3 (July 1984), pp 21-30.*

[66] D. Chauhan, P. Chandrashekar, and R. Duvigneau, "Wing shape optimization using ffd and twist parameterization," *12th Aerospace Society of India CFD Symposium.*

[67] R. Duvigneau, "Adaptive parameterization using free-form deformation for aerodynamic shape optimization," *HAL [Research Report] 2006, pp.40. ffinria-00085058v1f.*

[68] H. L. Kline, "The continuous adjoint method for multi-fidelity hypersonic inlet design," *PhD Thesis Stanford University April 2017*.

[69] J. J. Alonso, F. Palacios, T. Economon, M. Colonno, S. Copel, and t. the SU2, "High-fidelity aerodynamic shape optimization using su2," *MDO Consortium Workshop Stanford University*, 2013.

[70] J. H. C. T. J.Lin, Z. Q. Guan and S. H. Lo, "Vertex-ball spring smoothing: An efficient method for unstructured dynamic hybrid meshes," *Computer Structures, Vol. 136,pp. 24–33, May 2014* .

[71] J. T. Batina, “Using unstructured dynamic meshes,” *AIAA Journal, Vol. 28, No. 8, pp.1381–1388, Aug. 1990* .

[72] O. Estruch, O. Lehmkuhl, R. Borrell, C. D. P. Segarra, and a. Oliva, “A parallel radial basis function interpolation method for unstructured dynamic meshes,” *Computers and Fluids, Vol. 80, No. 1, pp. 44–54, 2013.*

[73] Y. YANG, “Application of spring analogy mesh deformation technique in airfoil design optimization,” *Masters Thesis METU JULY 2015.*

[74] J. F. Blom, “Considerations on the spring analogy,” *March 2000 International Journal for Numerical Methods in Fluids 32(6):647 - 668 DOI: 10.1002/(SICI)1097-0363(20000330)32:6<647::AID-FLD979>3.0.CO;2-K* .

[75] D. D. Knight, “Automated optimal design of supersonic and subsonic diffusers using cfd,” *Proceedings European Congress on Computational Methods in Applied Sciences and Engineering, The European Community on Computational Methods in Applied Sciences Center, CIMNE, Barcelona,Spain, Sept. 2000.*

[76] D. D. Knight, “Automated optimal design using cfd and high performance computing,” *Lecture Notes in Computer Science, Springer-Verlag, Berlin, Vol. 1215, 1997, pp. 198–221.*

[77] D. D. Knight, “Application of genetic algorithms to high speed air intake design,” *Von Karman Institute for Fluid Dynamics Lecture Series Program, Rept. VKI LS 2000-07, Vol. 1, Rhode Saint Genese, Belgium, May 2000.*

[78] G. C. Zha, D. Smith, M. Schwabacher, K. Rasheed, A. Gelsey, D. Knight, and M. Haas, “High performance supersonic missile inlet design using automated optimization,” *Journal of Aircraft, Vol. 34, No. 6, 1997, pp. 697–705.*

[79] E. Reddy and D. R. Reddy, “Aerodynamic shape optimization of a subsonic inlet using 3-d euler computation,” *in 31 st AIAA/;ASME/SAE/ASEE Joint Propulsion Conference and Exhibit, AIAA 95-2757, San Diego, July 10-12, 1995.*

[80] S. Lefantzi and D. D. Knight, "Automated design optimization of a three-dimensional s-shaped subsonic diffuser," *JOURNAL OF PROPULSION AND POWER Vol. 18, No. 4, July – August 2002.*

[81] M. Blaize, D. D. Knight, and K. Rasheed, "Automated optimal design of two-dimensional supersonic missile inlets," *Journal of Propulsion and Power, Vol. 14, No. 6, 1998, pp. 890–898.*

[82] M. Blaize, D. D. Knight, K. Rasheed, and Y. Kergeravat, "Optimal missile inlet design by means of automated numerical optimization," *Proceedings of the RTO Meeting 5, RTO-MP-5, Paper 37, BP 25, Neuilly-Sur-Seine Cedex, France, pp. 37-1–37-9.*

[83] C. Bourdeau, G. Carrier, and D. Knight, "Three dimensional optimization of supersonic inlets," *AIAA Paper 99-2108, June 1999.*

[84] G. Carrier, C. Bourdeau, D. Knight, Y. Kergaravat, and X. Montazel, "Multi-flight condition optimization of three-dimensional supersonic inlets," *Proceedings of the RTO Meeting 35, RTO-MP-035, Paper 30, BP25, Neuilly-Sur-Seine Cedex, France, pp. 30-1–30-10.*

[85] S. R. Wellborn, B. A. Reichert, and T. H. Okiishi, "An experimental investigation of the flow in a diffusing s-duct," *Journal of Propulsion and Power, Vol. 10, No. 5, 1994, pp. 668–675.*

[86] W. Gan and X. Zhang, "Design optimization of a three-dimensional diffusing s-duct using a modified sst turbulent model," *Aerospace Science and Technology Volume 63, April 2017, Pages 63-72.*

[87] W. Zhang, D. Knight, and D. Smith, "Automated design of a three dimensional subsonic diffuser," *Journal of Propulsion and Power, Vol. 16, No. 6, 2000, pp. 1132–1140.*

[88] J. Zhang, C. Wang, and K. Lum, "Multidisciplinary design of s-shaped intake," *26th AIAA Applied Aerodynamics Conference, AIAA 2008-7060, Honolulu, Hawaii, 2008.*

[89] B. L. Berrier, M. B. Carter, and B. G. Allan, "High reynolds number investigation of a flush-mounted, s-duct inlet with large amounts of

boundary layer ingestion," *in National Aeronautics and Space Administration, NASA/TP-2005-213766, Virginia, September,2005.*

[90] K. M. Loeper and P. King, "Numerical investigation of geometric effects on performance of s-ducts," *in 47th AIAA Aerospace Sciences Meeting Including The New Horizons Forum and Aerospace Exposition, AIAA 2009-713, Orlando, Florida, 5 - 8 January 2009.*

[91] W. Gan and X. Zhang, "Design optimization of a three-dimensional diffusing s-duct using a modified sst turbulent model," *Aerospace Science and Technology Volume 63, April 2017, Pages 63-72.*

[92] H. He and X. Li, "Design of s-shaped submerged inlet," *in Advanced Materials Research Vols., 2011.*

[93] D. F. Andre Lombardi and L. Santos, "Aircraft air inlet design optimization via surrogate-assisted evolutionary computation," *Springer International Publishing Switzerland 2015 A. Gaspar-Cunha et al. (Eds.): EMO 2015, Part II, LNCS 9019, pp. 313–327, 2015. DOI: 10.1007/978-3-319-15892-1 21.*

[94] Y. JunSok, C. Kim, and L. Byung Joon, "Adjoint-based design optimization of vortex generator in an s-shaped subsonic inlet," *AIAA JOURNAL Vol. 50, No. 11, November 2012 .*

[95] T. Albring, M. Sagebaum, and N. R. Gauge, "Efficient aerodynamic design using the discrete adjoint method in su2," *17th AIAA/ISSMO Multidisciplinary Analysis and Optimization Conference, 13 – 17 June 2015, Washington, D.C.*

[96] G. Oates, "Aircraft propulsion technology and design," *AIAA Education Series*, 1989.

[97] J. D. Mattingly and H. von Ohain, "Elements of propulsion:gas turbines and rockets," *AIAA Education Series*, 2006.

[98] A. Busemann, "Dieachsensymmetrische kegeligeüberschallströmung," *Luftfahrtforschung. ;19(4):137-144*, 1944.

[99] Gubanov, "Advances in aerodynamics," *https://doi.org/10.1186/s42774-019-0013-8*, 2019.

[100] V. Blishch, "External and internal aerodynamic forces and moments of air-breathing jet powered vehicles and their models at incidence and sideslip," *Trudy TsAGI, Issue 2328*, 1987.

[101] J. Steelant and T. Langener, "The lapcat-mr2 hypersonic cruiser concept," *29th Congress of the International Council ofthe Aeronautical Sciences,St.-Petersburg, Russia, 7–12 Sept*, 2014.

[102] E. C. Polhamus, "A concept of the vortex lift of sharp-edge delta wings based on a leading-edge-suction analogy," *Langley Research Center NASA TN D-3767*, 1966.

[103] H. HOEIJMAKERS and RIZZI, "A. vortex-fitted potential and vortex-captured euler solution for leading-edge vortex flow," *AIAA Journal,23, (12), pp 1983–1985*.

[104] J. LAMAR, "Extension of leading-edge suction analogy to wings with separated flow around the side edges at subsonic speeds," *NASA TR R-428*, 1974.

[105] G. N. Stephen and S. Ariela, "Linear and nonlinear programming," *Publishers: McGraw-Hill Science, Engineering Mathematics, 1996.*

[106] "https://docs.scipy.org/doc/scipy/reference/optimize.html,"

[107] H. Schlichting and K. Gersten, "Boundary-layer theory," *Springer 8th Ed. 2000.*

[108] E. Fabiano and D. J. Mavriplis, "Adjoint-based aerodynamic design on unstructured meshes," *DOI: 10.2514/6.2016-1295 Conference: AIAA Scitech 2016*.

[109] A. Jameson, "Aerodynamic shape optimization using the adjoint method," *Lectures at the Von Karman Institute, Brussels 2003*.

[110] J. Nocedal and S. J. Wright, "Numerical optimization," *Springer. ISBN 0-387-30303-0.*, 2006.

[111] "https://stats.stackexchange.com/questions/268290/in-mathematical-optimization-are-sequent quadratic-programming-and-sequentia,"

[112] "Su2 tutorials and help,"
https://su2code.github.io/tutorials/home/
https://www.youtube.com/channel/UCQq2$_D k2MvGGqi8 - eBVwRww$.

[113] A. Aniket, C. Alejandro, C. Sean, P. Francisco, C. Michael, T. Economon, J. Alonso, L. Amrita, L. Trent, and T. Thomas, "Stanford university unstructured (su2): An open-source integrated computational environment for multi-physics simulation and design," *51st AIAA Aerospace Sciences Meeting including the New Horizons Forum and Aerospace Exposition 2013*.

[114] Y. Kim Kwang, A. Samad, and E. Benini, "Design optimization of fluid machinery: Applying computational fluid dynamics and numerical optimization," *Wiley*, 2019.

[115] L. Pustina, R. Cavallaro, G. Bernardini, and R. Bombardieri, "Towards fully automated aerodynamic shape optimization of nonplanar wings with su2," *4th Annual SU2 Developers Meeting - May 8-10, 2019*.

[116] T. D. Economon, F. Palacios, R. Copeland, T. W. Lukaczyk, and J. J. Alonso, "Su2: An open-source suite for multiphysics simulation and design," *AIAA JOURNAL Vol. 54, No. 3, March 2016*.

[117] C. Geuzaine and J.-F. Remacle, "Gmsh: a three-dimensional finite element mesh generator with built-in pre- and post-processing facilities.," *International Journal for Numerical Methods in Engineering 79(11), pp. 1309-1331*, 2009.

[118] H. Schlichting and K. Gersten, *Boundary-Layer Theory*. Springer, 8th ed., 2000.

APPENDIX A

A.1 Initial Cell Height Calculation for Prism Layer Mesh

The following relations lead to the calculations of the physical cell wall height Y based on fluid properties and flow parameters. This wall distance is incorporated into the volume mesh generation process. In order to take into account the viscous sub-layer the cell height neighbouring the wall should have a Y+ = 1 for the given free stream velocity and fluid viscosity.

$$Y+ = \frac{Y u_\tau}{\nu_w} \tag{A.1}$$

and u_τ is the shear velocity calculated as:

$$u_\tau = \sqrt{\frac{\tau_w}{\rho}} \tag{A.2}$$

where τ_w is the shear stress calculated at the wall given by ,

$$\tau_w = 0.5 c_f \rho {U_\infty}^2 \tag{A.3}$$

for the given fluid density ρ and flow velocity U_∞. The local skin friction coefficient c_f formula for turbulent boundary layer given by Schlichting [118] :

$$c_f = \frac{0.058}{Re^{0.2}} \tag{A.4}$$

For the sake of demonstration the height of wall neighbouring cell is calculated for the case of flat plate surface of 5 m length, pressure at 1atmosphere and room temperature of 288 K.

Table A.1: *Cell height calculation from flow and Y+* .

Parameters	Values
Freestream Mach M	0.6
Freestream Temperature T	288 K
Reference Length L	5 m
Viscosity ν	1.48e-05 m^2/sec
Freestream Velocity U=M* $\sqrt{\gamma}$ R T	198 m/s
Density ρ	1.225 Kg/m^3
Re	66.9e+06
C_f	0.00157
Wall Shear Stress τ_w	37.9 Pa
u	5.47 m/s
Cell Height Y	2.7 e-06 m

The calculated cell height is implemented in mesh generation using GMSH.

A.2 Solver Settings in SU2 CFD cfg file

——— FLOW NUMERICAL METHOD DEFINITION ———

- Convective numerical method
  CONV NUM METHOD FLOW= AUSM
  SLOPE LIMITER FLOW= VENKATAKRISHNAN
- Spatial numerical order integration
  MUSCL FLOW= YES
- Coefficient for the limiter (smooth regions)
  VENKAT LIMITER COEFF= 1.0
- 2nd and 4th order artificial dissipation coefficients
  JST SENSOR COEFF= (0.5, 0.02)
- Time discretization
  TIME DISCRE FLOW= EULER IMPLICIT

———-SLOPE LIMITER DEFINITION ———————

- Coefficient for the sharp edges limiter
  ADJ SHARP LIMITER COEFF= 1.0
- Reference coefficient (sensitivity) for detecting sharp edges.
  REF SHARP EDGES= 3.0
  SENS REMOVE SHARP= NO

————- TURBULENT NUMERICAL METHOD DEFINITION————————

- Convective numerical method (SCALAR UPWIND)
  CONV NUM METHOD TURB= SCALAR UPWIND
- Monotonic Upwind Scheme for Conservation Laws (TVD) in the turbulence equations.Required for 2nd order upwind schemes (NO, YES)
  MUSCL TURB= YES

- Slope limiter (VENKATAKRISHNAN, MINMOD)
  SLOPE LIMITER TURB= VENKATAKRISHNAN
- Time discretization (EULER IMPLICIT)
  TIME DISCRE TURB= EULER IMPLICIT

——— ADJOINT-FLOW NUMERICAL METHOD DEFINITION ———

- Convective numerical method
  CONV NUM METHOD ADJFLOW= JST
- Slope limiter: (VENKATAKRISHNAN, SHARP EDGES)
  SLOPE LIMITER ADJFLOW= VENKATAKRISHNAN
- 2nd, and 4th order artificial dissipation coefficients
  ADJ JST SENSOR COEFF= (0.0, 0.02)
- Reduction factor of the CFL coefficient in the adjoint problem
  CFL REDUCTION ADJFLOW= 0.5
- Time discretization (RUNGE-KUTTA EXPLICIT, EULER IMPLICIT)
  TIME DISCRE ADJFLOW= EULER IMPLICIT

——- FREE-FORM DEFORMATION PARAMETERS ————

- Tolerance of the Free-Form Deformation point inversion
  FFD TOLERANCE= 1E-10
- Maximum number of iterations in the Free-Form Deformation point inversion
  FFD ITERATIONS= 500
- FFD farfield definition: 3D case (FFD farfieldTag, X1, Y1, Z1, X2, Y2, Z2, X3, Y3, Z3, X4, Y4, Z4, X5, Y5, Z5, X6, Y6, Z6, X7, Y7, Z7, X8, Y8, Z8)

  FFD DEFINITION= (WING,-6, -3, -0.5, 6,-3, -0.5, 6,3,-0.5, -6,3,-0.5, -6,-3, 0.5, 6,-3, 0.5, 6,3, 0.5, -6,3, 0.5)
- FFD DEGREE= (10, 8, 3)
- Surface continuity at the intersection with the FFD
  FFD CONTINUITY= 2ND DERIVATIVE

- Optimization objective function with scaling factor
- OPT OBJECTIVE= TOTAL OUTLET PRESSURE*-1E-6;LIFT * 0.01; (DRAG<0.023)*1.0
- OPT ITERATIONS= 100
- OPT ACCURACY= 1E-10
- OPT BOUND UPPER= 0.03
- OPT BOUND LOWER= -0.03

———— DESIGN VARIABLE PARAMETERS ————

- Kind of deformation (FFD SETTING, FFD CONTROL POINT 2D)
  DV KIND= FFD CONTROL POINT
- Marker of the surface in which we are going apply the shape deformation DV MARKER= (body)
- Parameters of the shape deformation
  FFD CONTROL POINT (FFD farfieldTag, i Ind, j Ind, k Ind, x Disp, y Disp, z Disp)
  DV PARAM= (WING, 1, 1, 1, 0.4, 0.4, 0.4)
- New value of the shape deformation
  DV VALUE= 0.0